UNIVERSITÀ
DEGLI STUDI
DI PADOVA

TÉCNICO
LISBOA

UNIVERSITÀ DEGLI STUDI DI PADOVA
CENTRO INTERDIPARTIMENTALE *"Centro Ricerche Fusione"*

UNIVERSIDADE TÉCNICA DE LISBOA
INSTITUTO SUPERIOR TÉCNICO

JOINT RESEARCH DOCTORATE IN FUSION SCIENCE AND ENGINEERING
CYCLE XXVI

Development of 2D/3D equilibrium codes for magnetically confined fusion experiments

Coordinator: Ch.mo Prof. Piero Martin

Supervisor: Ch.mo Prof. Leonardo Giudicotti

Supervisor: Dott. Paolo Zanca

Supervisor: Dott. David Terranova

Doctoral student: Gregorio Luigi Trevisan

Contents

Abstract

The present work is the result of a three-year Ph.D. research project carried out at Consorzio RFX on magnetically confined plasmas.

Research on controlled thermonuclear fusion is currently being pursued by many countries throughout the world, thanks to its promise of a relatively clean and abundant energy source. The next steps for the international community are the construction and operation of a large device, ITER, considered as the last fusion physics experiment with respect to the tokamak configuration. After ITER, in fact, the first commercial proto-reactor, DEMO, is envisaged to demonstrate the feasibility of fusion as an energy source. The stellarator community, on the other hand, is building a new device, Wendelstein 7-X, which will provide further insight into three-dimensional physics.

Among the various fusion devices, the reversed-field pinch has been demonstrated, if not a viable device for commercial energy production, an excellent tool for plasma physics studies. The RFX-mod experiment situated at Consorzio RFX in Padova, Italy, is the biggest RFP device in the world and the most advanced fusion device with respect to active stabilization of magnetohydrodynamic perturbations through feedback control. The RFX-mod team, furthermore, has tackled first theoretically and then experimentally the paramount concept of self-organization in RFPs, which produces enhanced confinement regimes with better transport properties and reduced magnetic chaos. Resonant tearing modes are known to be the biggest players in the dynamo mechanisms responsible for the helically deformed and enhanced regimes.

In such a complex framework, the reconstruction of the tearing modes inside the plasma through external measurements is extremely important for both modelling and experimental reasons since, for example, the structures influencing the core transport properties of plasmas are in part linked to tearing modes.

The present Ph.D. thesis focuses, in particular, on the development of two- and three-dimensional equilibrium codes.

As a first problem, a Fortran algorithm has been developed for the numerical solution of the helical Grad-Shafranov equation, which is a two-dimensional equilibrium equation derived under the assumption of helical symmetry. Such assumption is found to be particularly appropriate for the study of the dominant tearing mode in RFX-mod during routine quasi-single-helicity phases in RFP shots, but it can be applied to tokamak shots as well.

As a second problem, the three-dimensional VMEC/V3FIT code suite for equilibrium reconstruction has been analysed and studied. The helical Grad-Shafranov solver has been tested against the three-dimensional VMEC/V3FIT

predictions, carrying out a valuable benchmark. Then, a further step has been taken in the application of the V3FIT code to fixed-boundary reconstructions in RFX-mod by implementing a new virtual diagnostic, which had been previously demonstrated to be able to solve the mismatch in the edge value for the helical safety factor.

The thesis is organized as follows.

Part I, “Introduction”.

In **chapter 1**, controlled thermonuclear fusion is introduced as a feasible energy source and basic notions of fusion physics are discussed. In **chapter 2**, the most important aspects of fusion physics are discussed for both reversed-field pinches and tokamaks, and the concepts of self-organization and dynamos are introduced as a reason to study both three-dimensional physics and tearing mode reconstruction. In **chapter 3**, the general equations of magnetohydrodynamics are summarized and a few remarks, which will prove useful throughout the thesis, are collected.

Part II, “Helical Grad-Shafranov equation”.

In **chapter 4**, the helical Grad-Shafranov equation is briefly derived, the Fourier-transformed equation is introduced, and the analytical properties of the helical Grad-Shafranov problem and solutions are discussed. In **chapter 5**, the proposed iterative solution technique for the helical Grad-Shafranov equation is introduced, and the main steps of the solution algorithm are discussed. In **chapter 6**, the Fortran implementation of the iterative algorithm is characterized and the computation is discussed from a numerical point of view. In **chapter 7**, a convergence analysis is carried out in order to discuss the most important internal parameters of the Fortran code. In **chapter 8**, finally, the Fortran code is applied to two different experimental configurations and the results are discussed in detail.

Part III, “VMEC and V3FIT”.

In **chapter 9**, the three-dimensional VMEC and V3FIT codes are introduced and their main features are discussed. In **chapter 10**, the benchmark of the helical Grad-Shafranov solver against both VMEC and V3FIT is carried out as a validation of the Fortran code. In **chapter 11**, the implementation of a new diagnostic for V3FIT is discussed.

Part IV, “Conclusions”.

In the final chapter the main results of the development and application of the two- and three-dimensional tools developed in the previous parts are summarised and discussed.

Prefazione

Il presente elaborato è il risultato di un progetto di tre anni svolto presso il Consorzio RFX come dottorato di ricerca sui plasmi a confinamento magnetico.

La ricerca sulla fusione termonucleare controllata, infatti, è attualmente perseguita da molte nazioni nel modo, grazie alla promessa di una fonte di energia abbondante e pressoché pulita. I prossimi passaggi della comunità internazionale sono la costruzione e l'operazione di un grande dispositivo, ITER, considerato come l'ultimo esperimento di fisica per la fusione per quel che riguarda la configurazione tokamak. Dopo ITER, infatti, è previsto il primo protoreattore commerciale, DEMO, che dovrebbe dimostrare la fattibilità della fusione come fonte energetica. La comunità stellarator sta costruendo una nuova macchina, Wendelstein 7-X, che fornirà ulteriori spunti per la fisica tridimensionale.

Tra i vari dispositivi per la fusione, il Reversed-Field Pinch è stato dimostrato essere, se non un dispositivo praticabile per la produzione commerciale di energia, un ottimo strumento per lo studio della fisica del plasma. L'esperimento RFX-mod situato presso il Consorzio RFX a Padova, in Italia, è la macchina RFP più grande del mondo e rappresenta il dispositivo fusionistico più avanzato per quel che riguarda la stabilizzazione attiva di perturbazioni magnetoidrodinamiche attraverso controllo in retroazione. I ricercatori di RFX-mod, inoltre, hanno studiato dapprima teoricamente e poi sperimentalmente il concetto essenziale di auto-organizzazione negli RFP, che produce regimi di confinamento migliorato contraddistinti da trasporto migliorato ed un livello ridotto di caos magnetico. I modi *tearing* sono noti per essere i protagonisti dei meccanismi di dinamo responsabili delle deformazioni elicoidali e dei regimi migliorati.

In uno scenario così complesso, la ricostruzione dei modi *tearing* dentro al plasma attraverso misurazioni esterne è estremamente importante per ragioni sia modellistiche che sperimentali, dal momento che le strutture che influenzano le proprietà di trasporto nei plasmi sono in parte collegate proprio ai modi *tearing*.

Il presente elaborato, in particolare, si occupa di sviluppo di codici bidimensionali e tridimensionali per la risoluzione di equilibri.

Come primo problema è stato sviluppato un codice Fortran per la risoluzione numerica dell'equazione elicoidale di Grad-Shafranov, che è un'equazione di equilibrio bidimensionale derivata sotto l'assunzione di simmetria elicoidale. Tali assunzioni si scoprono essere particolarmente appropriate per lo studio del modo *tearing* dominante in RFX-mod durante gli stati ciclici di quasi-singola-elicità in configurazione RFP, ma possono essere applicate anche alla configurazione tokamak.

Come secondo problema sono stati analizzati e studiati i codici tridimensionali VMEC e V3FIT per la ricostruzione di equilibri. Il codice per la soluzione della Grad-Shafranov elicoidale è stato testato contro le predizioni tridimensionali di VMEC e V3FIT, svolgendo un fruttuoso confronto. Quindi, come ulteriore passaggio nell'applicazione del codice V3FIT ad RFX-mod in modalità *fixed-boundary*, è stata implementata una nuova diagnostica virtuale, che precedentemente è stata dimostrata essere in grado di risolvere l'inconsistenza nel valore al bordo per il fattore di sicurezza.

La tesi è organizzata come segue.

Parte I, "Introduction".

Nel **capitolo 1** si introduce la fusione termonucleare controllata come possibile fonte di energia, e si discutono le nozioni di base della fisica della fusione. Nel **capitolo 2** si discutono gli aspetti più importanti della fisica della fusione, sia per i dispositivi a campo rovesciato sia per i tokamak, e si introducono i concetti di auto-organizzazione ed effetto dinamo come ragione per lo studio della fisica tridimensionale e delle ricostruzioni per i modi *tearing*. Nel **capitolo 3** si riassumono le equazioni generali della magnetoidrodinamica e si riportano alcune considerazioni che si riveleranno essenziali nello sviluppo della tesi.

Parte II, "Helical Grad-Shafranov equation".

Nel **capitolo 4** si deriva rapidamente l'equazione di Grad-Shafranov elicoidale, si introduce l'equazione trasformata secondo Fourier e si discutono le proprietà analitiche del problema elicoidale di Grad-Shafranov e le sue soluzioni. Nel **capitolo 5** si introduce il meccanismo iterativo di soluzione per l'equazione di Grad-Shafranov elicoidale e si discutono i passaggi principali dell'algoritmo risolutivo. Nel **capitolo 6** si descrive l'implementazione in Fortran dell'algoritmo iterativo e si discute il calcolo della soluzione da un punto di vista numerico. Nel **capitolo 7** si effettua un'analisi di convergenza, in modo da presentare i parametri più importanti del codice Fortran. Nel **capitolo 8**, infine, si applica il codice Fortran a due configurazioni sperimentali differenti e se discutono i risultati in dettaglio.

Parte III, "VMEC and V3FIT".

Nel **capitolo 9** si introducono i codici tridimensionali VMEC e V3FIT e si discutono le loro principali caratteristiche. Nel **capitolo 10** il risultato di Grad-Shafranov elicoidale è confrontato sia con VMEC che con V3FIT, come validazione del codice Fortran. Nel **capitolo 11** si discute l'implementazione di una nuova diagnostica per V3FIT.

Parte IV, "Conclusions".

Nel capitolo conclusivo sono discussi i risultati principali dello sviluppo e dell'applicazione degli strumenti bidimensionali e tridimensionali dei capitoli precedenti.

Part I

Introduction

CHAPTER 1

Fusion basics

This chapter is devoted to the introduction of nuclear fusion as an energy source, to the characterization of the main properties of a nuclear reactor and to the overview of the magnetic confinement concept.

1.1 Fusion and fission

The possibility of a net energy release through nuclear reactions follows from the dependence of the binding energy per nucleon on the atomic number for the nuclei of the principal elements, as plotted in figure 1.1.

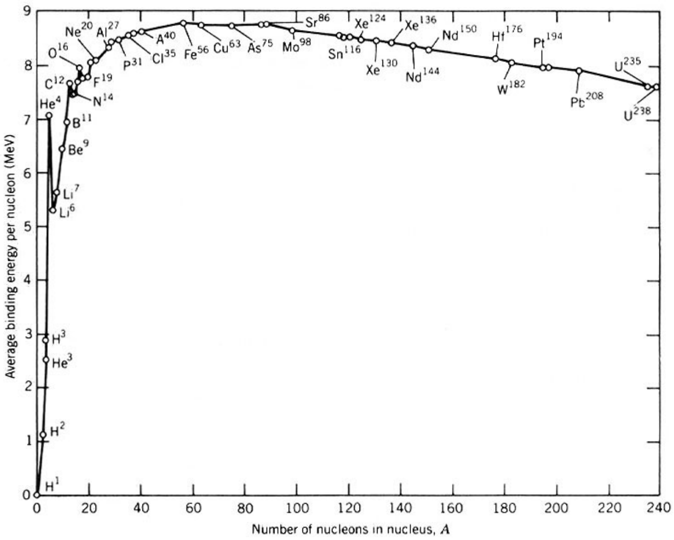

Figure 1.1: Average binding energy per nucleon as a function of the number of nucleons in the nuclei of the main elements.

Nuclear fission consists in breaking down a heavy nucleus to form lighter (and more bound) nuclei, and has the outcome of releasing as kinetic energy the mass defect of the reaction, that is, the mass difference between reagents and products. Typical mass defect for a nuclear fission reaction is 1 MeV per nucleon.

Nuclear fusion goes the opposite way around, that is, lighter nuclei are glued together to form a heavier (and more bound) nucleus, therefore exploiting the steep initial shoulder of the piecewise of figure 1.1 rather than the soft slant at high mass number. Typical mass defect for a nuclear fusion reaction is 7 MeV per nucleon.

Given the different feasibility in terms of engineering challenges, commercial reactors nowadays are based on the fission concept, while fusion reactors are still in a research and development phase.

There is a lot of expectation about the harnessing of nuclear fusion power, since fusion reactors would be cleaner and more secure than fission ones. Fusion reactions do not involve highly radioactive elements and would therefore not lead to nuclear waste, but only to radioactive activation of part of the reactor materials due to impact of energetic neutrons. Fission reactors, on the other hand, exploit the first few steps in the long-lived radioactive chains of uranium and plutonium, so that nuclear wastes have to be treated with particular care. Finally, fusion power plants would not pose serious threats to the environment, compared to those linked with fission plants like out-of-control chain reactions.

1.2 Fusion reactions

Nuclear fusion is a fundamental process in astrophysics, being one of the few mechanisms able to act against the gravitational pull of stars: fusion reactions, in fact, lead to a dynamic equilibrium between gravitational energy and kinetic thermal energy in stellar nuclei.

The stars like the Sun, which are in the hydrogen-burning stage, build helium starting from protons through the so-called ‘proton-proton chain’, consisting in three successive reactions,

$$\mathrm{p} + \mathrm{p} \longrightarrow {}^{2}\mathrm{D} + \mathrm{e}^{+} + \nu_{\mathrm{e}}, \tag{1.1a}$$

$$ {}^{2}\mathrm{D} + \mathrm{p} \longrightarrow {}^{3}\mathrm{He} + \gamma, \tag{1.1b}$$

$$ {}^{3}\mathrm{He} + {}^{3}\mathrm{He} \longrightarrow {}^{4}\mathrm{He} + \mathrm{p} + \mathrm{p}. \tag{1.1c}$$

Notice that (1.1a) is weak nuclear, (1.1b) is electomagnetic and (1.1c) is strong nuclear: inside the stars there is sufficient density to balance the extremely low cross section characterising the weak nuclear force and to have a significant deuterium production from (1.1a), whereas on Earth the same is not feasible. The proton-proton chain is not exploitable from an energy production point of view, therefore single-stage reactions have to be considered.

The main nuclear fusion reactions involve the light elements like hydrogen and helium, and more precisely their nuclei p and ${}^{4}\mathrm{He}$, together with their isotopes deuterium ${}^{2}\mathrm{D}$, tritium ${}^{3}\mathrm{T}$, and helium-3 ${}^{3}\mathrm{He}$. The kinetic energy relative to each product, according to the law of conservation of momentum, is written in parentheses.

$$
\begin{aligned}
{}^{2}\mathrm{D} + {}^{2}\mathrm{D} &\longrightarrow {}^{3}\mathrm{T}(1.01\,\mathrm{MeV}) + \mathrm{p}(3.02\,\mathrm{MeV}), && (1.2a)\\
{}^{2}\mathrm{D} + {}^{2}\mathrm{D} &\longrightarrow {}^{3}\mathrm{He}(0.82\,\mathrm{MeV}) + \mathrm{n}(2.45\,\mathrm{MeV}), && (1.2b)\\
{}^{2}\mathrm{D} + {}^{3}\mathrm{T} &\longrightarrow {}^{4}\mathrm{He}(3.56\,\mathrm{MeV}) + \mathrm{n}(14.03\,\mathrm{MeV}), && (1.2c)\\
{}^{2}\mathrm{D} + {}^{3}\mathrm{He} &\longrightarrow {}^{4}\mathrm{He}(3.71\,\mathrm{MeV}) + \mathrm{p}(14.64\,\mathrm{MeV}). && (1.2d)
\end{aligned}
$$

Using heavier reagents would not be convenient, since that would mean a higher Coulomb barrier and one would obtain less energy for each reaction.

In order to choose which one among the (1.2) reactions is the best candidate for a future fusion power plant, the cross sections have to be considered.

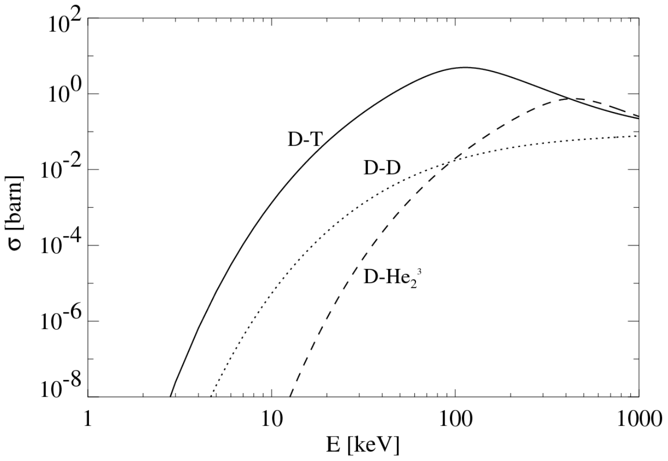

Figure 1.2: Cross sections of the (1.2) reactions as a function of energy.

Figure 1.2 shows how, for temperatures between 20 and 100 keV, the reaction (1.2c) exhibits a cross section higher than the other reactions by two orders of magnitude.

Regarding the availability of the reagents, one should consider that deuterium is present in the oceans in ratio 1:6400 with hydrogen, and that tritium is radioactive and unstable, but can be nonetheless obtained from litium,

$$
{}^{6}\mathrm{Li} + \mathrm{n} \longrightarrow {}^{4}\mathrm{He}(2.10\,\mathrm{MeV}) + {}^{3}\mathrm{T}(2.70\,\mathrm{MeV}). \tag{1.3}
$$

Litium itself is abundant on Earth, at approximately 20 mg per kg of Earth crust. One could therefore summarize that the reagents of (1.2c) are so abundant on Earth that power plant operation would be assured for hundreds of years. Such availability could be considered unlimited if compared to that of the fission reagents.

1.3 Ignition criterion

The energy balance in a fusion reactor will be determined by the equilibrium between energy production mechanisms (e.g.: fusion reactions, heating systems) and energy loss mechanisms (e.g.: transport loss, Brehmstrahlung loss).

The goal of a fusion power plant will be to reach a condition where external heating systems will not be required anymore, since the power of the α particles due to fusion reactions will balance the energy losses: above such threshold energy production will become feasible. This condition, known as 'ignition criterion', is typically expressed as an inequality on the triple product of three important factors: temperature T, density n and the characteristic energy confinement time τ_E,

$$n\,\tau_E\,T > 3 \cdot 10^{21}\,\mathrm{m}^{-3}\,\mathrm{keV\,s}. \tag{1.4}$$

From figure 1.3, visualization of eq. (1.4), one could deduce that the optimal working temperature is around 20 keV, corresponding to the minimum of the double product $n\tau_E$.

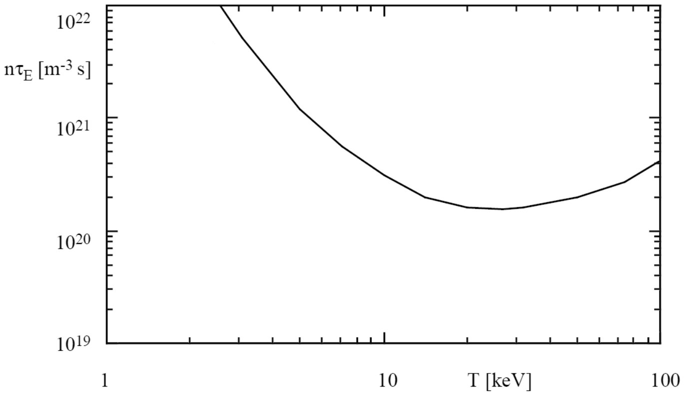

Figure 1.3: The ignition condition in the $(T, n\tau_E)$ plane.

On the other hand, engineering issues influence n: for a fusion power plant based on plasma confinement, the unavoidable plasma-wall interaction limits the density to values lower than $10^{20}\,\mathrm{m}^{-3}$ so as to avoid that the plasma facing components would be targeted by an extreme power flux. Eq. (1.4) then leads to an energy confinement time $\tau_E \sim 1\,\mathrm{s}$ for a successful ignition.

1.4 Toroidal devices

In order for the plasma to remain in density and temperature conditions favorable for energy production, it has to be confined long enough. Three confinement methods are known: gravitational, magnetic and inertial – the last two being actively pursued on Earth – nonetheless only magnetic confinement will be discussed in this thesis.

A charged particle moving inside a magnetic field spirals around the magnetic field lines, according to orbit theory. More precisely, it exhibits the superposition of a uniform motion in the direction parallel to the magnetic field and of a circolar uniform motion in the plane normal to the magnetic field, with a

Larmor gyration radius r_L and a cyclotron pulse ω_c,

$$r_L = \frac{mv_\perp}{|q|B}, \tag{1.5a}$$

$$\omega_c = \frac{|q|B}{m}. \tag{1.5b}$$

Thanks to careful tailoring of the magnetic configuration, one can therefore confine particles in a finite region of space. Cylindrical machines (e.g.: the magnetic bottle) are able to confine particles in the plane orthogonal to the magnetic field, but they can not avoid parallel dispersion phenomena near the edges: for such reason toroidal configurations are usually preferred, since every flux surface closes down on itself. The path of the charged particles around the magnetic field lines is shown in figure 1.4.

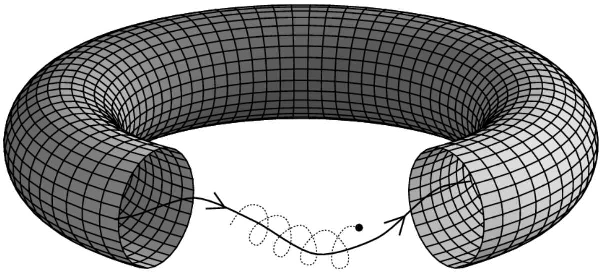

Figure 1.4: Spiral motion of a charged particle along a helical magnetic field line in a typical toroidal device.

Three main types of toroidal machines for magnetic confinement of fusion plasmas can be introduced: let us briefly introduce each one.

1.4.1 Tokamak

The main option for a fusion device is called ‘tokamak’ – acronym from the russian for “toroidal chamber with magnetic coils” – which has been chosen as the configuration for the International Thermonuclear Experimental Reactor (ITER). It is an axisymmetric toroidal device where the toroidal magnetic field, produced by the external coils in the direction along the torus, is much more intense than the poloidal field, produced by the plasma itself in the plane orthogonal to the toroidal direction.

The axisymmetric tokamak configuration can be represented as in figure 1.5.

1.4.2 Reversed-field pinch

Similarly to the tokamak configuration, the ‘reversed-field pinch’ (RFP) configuration is an axisymmetric toroidal device with a superposition of a toroidal and a poloidal magnetic field. Its main characteristics, however, are that the two magnetic components are of comparable intensity and that, moreover, the toroidal component reverses near the plasma edge.

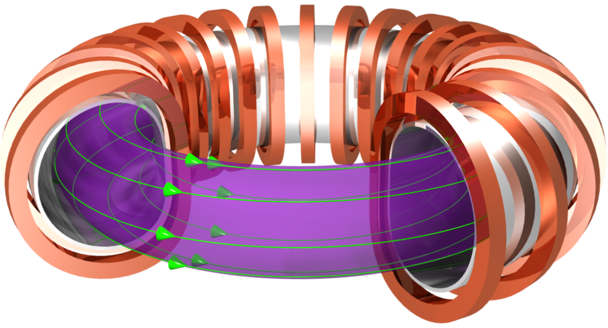

Figure 1.5: Three-dimensional representation of an axisymmetric toroidal device.

1.4.3 Stellarator

The ‘stellarator’ is the only type of device which is not axisymmetric. Its magnetic field is purely helical and inherently three-dimensional, and is produced by a complex setup of external coils. A further difference with respect to tokamaks and RFPs is that in a stellarator, usually, there is no plasma current.

Figure 1.6 shows the scheme for the Wendelstein 7-X stellarator, under construction at the Max-Planck Institute in Greifswald, Germany.

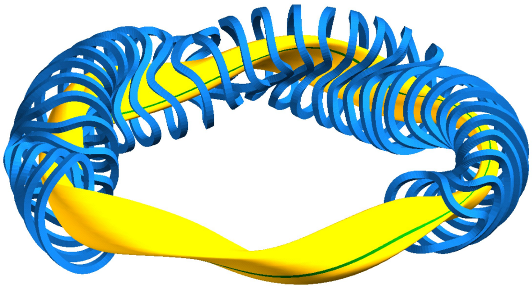

Figure 1.6: The complex setup of the external magnetic coils (blue) is plotted together with one plasma flux surface (yellow) for the Wendelstein 7-X device.

CHAPTER 2

Fusion physics

This chapter briefly introduces the two magnetic confinement devices studied in the following chapters, and discusses the importance of the analysed MHD modes in the RFP dynamics.

2.1 Equilibrium and stability

Curvilinear coordinates (r, θ, ϕ) are typically exploited to parameterize a toroidal device, as plotted in figure 2.1, where r is the minor radius, θ is the angle in the poloidal direction and ϕ is the angle in the toroidal direction.

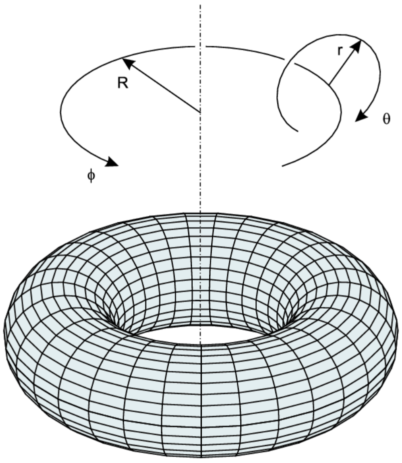

Figure 2.1: The (r, θ, ϕ) coordinate system exploited to parameterize a toroidal device.

As previously stated, the main difference between the two introduced axisymmetric configurations is the profile of each component of the magnetic field $\mathbf{B}$. In particular, while for the tokamak the toroidal component is much higher than the poloidal one, for the RFP they are of comparable amplitude. Figure 2.2 shows the typical profiles of both B_θ and B_ϕ in a tokamak and a RFP machine as a function of the radius r.

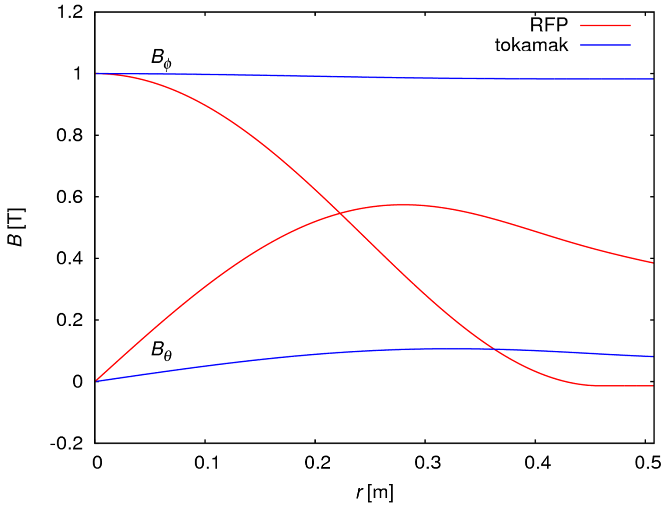

Figure 2.2: Typical radial profiles for the B_θ and B_ϕ components for the equilibrium of a tokamak and a RFP.

Generally, two important dimensionless variables are introduced to characterise RFP equilibria: the 'reversal' parameter F and the 'pinch' parameter Θ,

$$F = B_\phi(a)/\langle B_\phi \rangle, \tag{2.1a}$$

$$\Theta = B_\theta(a)/\langle B_\phi \rangle, \tag{2.1b}$$

where a is the plasma radius, and $\langle \cdot \rangle$ is the average on the poloidal section. Both variables will prove extremely useful in the description of the operational RFP equilibria in RFX-mod, but will not be significant in the description of tokamak equilibria, given the relative magnitude of the magnetic field components in such a configuration.

The existence of a reversed-field equilibrium with $F < 0$ can be found in the classic relaxation theory by Taylor through a procedure of magnetic energy minimization with conserved helicity [Ort93]. The reversal of the toroidal field, in fact, gives good stability properties to the configuration with respect to MHD-related perturbations.

The stability of a toroidal configuration can be analysed through the cylindrical safety factor,

$$q(r) = \frac{r}{R_0} \frac{B_\phi(r)}{B_\theta(r)}, \tag{2.2}$$

where r is the radial coordinate and R_0 is the major radius of the torus. The safety factor measures the toroidal loops needed by a field line to complete a poloidal loop.

Furthermore, by introducing a Fourier decomposition of the perturbations present upon the equilibrium, and by assuming an angular dependence

$$\mathbf{b}(r, \theta, \phi) = \mathbf{b}^{m,n}(r) \, \exp i(m\theta - n\phi) + c.c., \tag{2.3}$$

one could promptly see that the resonance condition

$$q(r_s^{m,n}) = \frac{m}{n}, \tag{2.4}$$

corresponds to the situation in which the magnetic perturbation and the field lines have the same pitch.

The resonance condition helps the growth of MHD instabilities: for example, in the Newcomb equation it corresponds to the vanishing of the line-bending term and of its stabilizing effect.

The analysis of the safety factor profile for the main magnetic configurations is therefore of paramount importance for a stability analysis. The typical $q(r)$ profiles for both a tokamak and a RFP are plotted in figure 2.3.

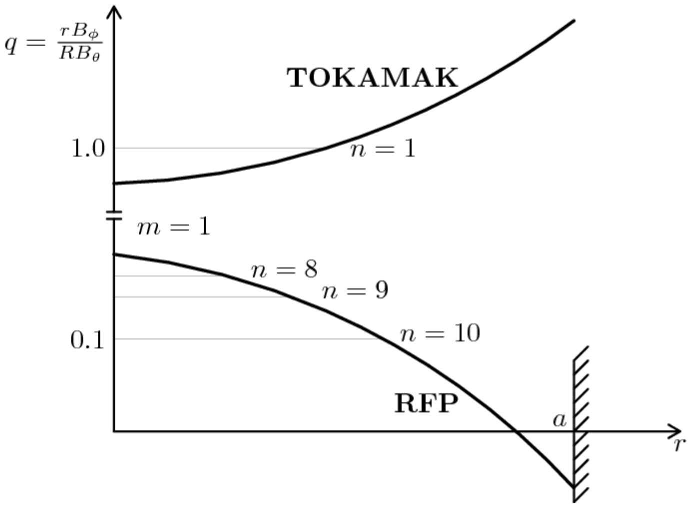

Figure 2.3: Typical safety factor profiles and $m = 1$ resonances for a tokamak and a RFP.

2.1.1 Tokamak

First, note that for the tokamak configuration the $m = 0$ modes, which are sausage distortions of the plasma column, are intrinsically stabilized, since the stability condition $q \neq 0$ is satisfied everywhere. A more detailed analysis yields the 'Wesson condition' [Wes04] as the stability region for the safety factor,

$$q(0) \geq 1, \tag{2.5a}$$

$$\frac{q(a)}{q(0)} \geq 3. \tag{2.5b}$$

For $q(0) \approx 1$ and for typical aspect ratios, e.g. $R_0/a > 3$, eq. (2.5b) means that the toroidal component of the magnetic field has to be at least one order of magnitude bigger that the poloidal component.

The Wesson condition (2.5b), moreover, corresponds to a maximum value for the achievable plasma current, which in turn limits the maximum plasma heating by Joule effect, that could be insufficient to cross the ignition threshold.

In tokamak devices, in fact, additional heating systems are typically envisaged, like neutral beam heating or radiofrequency heating.

As a final remark, an analysis of the β factors,

$$\beta_\theta = \frac{\langle p \rangle}{B_\theta^2(a)/2\mu_0} \sim 1, \tag{2.6a}$$

$$\langle \beta \rangle = \frac{\langle p \rangle}{B^2(a)/2\mu_0} \sim 0.01, \tag{2.6b}$$

where p is the kinetic pressure and $B^2/2\mu_0$ represents the magnetic pressure, highlights that the pressure is confined mainly by the poloidal field B_θ, while the toroidal field provides a stabilizing effect to the configuration.

2.1.2 Reversed-field pinch

The stability of a RFP device is completely different from the one of a tokamak.

The safety factor is still monotonous, in fact, but exhibits the maximum on the magnetic axis and decreases towards the plasma edge, where it reverses, so that outside the reversal surface the toroidal field is negative. The RFP is therefore much more sensitive than the tokamak to a lot of MHD modes. For example, the reversal region corresponds to the resonance of the $m = 0$ modes, whereas the internal region is typically characterized by the presence of the resonances for the $m = 1$ modes which are unstable tearing modes destabilized by the current gradient, that will be discussed in subsection 2.2.4.

On the other hand it can be ignited by Ohmic heating only, since there is no limit on the achievable plasma current, and it is characterized by lower magnetic fields, which can be produced avoiding superconductors and therefore leading to a significant budget difference.

2.2 Self-organization in the RFP

One of the most interesting features of a RFP device is the natural self-organization exhibited by its dynamics, analogous to the dynamo mechanisms typically observed in stars. The uttermost importance of the tearing modes in the RFP self-organization suggests to briefly introduce the astrophysical dynamo and Cowling's theorem.

2.2.1 Astrophysical dynamo

Geophysical and astrophysical observations show that the magnetic fields on Earth, or on the Sun, are maintained much longer than what would be expected considering resistive diffusion. In the case of the Sun, moreover, it is not at all straightforward to explain the eleven-year magnetic cycle. Self-sustaining phenomena, known as 'dynamos', are therefore exploited to explain the small-scale generation mechanisms that act against ohmic dissipation.

In the core of the Sun, for example, there appears to be a cycle between the toroidal and the poloidal component of the magnetic field: the generation of toroidal field starting from poloidal field is due to differential rotation, while turbulent convection phenomena convert poloidal field into toroidal field. The astrophysical dynamo is typically explained in terms of turbulent dynamo.

2.2.2 Cowling's theorem

Cowling's anti-dynamo theorem asserts that "axisymmetric magnetic configurations cannot be maintained by velocity fields symmetric with respect to the same axis."

Cowling's theorem can be applied to a RFP device: one can demonstrate that an axisymmetric field-reversed configuration cannot be maintained in a stationary state without some kind of magnetic dynamo [Ort93]. Such consideration is the starting point for the understanding of the turbulent dynamo.

At the same time Cowling's theorem does not apply to non-axisymmetric equilibria, which have been studied theoretically and numerically in recent years. The underlying dynamo for such configurations is briefly introduced as laminar dynamo in subsection 2.2.5.

2.2.3 Turbolent dynamo

According to the turbulent dynamo theory, in order to generate the dynamo mechanism required by Cowling's theorem it is necessary to introduce magnetic perturbations upon the axisymmetric equilibrium.

Each quantity $\mathbf{w}$ can be separated in its mean field component $\mathbf{w}_{mf}$ and its zero-average turbulent component $\mathbf{w}'$,

$$\mathbf{w} = \mathbf{w}_{mf} + \mathbf{w}', \tag{2.7a}$$

$$\langle \mathbf{w}' \rangle = \mathbf{0}, \tag{2.7b}$$

where $\langle \cdot \rangle$ represents an unspecified average. In the equations describing the system then one can find non-linear terms, like $\langle \mathbf{v}' \times \mathbf{B}' \rangle$ or $\langle \mathbf{v}' \cdot \mathbf{v}' \rangle$, which account for turbulent stochastic phenomena and counter the resistive diffusion (so-called 'α-effect') or which modify the effective plasma resistivity ('β-effect').

The application of the turbulent dynamo theory to the RFP carries a few differences with respect to the standard astrophysical context.

The problem is highly non-linear: the approximation of 'cinematic dynamo', according to which the velocity field is fixed, cannot be exploited and one has to solve both Ohm's Law (3.6) and the momentum equation (3.4) in a general MHD context, so as to determine the $\mathbf{v}$ and $\mathbf{B}$ fields self-consistently.

Differently from what happens at astrophysical level, then, there is no need for a conversion mechanism that converts toroidal flux in poloidal flux, since the latter is continuously put into the system from external coils as plasma current.

The most important fluctuations of a RFP, moreover, are not small-scale turbulence fields but are rather superpositions of large-scale laminar motions. The net effect of such fluctuations on the mean field equations, nonetheless, is exactly the same, and in particular one can still recognize an α-effect, even if less conspicuous.

2.2.4 Tearing modes

The most important players in the dynamo mechanism of a RFP are the $m = 1$ tearing modes (see figure 2.3), which produce an effect similar to the astrophysical differential rotation and convert poloidal flux into toroidal flux.

The $m = 0$ modes, which resonate at the reversal surface, typically have much lower amplitudes and therefore contribute less to the dynamo, but their presence is extremely important nonetheless since they mediate non-linear couplings between $m = 1$ modes.

The turbulent dynamo regime can therefore be described as the simultaneous presence of lots of different $m = 0$ and $m = 1$ modes, and is generally labelled ‘Multiple Helicity’ (MH) regime (figure 2.4).

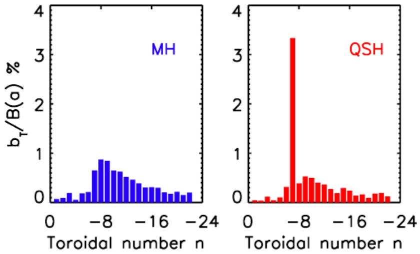

Figure 2.4: Typical spectrum for the $m = 1$ modes in RFX-mod in a state of Multiple Helicity (left panel) and Quasi Single Helicity (right panel).

Tearing modes are characterised by the fact that next to their resonant surface the finite plasma resistivity leads to ‘tearing’ of the magnetic field lines and reconnection of the flux surfaces with creation of magnetic islands and, more generally, modification of the magnetic topology. Reconnection phenomena cannot be described neglecting the finite plasma resistivity.

In the MH configuration, the overlapping of magnetic islands has the effect of producing magnetic chaos and reducing the confinement properties due to enhanced transport effects.

2.2.5 Laminar dynamo

Theoretical studies and numerical simulation recently led to postulating the existence of stationary Single Helicity (SH) configurations, where a single MHD mode dominates the spectrum together with its higher order harmonics [Lor09]. Such configuration corresponds to the possibility of a non-axisymmetric equilibrium, so that Cowling’s theorem would not apply. The self-organization mechanism is then called ‘laminar dynamo’ so as to distinguish it from the turbulent case, but it can be introduced analogously. The main difference is that the laminar dynamo leads to reduced magnetic chaos and enhanced confinement properties. In a SH state the plasma appears to be helically twisted, as in figure 2.5.

Figure 2.5: Three-dimensional visualization of a SH configuration in RFX-mod.

Even though the experimental realization of a SH configuration is yet to come, an intermediate state between MH and SH has been observed – and called a Quasi Single Helicity (QSH) state – where a dominant mode is present in the spectrum together with its higher order harmonics but where other helicities can be found as well, even if at a much lower amplitude, as in figure 2.4.

The main actor for the laminar dynamo is, once again, the resonant tearing mode producing the helical configuration. It is then understandable that a sufficiently detailed model for reconstructing the profile of such structures inside the plasma is extremely important in order to further improve the confinement, and would be positive from a diagnostic point of view.

2.3 RFX-mod

The Reversed-Field eXperiment (RFX) is the biggest RFP device in the world, and is hosted by the Italian National Research Council (CNR) in Padua.

Following the fire which occurred in the experiment hall in 1999, the RFX machine has been subject between 2000 and 2004 to various modifications and updates, among which the change of the conducting shell and the implementation of a new feedback control system [Son03]: the updated device is referred to as RFX-*mod*.

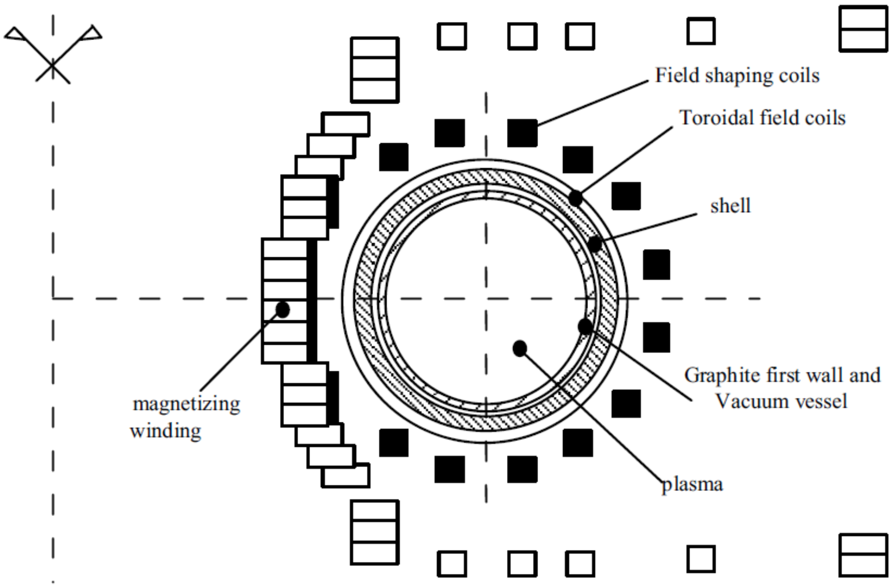

Figure 2.6: Cross section scheme for RFX: in RFX-mod the 65-millimeter aluminum shell has been replaced by a 3-millimeter copper shell.

The vacuum vessel in RFX-mod is toroidal in shape and its internal surface is fully covered by a set of graphite tiles. The vessel is enclosed in a thin stabilizing copper shell, which replaced the thick aluminum RFX shell, and a further structure supports the coils for plasma positioning and feedback control. The section of the device is plotted in figure 2.6, where the magnetizing winding, the field shaping coils and the toroidal field coils are shown, while the main physical characteristics of RFX-mod are summarized in table 2.1.

vacuum vessel	material	inconel-625
	major radius, R_0	1.995 m
	average minor radius, r_V	0.49 m
	thickness	0.03 m
	time constant, τ_V	3 ms
PFCs	material	graphite
	wall radius, a	0.459 m
	thickness	0.016 m
sensors' position	radial sensors, $r_{\text{sens},r}$	0.507 m
	toroidal sensors, $r_{\text{sens},\phi}$	0.508 m
conducting shell	material	copper
	internal minor radius, b	0.5115 m
	thickness	0.003 m
	time constant, τ_b	100 ms

Table 2.1: A few technical specifications of the RFX-mod experiment.

Figure 2.7 shows a three-dimensional representation of the coil system for RFX-mod, where the magnetizing, field shaping and toroidal coils are shown together with the 'PR' saddle coils, an array of 192 independently controlled coils representing the actuators of the feedback control system.

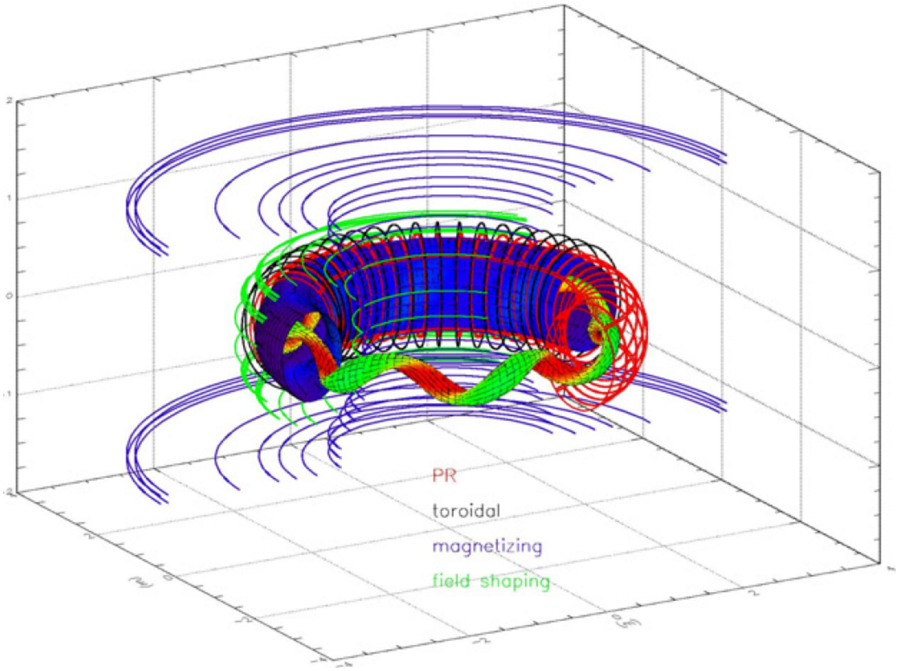

Figure 2.7: Three-dimensional modelling of the coil systems in RFX-mod from the point of view of the V3FIT code (from [Ter13]).

2.3.1 Diagnostics

Magnetic diagnostics

Let M and N be the poloidal and toroidal periodicities of the equally spaced probes, compactly written as MxN. The magnetic diagnostic setup consists of an array of 4x48 saddle coils for the integrated measurement of the radial magnetic field, 4x48 biaxial pick-up coils for the local measurement of both the poloidal and toroidal components, 8x4 probes for the measurement of the poloidal component with twice the poloidal definition, plus 10 toroidal and 8 poloidal flux loops, totalling 626 magnetic signals. The magnetic diagnostics, flux loops excluded, are plotted in figure 2.8.

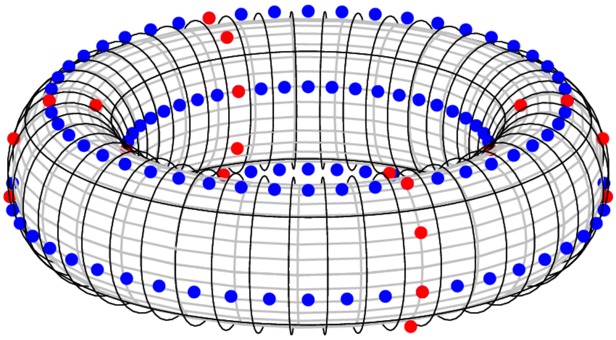

Figure 2.8: Partial plot of the magnetic diagnostics in RFX-mod: the vacuum vessel (gray) is covered by the 4x48 saddle coils (black), by the 4x48 poloidal and toroidal pick-up coils (blue) and by four toroidal positions where the poloidal field is measured with twice the poloidal periodicity (red).

The magnetic measurements will be exploited for the imposition of the helical Grad-Shafranov boundary conditions in subsection 6.4.7 and for the V3FIT simulations in chapter 10 and chapter 11.

It is important to stress that the exploited measurements are not the ‘raw’ values collected by the magnetic probes. Since the feedback active coils have the same 4x48 periodicity of the feedback probes, in fact, aliasing effects pollute the Fourier spectrum and induce systematic errors. A ‘cleaning’ system has therefore been devised so as to remove from the measurements the contributions due to the sideband harmonics produced by the control coils. Indeed, a much better feedback control of magnetic perturbations has been obtained with the Clean Mode Control (CMC) [Zan07].

For the helical Grad-Shafranov equation, in particular, the radial and toroidal components of the perturbed magnetic field will be acquired. Consistently with the Fourier expansion of eq. (2.3), they will be labelled

$$b_r^{m,n}(r = r_{\text{sens},r}), \qquad b_\phi^{m,n}(r = r_{\text{sens},\phi}), \tag{2.8}$$

or, more compactly,

$$b_r^{m,n}(r_{\text{sens}}), \qquad b_\phi^{m,n}(r_{\text{sens}}). \tag{2.9}$$

Kinetic diagnostics

The kinetic diagnostics, on the other hand, consists of a far-infrared interferometer [Inn97] for density measurements, four Soft X-Ray (SXR) fans [Fra01] for the measurement of the plasma emissivity and a Thomson scattering system [Alf07] for temperature measurements. The diagnostic signals provided by the three kinetic systems, plotted in figure 2.9, will be exploited in chapter 10 in the full V3FIT simulation.

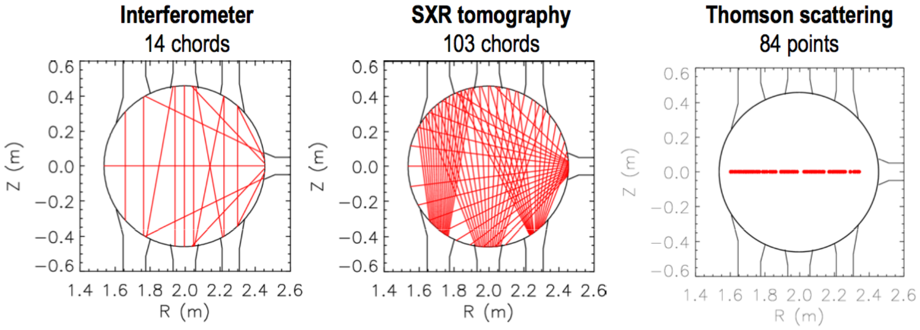

Figure 2.9: Plot of the kinetic diagnostics in RFX-mod, from [Ter13].

CHAPTER 3

Magnetohydrodynamics

This chapter will schematically introduce the main concepts of the MHD theory, upon which the helical Grad-Shafranov treatment is based.

3.1 General properties

As previously explained, the typical operating temperature in a fusion power plant will be around 20 keV. At such temperature matter is in the plasma state, that is, in a gaseous state which is globally neutral, but where electrons are ionized apart from the nuclei.

A plasma consists of two charged species – positively charged nuclei and negatively charged electrons – which can be separated for distances comparable to the 'Debye length',

$$\lambda_D = \sqrt{\frac{\varepsilon_0 k_B T_e}{n_e e^2}}. \tag{3.1}$$

If the separation exceeds the Debye length, an electrostatic field forms so as to prevent further charge separation, with characteristic time comparable to the inverse of the 'plasma frequency',

$$\frac{\omega_p}{2\pi} = \frac{1}{2\pi}\sqrt{\frac{n_e e^2}{m_e \varepsilon_0}}, \tag{3.2}$$

where n_e is the electron density, T_e electron temperature and m_e electron mass. Typical values for the Debye length are between micrometer and millimiter, while the plasma frequency is generally of the order of the gigahertz.

Likewise, a charged particle inside the plasma is screened by a buildup of opposite charges so that the effective Coulomb potential is screened with a decay length of λ_D. In order for the plasma to be considered globally neutral it is therefore necessary to consider a sufficiently large volume: the so-called 'quasi-neutrality' condition can be expressed, for example, by requiring that in the Debye sphere there be lots of particles,

$$n_e \cdot \frac{4}{3}\pi\lambda_d^3 \gg 1. \tag{3.3}$$

Summarizing, upon study of plasma phenomena which are varying in time slowly with respect to (3.2) and which are spacially large with respect to (3.1), the two charged species can be considered unitely as a single charged fluid.

3.2 Equations

The MagnetoHydroDynamics is therefore described by the system of equations,

$$\begin{aligned}
\rho\frac{\mathrm{d}\mathbf{v}}{\mathrm{d}t} &= \mathbf{J}\times\mathbf{B} - \nabla p + \rho\nu\nabla^2\mathbf{v} + \rho_c\mathbf{E}, && \text{(momentum eq.)} && (3.4)\\
\frac{\partial\rho}{\partial t} + \nabla\cdot(\rho\mathbf{v}) &= 0, && \text{(continuity eq.)} && (3.5)\\
\mathbf{E} &= \eta\mathbf{J} - \mathbf{v}\times\mathbf{B}, && \text{(Ohm's law)} && (3.6)\\
\nabla\cdot\mathbf{E} &= \frac{\rho_c}{\varepsilon_0}, && \text{(Poisson's eq.)} && (3.7)\\
\frac{\partial\mathbf{B}}{\partial t} &= -\nabla\times\mathbf{E}, && \text{(Faraday's law)} && (3.8)\\
\nabla\cdot\mathbf{B} &= 0, && \text{(solenoidality eq.)} && (3.9)\\
\mu_0\mathbf{J} &= \nabla\times\mathbf{B} - \mu_0\varepsilon_0\frac{\partial\mathbf{E}}{\partial t}, && \text{(Ampère's law)} && (3.10)
\end{aligned}$$

where $\mathrm{d}/\mathrm{d}t$ represents a convective derivation,

$$\frac{\mathrm{d}}{\mathrm{d}t} = \frac{\partial}{\partial t} + (\mathbf{v}\cdot\nabla), \tag{3.11}$$

and ρ is the plasma mass density, ρ_c the charge density, $\mathbf{v}$ the velocity, $\mathbf{J}$ the current density, $\mathbf{B}$ the magnetic field, p the pressure, ν the viscosity, $\mathbf{E}$ the electric field and η the resistivity. In order to get a self-consistent system, the equations (3.4)–(3.10) have to be coupled to an equation of state for p.

3.3 Assumptions

The quasi-neutrality condition means that the $\rho_c\mathbf{E}$ term in the momentum equation can be neglected.

The characteristic velocities are much lower than the speed of light, therefore we neglect relativistic effects like the term $\mu_0\varepsilon_0\partial\mathbf{E}/\partial t$ in Ampère's law.

Furthermore, Poisson's equation is decoupled from the system and can be independently solved for ρ_c once $\mathbf{E}$ is known.

The electric field itself is not an independent variable of the system, since it is computed through Ohm's law by knowing the $\mathbf{v}$ and $\mathbf{B}$ fields.

Finally, a non-viscous plasma is considered, $\nu = 0$, and pressure is neglected given the present low β_θ plasma of RFX-mod for the RFP case, $\beta_\theta \lesssim 5\%$.

Such simplifications yield for the momentum equation (3.4)

$$\rho\frac{\mathrm{d}\mathbf{v}}{\mathrm{d}t} = \mathbf{J}\times\mathbf{B}. \tag{3.12}$$

In order to assess the relative weight of each term in (3.12), it is useful to carry out a dimensional analysis. Therefore, let $\widehat{\mathbf{Q}}$ be a unit vector corresponding to each $\mathbf{Q}$ quantity (with module Q),

$$\widehat{\mathbf{B}} = \frac{\mathbf{B}}{B}, \tag{3.13a}$$

$$\widehat{\mathbf{v}} = \frac{\mathbf{v}}{v}, \tag{3.13b}$$

and let

$$\widehat{\mathbf{J}} = \frac{\mathbf{J}}{J}, \tag{3.14a}$$

$$\widehat{\nabla} = \frac{\nabla}{1/a}, \tag{3.14b}$$

$$\frac{\partial}{\partial \hat{t}} = \frac{1}{1/\tau}\frac{\partial}{\partial t} = \frac{a}{v}\frac{\partial}{\partial t}, \tag{3.14c}$$

where a is the plasma radius, τ the characteristic time of the perturbation and $v = a/\tau$ the characteristic velocity. Let then v_A and τ_A be the Alfvén velocity and time,

$$v_A = \sqrt{\frac{B^2}{\mu_0 \rho}}, \tag{3.15a}$$

$$\tau_A = \frac{a}{v_A}. \tag{3.15b}$$

From Ampère's law

$$\widehat{\mathbf{J}} = \widehat{\nabla} \times \widehat{\mathbf{B}}, \tag{3.16a}$$

$$J = \frac{B}{a\mu_0}, \tag{3.16b}$$

so that, through trivial algebraic substitutions, the force balance equation (3.12) yields

$$\left(\frac{v}{v_A}\right)^2 \left[\frac{\partial \widehat{\mathbf{v}}}{\partial \hat{t}} + (\widehat{\mathbf{v}} \cdot \widehat{\nabla})\widehat{\mathbf{v}}\right] = \widehat{\mathbf{J}} \times \widehat{\mathbf{B}}. \tag{3.17}$$

It is clear that whenever

$$v \ll v_A, \tag{3.18}$$

the convective term can be neglected and eq. (3.12) becomes the equilibrium equation

$$\mathbf{J} \times \mathbf{B} = \mathbf{0}. \tag{3.19}$$

The tearing instabilities which have been considered in this thesis grow on a characteristic time scale which is between the Alfvén time τ_A and the resistive diffusion time

$$\tau_R = \frac{\mu_0 a^2}{\eta}. \tag{3.20}$$

The ratio between the two is known as 'Lundquist number', and is typically very large for fusion plasmas,

$$S = \frac{\tau_R}{\tau_A} \sim 10^6, \tag{3.21}$$

so that the condition (3.18) stands. The force balance equation then shows that $\mathbf{J}$ and $\mathbf{B}$ are decoupled from the other MHD variables and that they can be computed by a 'reduced MHD model',

$$\nabla \cdot \mathbf{B} = 0, \tag{3.22a}$$
$$\nabla \times \mathbf{B} = \mu_0 \mathbf{J}, \tag{3.22b}$$
$$\mathbf{J} \times \mathbf{B} = \mathbf{0}. \tag{3.22c}$$

Note that the $\eta = 0$ assumption for ideal MHD has *not* been exploited anywhere, so that Ohm's law is still (3.6).

Moreover, the magnetic vector potential $\mathbf{A}$, which generates $\mathbf{B}$ through

$$\mathbf{B} = \nabla \times \mathbf{A}, \tag{3.23}$$

and which therefore yields eq. (3.22a), is subject to the gauge condition $A_r = 0$.

3.4 Remarks

The reduced MHD system (3.22) is valid for every magnetic perturbation for which eq. (3.18) stands: among these one can find, as already explained, tearing perturbations but also the so-called resistive wall modes. These are ideal non-resonant perturbations that in case of ideal conducting shell would be perfectly stabilized, but that grow due to the effect of the finite resistivity of the shell and indeed evolve on a time scale comparable to that of the shell itself, around 100 ms for RFX-mod.

The reduced MHD model can be exploited to analyse the radial profile of the magnetic field even in non-equilibrium conditions, as long as eq. (3.18) stands. Since the system (3.22) is scale-invariant, however, additional physics has to be considered to predict the amplitudes and the dynamics of such perturbations. Typically, Ohm's law (3.6) and Faraday's law (3.8) are used to supply the missing information, but in the following chapter the extra physics will be supplied by enforcing external magnetic measurements as boundary conditions.

Part II

Helical Grad-Shafranov equation

CHAPTER 4

Helical equation

This chapter will discuss the helical Grad-Shafranov equation from a theoretical point of view, starting from the results of the MHD theory introduced in chapter 3. Closely following the 1992 paper by Finn, Nebel and Bathke [Fin92], the main steps in the derivation of the equation, together with its properties, will be introduced and discussed.

4.1 Derivation

4.1.1 Geometry

Let us start from a cylindrical coordinate system (r, ϑ, z) describing a linearized torus, that is, a torus with infinite aspect ratio.

The linear coordinate z, describing the direction along the cylinder, has period $2\pi R_0$ (where R_0 is the major radius) and can thus be replaced by an angle-like coordinate ϕ. Consequently, every derivation with respect to z can be replaced by an angle-like derivation with respect to ϕ,

$$z \quad \rightarrow \quad R_0\,\phi, \tag{4.1a}$$

$$\mathrm{d}z \quad \rightarrow \quad R_0\,\mathrm{d}\phi, \tag{4.1b}$$

$$\frac{\partial}{\partial z} \quad \rightarrow \quad \frac{1}{R_0}\frac{\partial}{\partial \phi}. \tag{4.1c}$$

The cylinder is therefore described by cylindrical coordinates (r, ϑ, ϕ). It is important to stress that even if we consider ϕ a toroidal angle, it is really the linear coordinate z and therefore no toroidal effects are included in such model.

4.1.2 Symmetry

The symmetry assumption is that of *helical* symmetry, promptly defined by the requirement that in the MHD spectrum there be a single dominant m, n mode together with its higher order harmonics. The Single Helicity configuration has been introduced in subsection 2.2.5.

It is straightforward to notice that the physical angular dependence is upon a 'helical angle' $u \equiv m\vartheta - n\phi$, not upon the two angle coordinates separately, and thus each quantity is completely determined by its (r,u) dependence and can therefore be decomposed as a Fourier series in terms of a single 'helical mode number' q,

$$\mathbf{B}(r,u) = \mathbf{B}^0(r) + \sum_q \mathbf{b}^q(r)\,\mathrm{e}^{iqu} + c.c.. \tag{4.2}$$

In RFX-mod the most internally resonant mode, the $m=1, n=7$ tearing, is the dominant mode $q=1$ that determines the helicity of the SH state, while its higher order harmonics correspond to higher q numbers (e.g.: $q=2$ means $m=2, n=14$, etc).

4.2 Grad-Shafranov equation

The starting point is the 'reduced MHD' system (3.22), introduced in section 3.3. Let us write it again,

$$\nabla\cdot\mathbf{B} = 0, \tag{4.3a}$$

$$\nabla\times\mathbf{B} = \mathbf{j}, \tag{4.3b}$$

$$\mathbf{j}\times\mathbf{B} = \mathbf{0}. \tag{4.3c}$$

In terms of the 'helical flux' χ and the 'helical field' g, with gauge (3.23),

$$\chi = mA_\phi + n\varepsilon A_\vartheta, \tag{4.4a}$$

$$g = mB_\phi + n\varepsilon B_\vartheta, \tag{4.4b}$$

the magnetic field has the representation

$$\mathbf{B}(r,u) = f(r)\nabla\chi(r,u)\times\mathbf{d}(r) + f(r)\,g(r,u)\,\mathbf{d}(r), \tag{4.5}$$

where

$$\varepsilon(r) = r/R_0, \tag{4.6a}$$

$$f(r) = r/(m^2+n^2\varepsilon^2), \tag{4.6b}$$

$$\mathbf{d}(r) = \hat{r}\times\nabla u. \tag{4.6c}$$

The Grad-Shafranov equation derives from (4.3) and can be shown to take the helical form:

$$\frac{1}{f}\frac{\partial}{\partial r}\left(f\frac{\partial\chi}{\partial r}\right) + \frac{1}{rf}\frac{\partial^2\chi}{\partial u^2} = \beta g(\chi) - g\,\frac{\mathrm{d}g}{\mathrm{d}\chi}, \qquad \text{(HGS)} \tag{4.7}$$

with $\beta = 2mn/R_0(m^2+n^2\varepsilon^2)$. The helical field is proven to be a flux function, and its derivative with respect to the helical flux is labelled λ,

$$g = g(\chi), \tag{4.8a}$$

$$\lambda = \frac{\mathrm{d}g}{\mathrm{d}\chi}. \tag{4.8b}$$

Once the helical flux is known, the magnetic field can be promptly computed through:

$$B_r = \frac{1}{r}\frac{\partial \chi}{\partial u}, \tag{4.9a}$$

$$\nabla u \cdot \mathbf{B} = -\frac{1}{r}\frac{\partial \chi}{\partial r}, \tag{4.9b}$$

$$B_\vartheta = -\frac{m}{r} f \frac{\partial \chi}{\partial r} + \frac{n}{R_0} f g, \tag{4.9c}$$

$$B_\phi = \frac{n}{R_0} f \frac{\partial \chi}{\partial r} + \frac{m}{r} f g. \tag{4.9d}$$

It is also useful to introduce a normalized flux label ρ,

$$\rho = \frac{\chi - \chi_{\min}}{\chi_{\max} - \chi_{\min}}, \tag{4.10}$$

so that $\rho \in [0; 1]$.

4.2.1 Fourier-transformed equation

The helical Grad-Shafranov equation (4.7) is a second-order highly non-linear partial differential equation. The solution $\chi(r, u)$ can be decomposed similarly to eq. (4.2), so that each Fourier harmonic χ^q can be solved through a separate *ordinary* differential equation:

$$\frac{1}{f}\frac{\mathrm{d}}{\mathrm{d}r}\left(f\frac{\mathrm{d}\chi^q}{\mathrm{d}r}\right) + \frac{(iq)^2}{rf}\chi^q = \beta g^q - \left(g\frac{\mathrm{d}g}{\mathrm{d}\chi}\right)^q. \tag{4.11}$$

The biggest complexity in the HGS equation is the functional dependence of the helical field on the helical flux, $g = g(\chi)$. For this reason a technique that lets the helical field and the helical flux be computed separately, through an iterative two-step method, has been adopted. The iterative technique means that the right-hand side of the transformed equation (4.11) is considered as a known quantity during the integration, so that one has to solve a *linear* non-homogeneous differential equation in χ^q.

4.3 Solution

Due to the Fourier transform and the iterative technique, the HGS equation can be solved like an *ordinary* and *linear* differential equation. The solution, therefore, will be sum of two terms: the solution to the homogeneous equation, and a particular solution to the complete equation. Since the HGS eq. is a second-order differential equation, two integration constants will have to be enforced as boundary conditions. Schematically,

$$\chi^q = \chi^q_{\text{homog}}(C_1, C_2) + \chi^q_{\text{partic}}. \tag{4.12}$$

In order to be a physical flux the solution must satisfy a regularity constraint in the origin,

$$\chi^q(r) \to 0, \qquad \text{for } r \to 0. \tag{4.13}$$

Since both the homogeneous solution and the particular solution individually satisfy the regularity constraint, let us discuss about each of them separately.

4.3.1 Homogeneous solution

The homogeneous equation related to the HGS eq. is

$$\frac{1}{f}\frac{\mathrm{d}}{\mathrm{d}r}\left(f\frac{\mathrm{d}}{\mathrm{d}r}\chi^q_{\mathrm{homog}}\right)+\frac{(iq)^2}{rf}\chi^q_{\mathrm{homog}}=0. \tag{4.14}$$

Zeroth order

For $q=0$, eq. (4.14) is trivial and can be analytically integrated, but for $m\neq 0$ the solution is degenerate since the condition (4.13) enforces

$$\chi^{q=0}_{\mathrm{homog}}=0. \tag{4.15}$$

Higher orders

For $q\geq 1$, eq. (4.14) admits semi-analytical solutions in terms of the modified Bessel functions [Abr72], $I_{\pm\nu}(z)$ and $K_\nu(z)$, which are solutions to the equation

$$z^2\frac{\mathrm{d}^2w}{\mathrm{d}z^2}+z\frac{\mathrm{d}w}{\mathrm{d}z}-(z^2+\nu^2)w=0. \tag{4.16}$$

Considering that

$$\nu = q\,m, \tag{4.17a}$$
$$z = q\,n\,\varepsilon, \tag{4.17b}$$
$$w = \chi^q, \tag{4.17c}$$

the most general solution to eq. (4.14) can be found to be

$$\chi^{q\geq 1}_{\mathrm{homog}}(z)=C_1\,zI'_\nu(z)+C_2\,zK'_\nu(z). \tag{4.18}$$

The regularity constraint on the origin (4.13) enforces $C_2=0$. Moreover, exploiting the properties of the Bessel functions,

$$\chi^{q\geq 1}_{\mathrm{homog}}(z)=C_1\,zI'_\nu(z) \tag{4.19a}$$
$$=C_1(zI_{\nu+1}(z)+\nu I_\nu(z)). \tag{4.19b}$$

4.3.2 Inhomogeneous solution

The solution χ^q_{partic} to the inhomogeneous equation can be computed by numerical integration for each harmonic q.

The regularity constraint on the origin (4.13) can be enforced by appropriately building the solution during the numerical integration. By assuming a power dependence near the origin,

$$\chi^q_{\mathrm{partic}}(r)\sim A\,r^B, \qquad \text{for } r\to 0, \tag{4.20}$$

the regularity constraint can be discussed separately for the $q=0$ and the $q\geq 1$ harmonics. For simplicity, let

$$T^q=\beta g^q-(g\lambda)^q, \tag{4.21}$$

be the RHS known term in the helical Grad-Shafranov equation.

Zeroth order

For $q = 0$ the regularity constraint (4.13) on the A and B parameters enforces

$$A = \frac{1}{B^2} T^{q=0}(0), \tag{4.22a}$$

$$B = 2, \tag{4.22b}$$

and therefore

$$\chi^{q=0}_{\text{partic}}(r) \sim \frac{1}{4} T^{q=0}(0)\, r^2, \qquad \text{for } r \to 0. \tag{4.23}$$

Higher orders

For $q \geq 1$, on the other hand, the regularity constraint enforces only

$$B = qm, \tag{4.24}$$

with no condition on A, yielding

$$\chi^{q\geq 1}_{\text{partic}}(r) \sim A\, r^{qm}, \qquad \text{for } r \to 0. \tag{4.25}$$

4.3.3 Complete solution

In summary, the complete solutions to the HGS equation (4.11) are

$$\chi^{q=0} = \chi^{q=0}_{\text{partic}}, \tag{4.26a}$$

$$\chi^{q\geq 1}(C_1) = C_1 qn\varepsilon I'_{qm} + \chi^{q\geq 1}_{\text{partic}}. \tag{4.26b}$$

For $q \geq 1$, the C_1 integration coefficient can be exploited to impose a boundary condition. The boundary condition problem for RFX-mod is introduced in subsection 6.4.7.

CHAPTER 5

Solution technique

The aim of this chapter is to break down the solution technique and explain the idea behind it. The main complexities of the helical Grad-Shafranov equation will be discussed, and the proposed solution method will then be introduced.

5.1 Solution target

First, let us start by specifying the type of problem that will be tackled through the helical Grad-Shafranov equation. Two extremely different simulations will be introduced and discussed in Chapter 8, depending upon the topology.

5.1.1 SHAx and MHAx states

The main application of the Fortran code is the analysis of the dominant tearing mode in RFX-mod during a Quasi Single Helicity phase, which agrees profoundly with the basic assumptions of the helical Grad-Shafranov model. In RFP experiments with $|F| < 0.1$, in fact, the internally resonant $m = 1$, $n = 7$ tearing mode is found to routinely generate QSH states, during which it dominates the MHD perturbation spectrum, as plotted in figure 2.4b.

Depending on the amplitude of the dominant mode, different type of QSH states exist [Lor08]. Generally, QSH states exhibit a Multiple Helical Axis (MHAx) topology, where the geometric magnetic axis can be found together with the O- and X-points generated by the dominant island. However, when the amplitude of the dominant mode crosses the 3.5% threshold with respect to the total magnetic energy, the island grows and replaces the geometric magnetic axis, leaving the O-point as the Single Helical Axis (SHAx) of the configuration.

The main application of the HGS equation, discussed in section 8.1, involves a RFP configuration in a QSH phase, where the dominant $m = 1$, $n = 7$ tearing mode has sufficient amplitude so as to determine a SHAx state.

The second application, discussed in section 8.2, involves a MHAx state instead, produced by the $m = 2$, $n = 1$ tearing mode during a tokamak shot.

5.1.2 Radial domain

Let us also discuss the domain of the solution by specifying the range in the radial coordinate r, which is directly related the RFX-mod experimental setup explained in detail in section 2.3 and specifically in table 2.1.

Starting from the machine axis, $r = 0$, one first encounters the plasma region, $0 \leq r \leq a$. Then there is a region, $a < r < b$, which includes both the graphite wall and the vacuum vessel, at r_V, but that is modelled as 'vacuum'. Just before the conductive shell we find the magnetic sensors, at $r = r_{\mathrm{sens,r}}$ and $r = r_{\mathrm{sens,t}}$, and then the conductive shell at $r = b$. The radial domain is schematically plotted in figure 5.1.

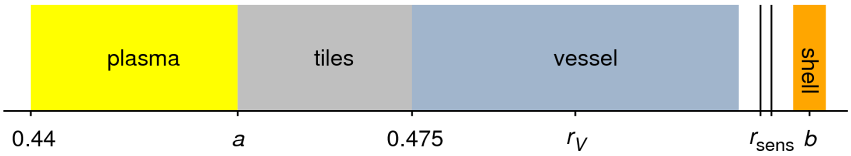

Figure 5.1: A schematic view of the main regions in the radial domain, to scale.

Summarizing, even though the solution can be interpreted up to the plasma radius, $0 \leq r \leq a$, the solution has to be computed up to the conductive shell, $0 \leq r < b$, since that is the position of the magnetic sensors exploited for the boundary conditions.

5.2 Solution scheme

As previously discussed, the iteration scheme adopted for the solution of the helical Grad-Shafranov equation helps in tackling the highly non-linear problem, by separating the left-hand from the right-hand side in eq. (4.11).

Initially a 'zeroth-step guess' for χ is computed, then the actual iterative cycle begins: the helical field g is computed exploiting the knowledge of χ, and then the helical flux χ is computed through equation (4.11) where g is a known quantity. Figure 5.2 visualizes the iterative cycle.

Each step exploits a helical field g that has been computed from the helical flux χ of the previous step, and provides χ for the computation of g in the successive step. The iteration continues until the required level of self-consistency is obtained, that is, when the helical field does not change anymore.

On one hand, such technique helps in circumventing the high non-linearity of the problem at the integration stage but, on the other hand, it shifts it towards the search for self-consistency, so that many iterations are actually needed.

Let us now look into the details of each stage.

5.3 Initial guess

In order to get a guess for the helical field g, so that it can be used as a known quantity in the HGS equation, a guess for χ has to be computed first. Dur-

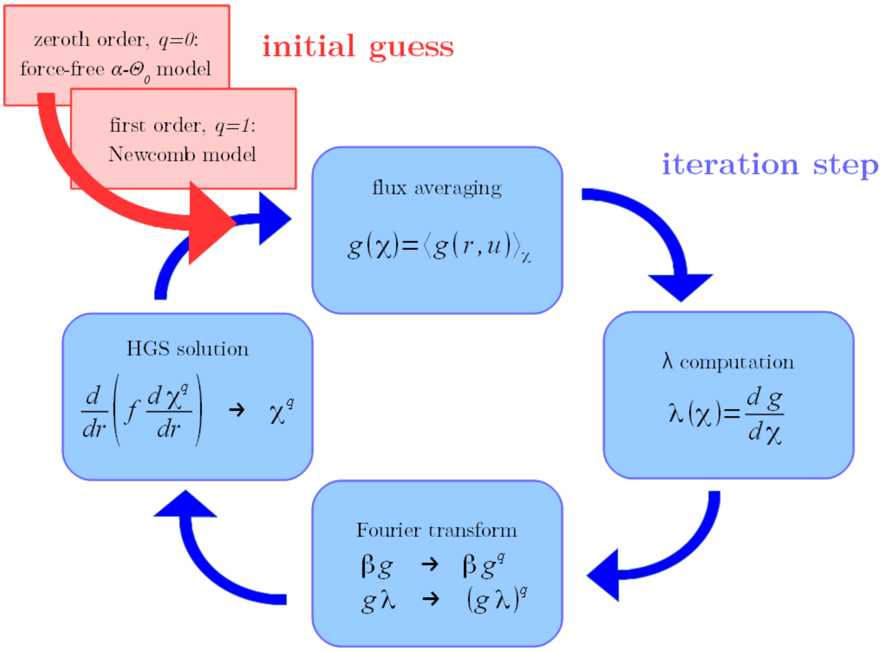

Figure 5.2: Flowchart of the solution algorithm.

ing such stage – labelled 'initial guess' or 'zeroth step' – both the zeroth-order harmonic $\chi^{q=0}$ and the first-order harmonic $\chi^{q=1}$ are computed.

For the zeroth order guess, $\chi^{q=0}$, we exploit an axisymmetric equilibrium based on the α-Θ_0 model [Ort93]. For the first order guess, $\chi^{q=1}$, we use a Newcomb approach [Fit99] based on the zeroth-order guess: the underlying α-Θ_0 equilibrium is perturbed and then a *linear* analysis is carried out. The Newcomb equation can be also obtained by a direct linearization of the HGS equation (4.7).

In the following of this section the magnetic field $\mathbf{B}$ will therefore consist of a zeroth-order magnetic field, $\mathbf{B}^{q=0} = \mathbf{B}_0$, and a first-order magnetic field, $\mathbf{B}^{q=1} = \mathbf{b}$.

5.3.1 Zeroth order

The underlying zeroth-order equilibrium is determined by the system

$$\nabla \cdot \mathbf{B}_0 = 0, \tag{5.1a}$$

$$\nabla \times \mathbf{B}_0 = \mu_0 \mathbf{J}_0, \tag{5.1b}$$

$$\mathbf{J}_0 \times \mathbf{B}_0 = \mathbf{0}. \tag{5.1c}$$

From the force-free equation immediately follows that the magnetic field and the current density are parallel,

$$\nabla \times \mathbf{B}_0 = \mu_0 \mathbf{J}_0 = \sigma \mathbf{B}_0, \tag{5.2}$$

or, more explicitly,

$$-\frac{\mathrm{d}}{\mathrm{d}r}B_{0\phi} = \sigma(r)\,B_{0\vartheta}, \tag{5.3a}$$

$$\frac{1}{r}\frac{\mathrm{d}}{\mathrm{d}r}(rB_{0\vartheta}) = \sigma(r)\,B_{0\phi}. \tag{5.3b}$$

The system of equations (5.3) has to be solved numerically.

The $\sigma(r)$ coefficient is modelled for RFPs through the α-Θ_0 approach [Ort93], and for tokamaks through the Wesson model [Wes04], which can be compactly written as

$$\sigma(r) = \left(\frac{2\Theta_0}{a}\right)\begin{cases}\left[1-\left(\frac{r}{a}\right)^{\alpha}\right] & \text{for RFPs,}\\ \left[1-\left(\frac{r}{a}\right)^{2}\right]^{\alpha} & \text{for tokamaks,}\end{cases} \tag{5.4}$$

with α and Θ_0 positive constants and where $\sigma(r) = 0$ for $r \geq a$.

For the RFP case in RFX-mod, the pulse file contains the information regarding the experimental F and Θ dimensionless parameters, introduced in eq. (2.1). The α and Θ_0 coefficients are determined through an automatic fit of the F and Θ parameters, where pressure is included, and are stored in the pulse file as well. Since we are neglecting pressure, the equilibrium computed exploiting such α-Θ_0 model does not exactly match the experimental F and Θ parameters.

For the tokamak case in RFX-mod, the α and Θ_0 coefficients are determined through an automatic fit of the $q(0)$ and $q(a)$ parameters, instead.

Furthermore, the plasma current I_P is read from the pulse file and exploited to scale the zeroth-order fields. The system (5.3), in fact, is linearly invariant so the scale factor has to be computed.

5.3.2 First order

Then, a linear perturbation theory is applied to the system (5.1), yielding for the first-order magnetic field $\mathbf{b}$

$$\nabla\cdot\mathbf{b} = 0, \tag{5.5a}$$

$$\nabla\times\mathbf{b} = \mu_0\mathbf{j}, \tag{5.5b}$$

$$\mathbf{J}_0\times\mathbf{b} + \mathbf{j}\times\mathbf{B}_0 = \mathbf{0}. \tag{5.5c}$$

The Newcomb equation for $\chi^{q=1}$ derives from (5.5) and can be written as

$$\frac{\mathrm{d}}{\mathrm{d}r}\left(f\frac{\mathrm{d}}{\mathrm{d}r}\chi^{q=1}\right) - g^{m,n}\chi^{q=1} = 0, \qquad \text{(NWC)} \tag{5.6}$$

where

$$F(r) = mB_{0\vartheta} - n\varepsilon B_{0\phi}, \tag{5.7a}$$

$$G(r) = n\varepsilon B_{0\vartheta} + mB_{0\phi}, \tag{5.7b}$$

$$g^{m,n}(r) = \frac{1}{r} + f\frac{G}{F}\frac{\mathrm{d}\sigma}{\mathrm{d}r} + f^2\frac{2mn\sigma}{rR_0} - f\sigma^2, \tag{5.8}$$

and where ε and f are defined in eq. (4.6) and σ in eq. (5.4).

The components of the perturbed magnetic field can be computed through

$$b_r = \frac{i}{r}\chi^{q=1}, \tag{5.9a}$$

$$b_\vartheta = \frac{-mf}{r}\frac{\mathrm{d}}{\mathrm{d}r}\chi^{q=1} + \frac{nf}{R_0}\sigma\chi^{q=1}, \tag{5.9b}$$

$$b_\phi = \frac{nf}{R_0}\frac{\mathrm{d}}{\mathrm{d}r}\chi^{q=1} + \frac{mf}{r}\sigma\chi^{q=1}. \tag{5.9c}$$

The Newcomb equation, and in particular the term $1/F$, is singular at the surface where the input m, n mode resonates with the cylindrical safety factor, as in eq. (2.4), and generally exhibits a discontinuity in its first derivative at $r = r_s$, while still remaining continuous. From a mathematical point of view, therefore, the solution is computed separately in the inner region, $0 \le r < r_s$, and the outer region, $r_s < r < b$, while the resonant region, $r_s^- \le r \le r_s^+$, is investigated by Taylor-expanding the F term.

Since the Newcomb equation is a second-order differential equation, two integration constants have to be specified, but due to the domain interruption at the resonant surface *four* integration constants have to be specified instead, two for each region. The regularity condition in the origin (4.13) has to be enforced together with the continuity condition through r_s: each condition exploits an integration constant. The remaining two integration constants are exploited to enforce $b_r^{m,n}(r_{\mathrm{sens}})$ and $b_\phi^{m,n}(r_{\mathrm{sens}})$, which are the Fourier-transformed boundary values for the first-order magnetic field, computed as explained in subsection 2.3.1.

As the zeroth- and first-order solutions are known, the helical flux χ can be directly computed through

$$\chi = \chi^{q=0} + \chi^{q=1}e^{iu} + c.c., \tag{5.10}$$

and then the magnetic field $\mathbf{B}$ follows from eq. (5.9). After that, the helical Grad-Shafranov iterative procedure can start.

5.4 Iteration step

5.4.1 Flux averaging

The first problem is that, in general, the helical field is not a flux function, but it has to be for the helical Grad-Shafranov equation to stand. Therefore, a flux averaging of the helical field has to be carried out,

$$g(r,u) \longmapsto g(\chi) = \langle g(r,u)\rangle \tag{5.11a}$$

$$= \langle mB_\phi(r,u) + n\varepsilon(r)B_\vartheta(r,u)\rangle \tag{5.11b}$$

$$= m\langle B_\phi\rangle + n/R_0\langle rB_\vartheta\rangle. \tag{5.11c}$$

The flux surface average is defined by

$$\langle Q\rangle = \frac{\mathrm{d}}{\mathrm{d}V}\int_V Q\,\mathrm{d}^3x, \tag{5.12}$$

where V is the volume within the flux surface and $\mathbf{x} \equiv (r, \vartheta, \phi)$. By introducing a simple u-average at constant χ,

$$\langle Q \rangle_0 = \frac{1}{2\pi} \int_0^{2\pi} Q \,\mathrm{d}u, \tag{5.13}$$

the flux average (5.12), following Finn's paper, takes the form

$$\langle Q \rangle = \langle QJ \rangle_0 / \langle J \rangle_0, \tag{5.14}$$

where J is the Jacobian,

$$J^{-1} = n/R_0 \,\mathbf{B} \cdot \nabla u. \tag{5.15}$$

The flux average at constant χ therefore results

$$\langle Q \rangle = \frac{\oint Q \,(\mathbf{B} \cdot \nabla u)^{-1} \,\mathrm{d}u}{\oint (\mathbf{B} \cdot \nabla u)^{-1} \,\mathrm{d}u}, \tag{5.16}$$

where, more explictly,

$$\int_0^{2\pi} (\mathbf{B} \cdot \nabla u)^{-1} \,\mathrm{d}u = \int_0^{2\pi} \frac{\sqrt{\mathrm{d}r^2 + rf\,\mathrm{d}u^2}}{\sqrt{(b^r)^2 + f/r(\mathrm{d}\chi/\mathrm{d}r)^2}}. \tag{5.17}$$

5.4.2 λ derivation

Since the right-hand side of the HGS equation involves g as well as its derivative with respect to χ, $\lambda = \mathrm{d}g/\mathrm{d}\chi$, a derivation is necessary. At this stage a branching occurs, depending upon the topology of the configuration. As explained in section 5.1, in fact, the computation for a MHAx configuration is radically different than that of a SHAx configuration.

In a SHAx case the helical field g is a single-valued function of the helical flux χ: the derivation of λ is straightforward.

In a MHAx case, on the other hand, g is a multi-valued function of χ, since there are different contours with the same χ label, and the derivation has to be computed for each branch separately. As a consequence, two contours with equal χ do not, in general, have equal λ.

5.4.3 Fourier transform

Then, g and λ have to be expressed back in terms of (r, u),

$$g(\chi) \longmapsto g(r, u) = g(\chi(r, u)), \tag{5.18a}$$

$$\lambda(\chi) \longmapsto \lambda(r, u) = \lambda(\chi(r, u)), \tag{5.18b}$$

in order to be successfully Fourier transformed,

$$g(r, u) \longmapsto g^q(r), \tag{5.19a}$$

$$g(r, u)\lambda(r, u) \longmapsto (g\lambda)^q(r). \tag{5.19b}$$

As soon as g and $g\lambda$ are Fourier transformed, the right-hand side of eq. (4.11) is fully known. The HGS solution can then be tackled.

5.4.4 HGS solution

Both the homogeneous and the inhomogeneous solutions of the helical Grad-Shafranov equation are computed numerically, as discussed in section 4.3.

Zeroth order

For $q = 0$, the solution (4.26a) coincides with the particular solution, without exploitable integration constants.

Higher orders

For $q \geq 1$, the solution (4.26b) is a superposition of the homogeneous and particular solutions, and the C_1 integration constant can be exploited to enforce a boundary condition. The boundary condition problem for RFX-mod is discussed in subsection 6.4.7.

5.4.5 Inverse Fourier transform

Similarly to eq. (5.10), the full χ solution can be computed through

$$\chi = \sum_q \chi^q e^{iqu} + c.c., \tag{5.20}$$

and the magnetic field can be computed from eq. (4.9), completing the iteration step. The procedure can then loop back to section 5.4 with a new estimate for the helical flux χ and for the magnetic field $\mathbf{B}$.

The helical field $g(r, u)$ at this stage is *not* changed with respect to eq. (5.18): it will be replaced only after the flux averaging (5.11) made on the new flux surfaces in the successive iteration step.

CHAPTER 6

Fortran implementation

This chapter deals with the development of the `hegrasha` Fortran code, which iteratively solves the helical Grad-Shafranov equation for the RFX-mod experiment. The outline of the chapter closely follows the flow of the code itself.

6.1 Motivation

Since a general analytical solution is not possible for the helical Grad-Shafranov equation, a program has been written in order to compute the solution by means of numerical integration of the Fourier-transformed equation.

The program – named `hegrasha` for 'helical Grad-Shafranov code' – has been written in Fortran, closely coupled to the cylindrical Newcomb code `newcomb_cyl`, developed as part of the author's Master's thesis [Tre10].

As discussed in section 5.1, `hegrasha` can be applied to both SHAx and MHAx states. Since this chapter is devoted to the explanation of each computation performed by the code, the main results are reported for both topological configurations.

6.2 Initialization

6.2.1 Dependencies

Fortran has been chosen as programming language because of its nature of heavy computational solver.

The code, at present, relies on two dependencies: the Fortan NAG libraries are exploited for various internal computations, and the IDL `CONTOUR` procedure is used as an external flux surface solver.

Furthermore, `hegrasha` has been partially parallelized following the OpenMP paradigm. The parallelization contributes in shortening the runtimes of the most intense computational portions of the code.

6.2.2 Parameters

First of all, let us introduce a few among the parameters that will be exploited throughout the program. This helps the reader get in touch with the requirements and the internal structure of the code.

The external parameters required by the code as input are straightforward and self-explanatory:

- shot number (e.g. #23810);
- time instant (e.g. 80 ms);
- poloidal mode number m (e.g. 1);
- toroidal mode number n (e.g. 7).

The internal parameters carry information about the behaviour of the code:

- number of harmonics to be considered (e.g. 2);
- tolerance of the numerical integrations (e.g. 10^{-12});
- number of contours for flux averaging (e.g. 300);
- boundary condition to be imposed (e.g. b_r);
- additional boundary condition, if any, to be used (e.g. none);
- back-averaging constant (e.g. 88%);
- convergence threshold (e.g. 10^{-2});
- converging iterations required (e.g. 20).

Each variable could be targeted by a full analysis in its own right, but only a few have been subjected to such scrutiny. The other have been chosen and tweaked by trial-and-error in order to accomodate both reasonable computational accuracy and runtime.

6.2.3 Data acquisition

The first thing `hegrasha` needs to do is acquire from the database the information corresponding to the shot number, time instant and mode given as input. The following data are read from consecutive queries to MDS trees:

- zeroth-order F and Θ parameters;
- force-free α and Θ_0 parameters;
- plasma current I_P;
- first-order boundary conditions $b_r^{m,n}$ and $b_\phi^{m,n}$.

As explained in subsection 5.3.1, α and Θ_0 are read to compute the force-free equilibrium model from eq. (5.4). However, they do not lead to the same F and Θ parameters which they have been derived from, due to the role of pressure. The experimental F and Θ parameters are in fact retrieved from the pulse file as comparison quantities only.

The plasma current I_P is exploited to enforce the scale of system (5.3), and the first-order boundary conditions are used in the construction of the first-order helical Grad-Shafranov solution.

6.3 Initial guess

The numerical portion of the code begins with the separate computation of the zeroth- and first-order initial guesses, following section 5.3, through the `nag_ivp_ode_rk` NAG library for Runge-Kutta numerical integration.

The results are plotted for both a RFP shot with a dominant $m = 1$, $n = 7$ tearing mode in a SHAx state, labelled 'RFP/1,7/SHAx' for brevity, and for a tokamak shot with a $m = 2$, $n = 1$ tearing mode in a MHAx state, labelled 'tok/2,1/MHAx'.

6.3.1 Zeroth order

The zeroth-order equilibrium, computed following subsection 5.3.1, is plotted in figure 6.1.

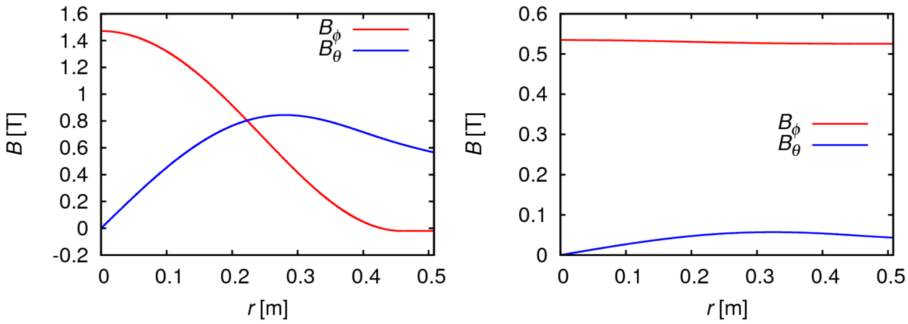

Figure 6.1: The two components, $B_\vartheta^{q=0}$ and $B_\phi^{q=0}$, of the initial guess are plotted for the RFP/1,7/SHAx run (left panel) and the tok/2,1/MHAx run (right panel).

6.3.2 First order

The first-order Newcomb perturbation, computed following subsection 5.3.2 with dominant mode $m = 1$, $n = 7$ for the RFP shot and $m = 2$, $n = 1$ for the tokamak shot, is plotted in figure 6.2.

6.4 Iterative loop

The main loop of the program can then be entered, that is, the portion devoted to the actual solution of the helical Grad-Shafranov equation. Following the idea discussed in section 5.4, a few computations have to be carried out before the numerical solver can integrate the differential equation.

6.4.1 Contour analysis

As previously anticipated, for the contour analysis `hegrasha` currently relies on the external `CONTOUR` IDL procedure, which identifies each contour and returns the (r, u) data points so as to carry out further computations.

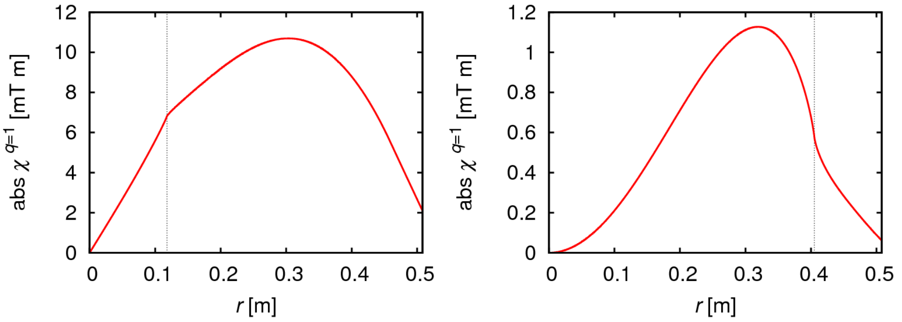

Figure 6.2: The first-order Newcomb solution, $\chi^{q=1}$, is plotted for the RFP/1,7/SHAx run (left panel) and the tok/2,1/MHAx run (right panel). In both panels, the dashed vertical line shows the resonant surface for the $q = 1$ mode.

The definition of a contour is that of a collection of *connected* points characterized by the same χ value. While for a SHAx state the definition is straightforward, for a MHAx case it is less evident. It is therefore important to note that a certain value of χ corresponds, in general, to more than one contour.

An example of the typical result of the contour analysis is plotted in the (r, ϑ) plane in figure 6.3 for both the RFP/1,7/SHAx run and the tok/2,1/MHAx run.

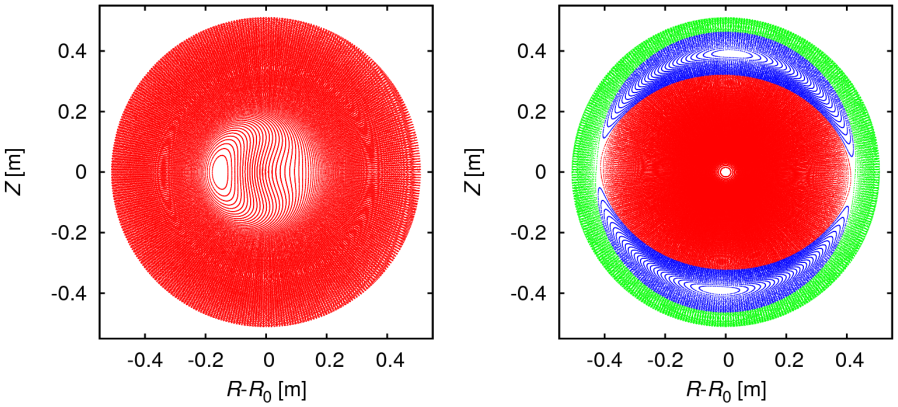

Figure 6.3: The typical result for the contour analysis is plotted for both the RFP/1,7/SHAx run (left panel) and the tok/2,1/MHAx run (right panel).

The different colours in the right panel of figure 6.3 are due to the further topological analysis carried out by `hegrasha` which is explained in subsection 6.4.3.

6.4.2 Flux averaging

In order to get the helical field as a flux quantity $g(\chi)$ rather than a polar quantity $g(r, u)$, a flux averaging procedure is carried out following subsection 5.4.1.

The result is a discrete flux function, plotted in figure 6.4 as a function of the normalized flux ρ defined in eq. (4.10).

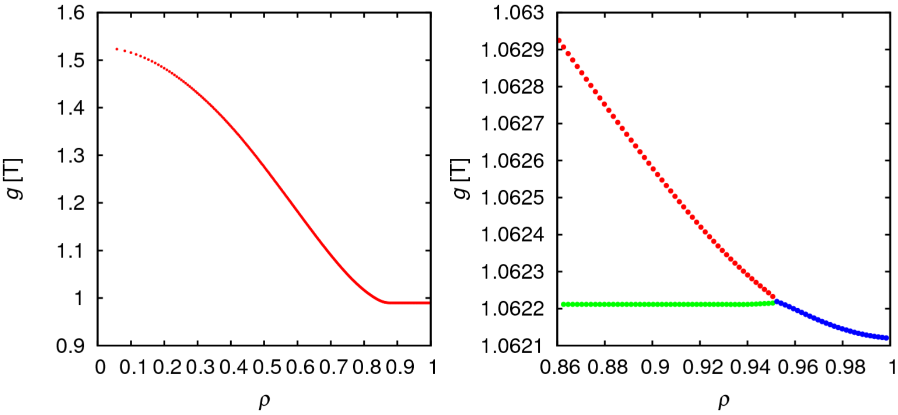

Figure 6.4: The flux-averaged helical field $g(\chi)$ as a function of the normalized poloidal flux ρ for both the RFP/1,7/SHAx run (left panel) and the tok/2,1/MHAx run (right panel). Note that, for the tok/2,1/MHAx run, the plotted range is the edge region, so as to highlight the multi-valued functional dependence.

6.4.3 λ derivation

Then, as explained in subsection 5.4.2, the derivative of the helical field g with respect to the helical flux, $\mathrm{d}g/\mathrm{d}\chi$, has to be computed.

In the MHAx state a topological analysis has to be computed before λ can be derived, since each region has to be considered separately. The contour analysis produces the colored contour sets plotted in figure 6.3.

The derivation can then be performed, as plotted in figure 6.5.

6.4.4 Grid computation

The quantities g and $g\lambda$, computed in the previous steps and expressed back in terms of (r, u) following eq. (5.18), have then to be Fourier transformed.

Unfortunately, they are *not* evenly spaced in a polar grid as necessary. Therefore, the information scattered on the polar plane has to be distributed on a grid regular in u (and regular in ϑ for constant ϕ), which is also regular in r for simplicity. In order to do this, the NAG library `nag_scat_interp` for scattered bidimensional data is exploited. This lets most of the information to be reliably evaluated on regular grid positions, even though a certain amount of care has to be put into a verification process, since often the NAG library badly evaluates data where there are too many (or too little) points.

A ‘healing’ procedure has then been devised, that ‘heals’ the badly evaluated points and replaces them with a much more reliable one-dimensional interpolation on the diameter, carried out through the `nag_spline_1d` spline interpolation library.

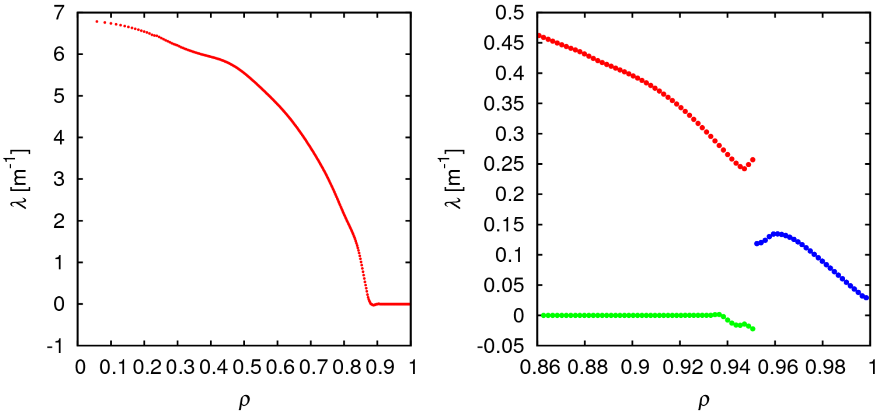

Figure 6.5: The two typical $\lambda(\chi)$ profiles as a function of the normalized poloidal flux ρ for both the RFP/1,7/SHAx run (left panel) and the tok/2,1/MHAx run (right panel). Note that, for the tok/2,1/MHAx run, the range is the edge region corresponding to the left panel of figure 6.4.

6.4.5 Fourier transform

After that, the `nag_fft` library carries out the actual Fourier decomposition of both g and $g\lambda$, as in eq. 5.19. In order to account for the vacuum region the Fourier harmonics are modified and $\lambda = 0$ is enforced for $r > a$.

6.4.6 HGS solution

Then, everything is ready for the actual computation of the HGS equation (4.11). Since the helical Grad-Shafranov equation is non-homogeneous, both the analytical homogeneous solution and the numerical inhomogeneous solution have to be computed, as explained in section 4.3. The former currently relies on the `nag_bessel_fun` NAG library for the construction of the Bessel functions, while the latter is computed through the `nag_ivp_ode_rk` NAG library for Runge-Kutta numerical integration.

6.4.7 Boundary conditions

As discussed in section 4.3, the harmonics present different characteristics with respect to the integration constant. Let us discuss each of them separately.

Zeroth order

The $q = 0$ solution (4.26a) does not depend upon the C_1 integration constant, and no boundary condition is enforced.

First order

The $q = 1$ solution (4.26b) does present the C_1 constant, so that one boundary condition can be enforced.

For the specific case of RFX-mod, two available measurements of the $q = 1$ perturbation are available as boundary conditions: $b_r^{m,n}(r_{\text{sens}})$ and $b_\phi^{m,n}(r_{\text{sens}})$, computed as explained in subsection 2.3.1. Since just one parameter is available as boundary condition, we cannot exploit both measurements. The radial component is typically used,

$$b_r^{q=1}(r_{\text{sens}}) = b_r^{m,n}(r_{\text{sens}}), \tag{6.1}$$

leaving the toroidal component as a comparison quantity in order to verify the quality of the convergence.

The overdetermined problem for the boundary conditions is further discussed, from a numerical point of view, in section 7.3.

Higher orders

The $q \geq 2$ solutions (4.26b) present the C_1 constant as well.

Similarly to the $q = 1$ solution, the radial component of the perturbation magnetic field is chosen as boundary condition, but it is enforced to zero rather than to a finite value,

$$b_r^{q\geq 2}(r_{\text{sens}}) = 0. \tag{6.2}$$

The main reason for the condition (6.2) on higher harmonics is that due to the low poloidal periodicity of the magnetic sensors in RFX-mod, which is $M = 4$ as described in section 2.3, it is not possible to detect and measure $q \geq 2$ harmonics. For $m = 1$, for example, aliasing problems prevent from separating the $q = 2$ harmonic from the error field contributions to the $q = -2$ harmonic.

The constraint (6.2) is a reasonable approximation, moreover, since the magnetic sensors are on the inner surface of the conductive shell, which is subject to image currents that act against any magnetic field. In the presence of feedback the shell can be considered almost ideal so that it neutralizes their radial magnetic field. Since their amplitude is zero on the shell, at $r = b$, it will be negligible near it, at $r = r_{\text{sens}}$: the resulting equation (6.2) is therefore labelled ‘ideal shell’ condition.

6.4.8 Back-averaging

Once the solutions χ^q for the specified q harmonics have been computed, in accordance with the external magnetic measurements whenever available, the program can loop back to the contour analysis of subsection 6.4.1. In the new iteration step, the χ solution reconstructed from eq. (5.20) and the magnetic field from eq. (4.9) can be exploited to compute a new guess for the right-hand side of the HGS equation (4.11).

The problem is that, in general, the convergence of such an iterative procedure proves to be rather delicate and extremely sensitive to numerical errors, prompting the implementation of a back-averaging technique. The theory of the back-averaging mechanism is discussed in detail in the 1988 paper by Kress [Kre88].

A back-averaging method can be defined as a numerical technique for calculating the fixed point of a transformation, that can yield convergence where it does not exist and accelerate it when it does. Even though many kinds of back-averaging mechanisms can be introduced, a simple (or two-point) back-averaging has been implemented in the Fortran code. The goal of making the iterating procedure more robust with respect to convergence problems has been met, as is discussed in section 7.5, nonetheless more refined back-averaging implementations could further improve the results.

The implemented back-averaging paradigm follows the two-point approach:

$$\chi_{(i+1)} = (1 - K)\,\chi_{(i)} + K\,\chi_{(i-1)}, \tag{6.3}$$

where K is the back-averaging constant, and $\chi_{(i)}$ indicates the i-th step solution. A K constant of 0% means there is no averaging, and the iterating procedure works as outlined in the opening of this subsection. On the other hand, a constant of 100% means that there is no iterating, since new information is always discarded[1]. The back-averaging technique is applied to both the helical flux $\chi_{(i)}$ and the magnetic field $\mathbf{B}_{(i)}$, with typical values for K as high as 90%.

6.4.9 Convergence criterion

Let z_1 and z_2 be two complex r-functions, $z_{1,2}(r) \in \mathbb{C}$. Then, the δ convergence factor computed from

$$\delta(z_1, z_2) = \left(\frac{\displaystyle\int \mathrm{d}r\, |z_1(r) - z_2(r)|^2}{\displaystyle\int \mathrm{d}r\, |z_1(r)|^2} \right)^{1/2}, \tag{6.4}$$

represents an extremely helpful measure of the agreement between z_1 and z_2. Eq. (6.4) can be further specified so as to compare successive HGS solutions, that is, $z_1 = \chi^q_{(i)}$ and $z_2 = \chi^q_{(i-1)}$, as in

$$\delta^q(i) = \delta(\chi^q_{(i)}, \chi^q_{(i-1)}). \tag{6.5}$$

Indeed, the two most valuable variables to estimate the quality of a simulation are the zeroth-order convergence factor, $\delta^{q=0}$, and the first-order factor, $\delta^{q=1}$.

The latter is the convergence factor against which the convergence criterion is checked: the user can specify how many iterations must have a $\delta^{q=1}$ lower than a certain threshold before the iteration is considered 'converged'. A reasonable setup for the convergence criterion could be 20 iterations with $\delta^{q=1} < 0.5\%$.

In most analyses, however, and in particular in the simulations on which chapter 7 is based, the convergence criterion has not been explicitly used so as to gain information about how the iterations behave *after* convergence. This is a necessary step in the validation of a code.

Anyway, once the convergence criterion is found not to be satisfied, `hegrasha` loops back to the beginning, that is, to subsection 6.4.1.

---

[1] A negative K constant would fall under the forward-averaging approach, which will not be considered here.

CHAPTER 7

Convergence

In order to better understand the inner workings of the Fortran code and of the helical Grad-Shafranov equation, some analyses have been carried out targeting the most important internal parameters. The insight gained through such approach has been used to improve the code itself, and to tailor it to specific requirements. Each and every one of these analyses, focusing on the $m = 1$, $n = 7$ mode in a SHAx state during a RFP shot in RFX-mod, helped in getting the converged results that will be presented and discussed in the next chapter, in section 8.1.

parameter	*value*	*description*	*section*
`maxq`	`1÷4`	number of harmonics	7.1
`nlev`	`200,300,400`	number of contours	7.2
`bc`	`0÷3`	main BC	7.3
`addbc`	`no,nwc,hgs`	additional BC	7.4
`bacav`	`84÷90%`	back-averaging constant	7.5

Table 7.1: The main analysed parameters with the corresponding section.

For each analysis a few aspects have been investigated: the overall convergence paths on one hand, and the final reconstruction results on the other hand. It is worth stressing that the simulations were launched so as to run for 200 iterations, with or without convergence. If the convergence algorithm introduced in subsection 6.4.9 was switched on, it would stop the quickest ones after a few tens of iterations, and would keep the slowest ones running for much longer than 200 steps.

7.1 Number of harmonics

This section will focus on `maxq`, the parameter controlling the maximum number of harmonics to consider in the computation of the Fourier-transformed helical Grad-Shafranov equation (4.11). The purpose is to understand how much the addition of harmonics influences the final result since, clearly, a certain cutoff to the harmonic spectrum has to be imposed.

7.1.1 Parameters

The analysis is carried out by varying the number of harmonics included in the computation, $q = 0, \ldots, \max_q$, with cutoff `maxq=1÷4`. The main parameters of the analysis are reported in table 7.2.

parameter	*value*	*description*	*section*
`maxq`	1÷4	number of harmonics	7.1
`nlev`	300	number of contours	7.2
`bc`	0	main BC	7.3
`addbc`	`no`	additional BC	7.4
`bacav`	88%	back-averaging constant	7.5

Table 7.2: Summary of the main parameters of the simulations.

7.1.2 Convergence

First of all, let us take a look at the convergence of each simulation. Figure 7.1 shows the path for the most important variables: F and $\delta^{q=0}$, which are based on the zeroth-order fields, and $\max \operatorname{abs} \chi^{q=1}$ and $\delta^{q=1}$, which are first-order quantities.

The first thing that can be noticed is that, for the `maxq=1` simulation, the maximum of the first-order solution steadily lowers iteration after iteration, despite a low first-order convergence factor. Such behaviour – which could be termed *local* convergence as opposed to *global* convergence – is not found for the zeroth-order F parameter, and could not be understood by looking at either $\delta^{q=0}$ and $\delta^{q=1}$: the zeroth- and first-order convergence factors, in fact, detect minor differences between successive iterations, on average below 0.1%. The simulation evolves nonetheless, and the minor differences sum up leading to a final maximum value which is approximately 13% lower than that of the other simulations. A reason for this could be that the second harmonic, $q = 2$, is needed for the model to be stable and self-consistent.

The other simulations, `maxq=2÷4`, behave as expected and low convergence factors correspond to low differences between the solutions.

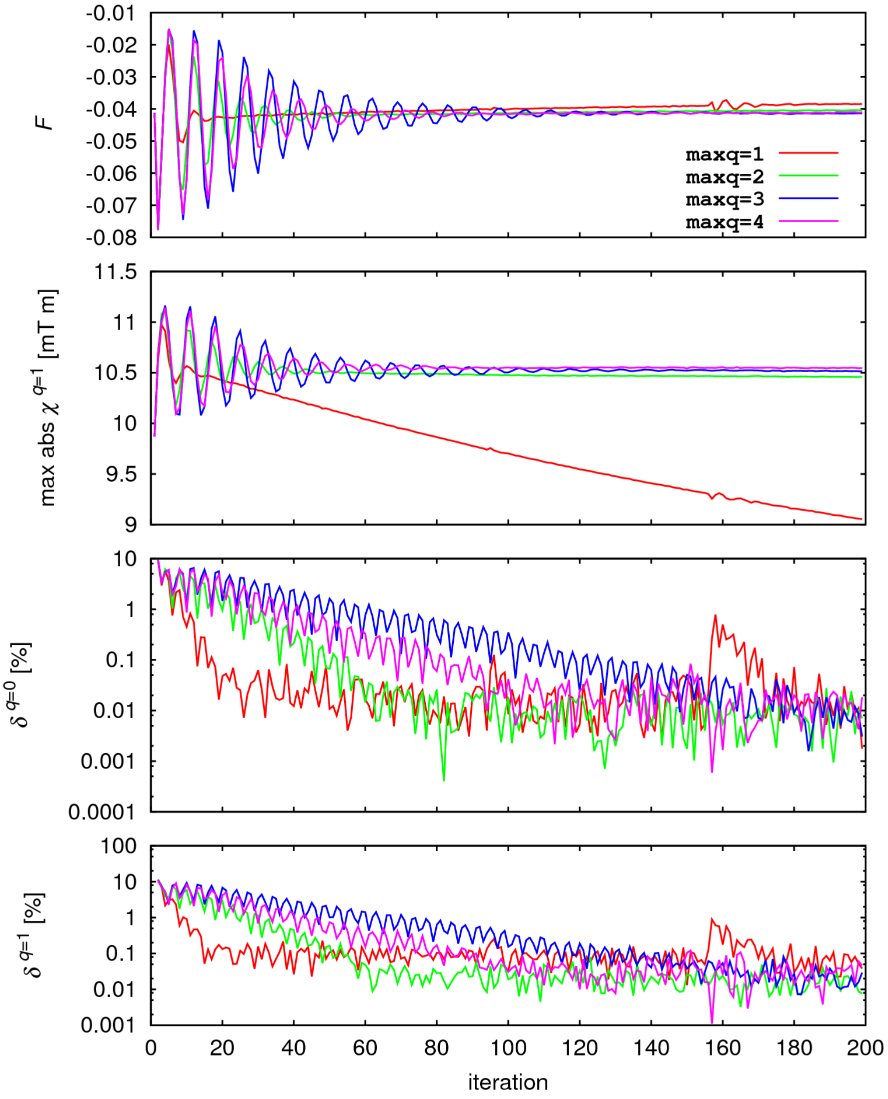

Figure 7.1: Converge paths of F, $\max\text{abs}\,\chi^{q=1}$ and $\delta^{q=0,1}$ for `maxq=1÷4`.

7.1.3 Solutions

Then, let us focus on the reconstructed solutions. Figure 7.2 shows the $q = 0 \div 3$ profiles for each reconstruction.

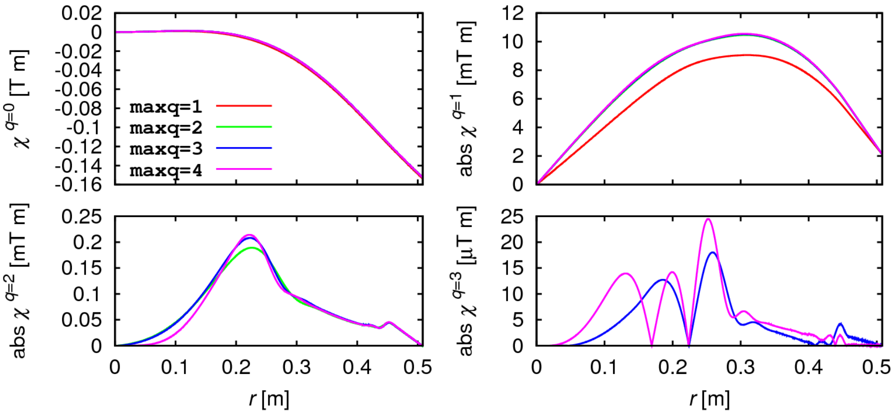

Figure 7.2: Profiles of the computed $q = 0 \div 3$ solutions for `maxq=1÷4`.

The `maxq=1` simulation (plotted for comparison) suffers from a lack of global convergence, as previously explained, and should therefore be left out of any further consideration.

The `maxq=2÷4` simulations show a definite agreement between themselves indicating that, from the `maxq=2` simulation up, the final result does not depend upon the `maxq` parameter. In other terms, further information is exploited to compute higher harmonics, but does not influence the lower $q = 0, 1$ harmonics and has little effect on the $q = 2$ harmonic.

7.1.4 Conclusions

Summarizing, the `maxq=2` simulation has sufficient information for the algorithm to be both physically self-consistent and numerically stable.

(page intentionally left blank)

7.2 Number of contours

Another extremely important parameter in each simulation is the number of contours exploited for the contour analysis. Due to the very sensitive computations needed by the preliminary steps of the helical Grad-Shafranov equation, too little information can be detrimental. For such reason, a few contour configurations have been analysed so as to determine the best setup.

7.2.1 Parameters

Simulations with a uniform contour density and different number of contours have been launched. The main parameters are reported in table 7.3.

parameter	*value*	*description*	*section*
`maxq`	2	number of harmonics	7.1
`nlev`	`200,300,400`	number of contours	7.2
`bc`	0	main BC	7.3
`addbc`	`no`	additional BC	7.4
`bacav`	88%	back-averaging constant	7.5

Table 7.3: Summary of the main parameters of the simulations.

7.2.2 Convergence

Once again, let us first take a look at the convergence paths in figure 7.4.

The `nlev=200` simulation has managed to complete the whole iteration cycle, but has not reached convergence. This indicates that too little contour information may be detrimental for the convergence, and indeed numerical instabilities may occur with `nlev<200`. On the other hand, the `nlev=300,400` simulations have reached convergence.

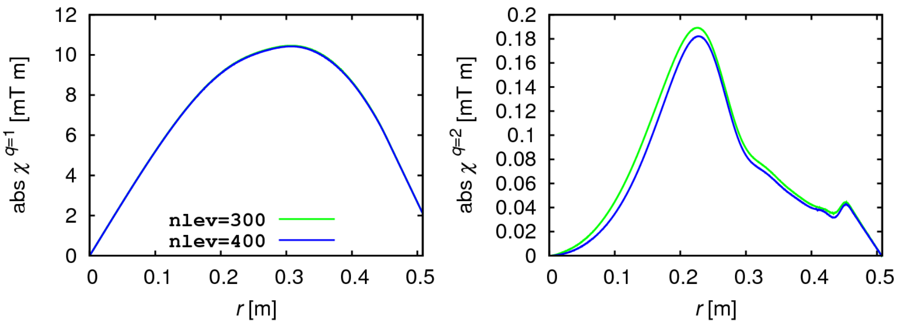

Figure 7.3: Profiles of the computed $q = 1 \div 2$ solutions for `nlev=300,400`.

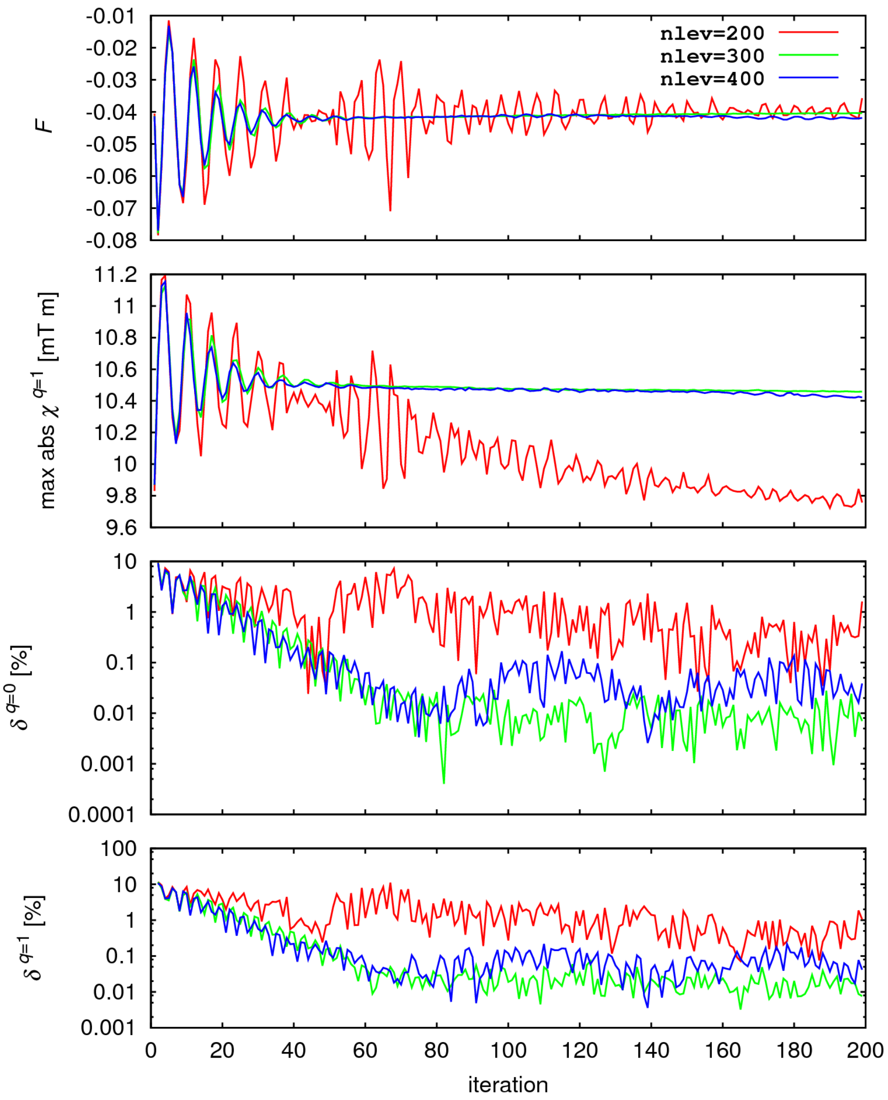

Figure 7.4: Converge paths of F, $\max\text{abs}\,\chi^{q=1}$ and $\delta^{q=0,1}$ for `nlev=200,300,400`.

7.2.3 Solutions

The reconstructed solutions for the converged simulations `nlev=300,400`, plotted in figure 7.3, show an excellent agreement up to the second-order harmonic.

7.2.4 Conclusions

In summary, the contour setup requires sufficient density in the central and near-axis region for numerical precision and computation stability. Among the proposed densities, the `nlev=300` shows the best convergence properties.

7.3 Main boundary condition

As introduced in subsection 2.3.1 and discussed in subsection 6.4.7 for the specific case of RFX-mod, the experimentally measured radial component of the perturbation magnetic field is typically exploited as a boundary condition, leaving the toroidal component as a comparison quantity in order to verify the quality of the convergence. The aim of this section is to investigate whether exploiting the other boundary condition modifies the result or not, and what happens if both are used at the same time during the simulation.

7.3.1 Parameters

Five simulations have been launched enforcing the toroidal condition every `bc=0÷3` iterations. With such definition, `bc=0` means that $b_r^{m,n}$ is used, `bc=1` means that $b_\phi^{m,n}$ is used, and `bc=2÷3` means that $b_r^{m,n}$ is used for `bc-1` steps, and then $b_\phi^{m,n}$ is used for the successive step. The main parameters of the analysis are reported in table 7.4.

parameter	*value*	*description*	*section*
`maxq`	2	number of harmonics	7.1
`nlev`	300	number of contours	7.2
`bc`	0÷3	main BC	7.3
`addbc`	`no`	additional BC	7.4
`bacav`	88%	back-averaging constant	7.5

Table 7.4: Summary of the main parameters of the simulations.

7.3.2 Convergence

First, let us focus on the convergence paths, shown in figure 7.5.

The first thing one notices from figure 7.5 is that the `bc=1` simulation does not reach convergence and fatally terminates after 130 iterations. Moreover, the `bc=2` simulation, which is obtained by alternatively enforcing both $b_r^{m,n}$ and $b_\phi^{m,n}$, reaches a quasi-steady state characterized by a fading $\max \text{abs}\, \chi^{q=1}$ and zeroth- and first-order deltas much higher than those of the `bc=0` simulation. Such effect can be linked with the fact that two successive steps exploit two different and *independent* boundary conditions, so that the solution cannot satisfy both. The `bc=3` simulation exhibits a similar behaviour but with a few quantitative differences, e.g. the $\max \text{abs}\, \chi^{q=1}$ changes slower and, since the boundary condition changes every two steps, there is a subset of iterations where the first-order convergence factor is as low as 0.1%, corresponding to the iterations where the boundary condition does not change. The `bc=0` simulation is the one with the best convergence features.

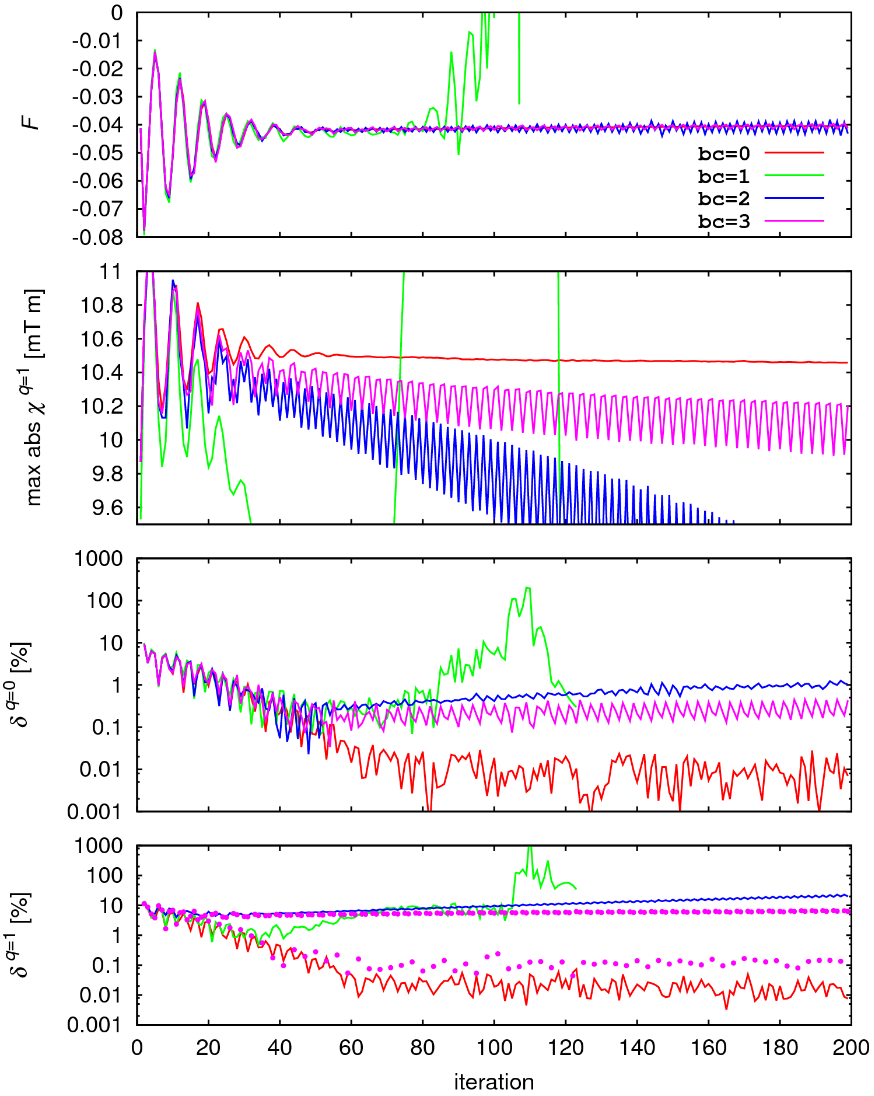

Figure 7.5: Converge paths of F, $\max \mathrm{abs}\, \chi^{q=1}$ and $\delta^{q=0,1}$ for `bc=0÷3`.

7.3.3 Edge toroidal field

Apart from the quantities plotted in figure 7.5, it is interesting to focus on the toroidal component of the perturbed magnetic field at the sensors' radius, $\mathrm{abs}\, b_\phi^{q=1}(r_\mathrm{sens})$, as shown in figure 7.6.

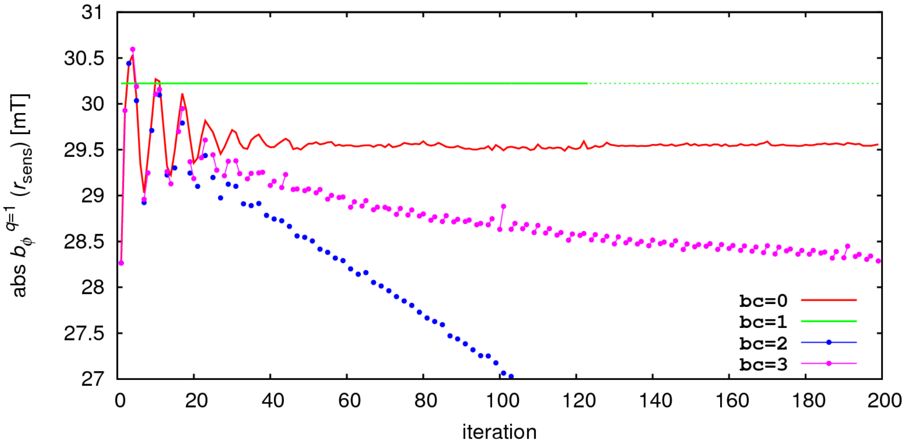

Figure 7.6: Converge paths of $\mathrm{abs}\, b_\phi^{q=1}(r_\mathrm{sens})$ for `bc=0÷3`.

For simplicity, the points where the boundary condition has been enforced through $b_\phi^{m,n}$ have been removed from the plot, but the `bc=1` simulation has been plotted untouched in order to show the measured value. In such way, for the `bc=2` simulation only half of the points have been plotted, whereas for the `bc=3` simulation two thirds have. As is evident from figure 7.6, the `bc=2` simulation does not converge towards the measured toroidal value, even if such value is imposed every other iteration. Similarly, the `bc=3` simulation is characterised by a much slower change, but the toroidal field still does not converge. On the other hand, the `bc=0` simulation converges to a well-defined value, which differs from the experimental value. This discrepancy will be further discussed in section 7.4.

7.3.4 Solutions

Since only the `bc=0` solution has reached true convergence, no comparison can be done with the `bc=2,3` simulations.

7.3.5 Conclusions

In summary, exploiting simultaneously two different boundary conditions compromises the stability of the solution. Considering that the simulations with both boundary conditions fail to converge and therefore do not yield a reasonable solution, the choice of radial boundary condition remains the most convenient one.

7.4 Additional boundary condition

The problem of overdetermined boundary conditions has been partially discussed in the previous section. This section focuses on two numerical techniques implemented in the code with the purpose of enforcing both boundary conditions for the first-order solution $\chi^{q=1}$.

7.4.1 Parameters

The main parameters of the analysis are reported in table 7.5.

parameter	*value*	*description*	*section*
`maxq`	2	number of harmonics	7.1
`nlev`	300	number of contours	7.2
`bc`	0	main BC	7.3
`addbc`	`no,hgs,nwc`	additional BC	7.4
`bacav`	88%	back-averaging constant	7.5

Table 7.5: Summary of the main parameters of the simulations.

7.4.2 Technique

The main idea behind this section is that a further boundary condition can be imposed by adding a further solution to $\chi^{q=1}$: a Grad-Shafranov solution χ^q_{hgs} or a Newcomb solution χ^q_{nwc}, for example, can be summed to the exact solution χ^q_{exact} from eq. (4.26b),

$$\chi^q = \chi^q_{\text{exact}}(C_1) + \chi^q_{\text{nwc/hgs}}(C_3). \tag{7.1}$$

The additional term $\chi^q_{\text{nwc/hgs}}$ helps in enforcing both boundary conditions, but is responsible for the loss of formal exactness, since $\chi^{q=1}$ from eq. (7.1) is *not* a solution to the HGS equation. Without the additional term, on the other hand, χ^q_{exact} would be the formal solution to the HGS equation but could fail in satisfying both boundary conditions. In such a case, therefore, it could be preferrable to relax the problem to obtain a correctly bounded (yet inexact) solution rather than an incorrectly bounded (but exact) solution.

The two integrations constants C_1 and C_3 can be exploited to enforce *both* boundary conditions at the sensors' radius. Since the main boundary condition typically enforces the radial component $b_r^{m,n}$, the additional solution is constructed so as to help enforcing the toroidal condition $b_\phi^{m,n}$.

The first implemented additional solution is a Newcomb solution, χ^q_{nwc}, obtained through the zeroth-step Newcomb problem with boundary conditions $b_r(r_{\text{sens}}) = 0$ and arbitrary b_ϕ.

The other additional solution is a HGS solution, χ^q_{hgs}, obtained through the helical Grad-Shafranov equation with boundary condition $b_r(r_{\text{sens}}) = 0$.

The addition of either χ^q_{nwc} or χ^q_{hgs} to the original solution does not modify the $b_r(r_{\text{sens}})$ value but can help enforcing the measured $b_\phi(r_{\text{sens}})$ value through the additional C_3 parameter. Schematically,

$$\chi^q_{\mathrm{exact}} \quad \text{such that} \quad b_r(r_{\mathrm{sens}}) = b_r^{m,n}, \tag{7.2a}$$

$$b_\phi(r_{\mathrm{sens}}) \neq b_\phi^{m,n}, \tag{7.2b}$$

$$\chi^q_{\mathrm{nwc/hgs}} \quad \text{such that} \quad b_r(r_{\mathrm{sens}}) = 0, \tag{7.2c}$$

$$\chi^q_{\mathrm{exact}} + C_3\chi^q_{\mathrm{nwc/hgs}} \quad \text{such that} \quad b_r(r_{\mathrm{sens}}) = b_r^{m,n}, \tag{7.2d}$$

$$b_\phi(r_{\mathrm{sens}}) = b_\phi^{m,n}. \tag{7.2e}$$

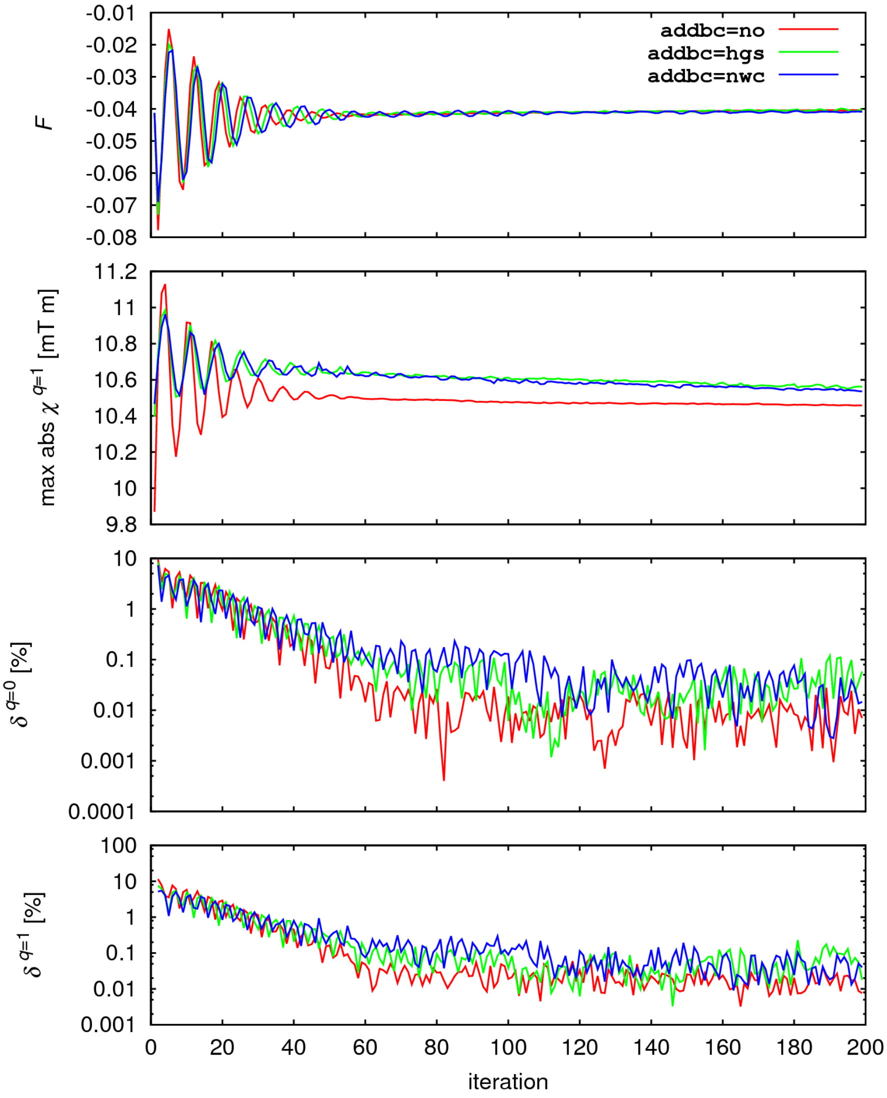

Figure 7.7: Converge paths of F, $\max\mathrm{abs}\,\chi^{q=1}$ and $\delta^{q=0,1}$ for `addbc=no,nwc,hgs`.

7.4.3 Convergence

Let us first take a look at the convergence paths for each of the three simulations. The exact HGS solution is labelled `addbc=no`, whereas the solutions with the Newcomb and helical Grad-Shafranov additional terms are labelled `addbc=nwc` and `addbc=hgs`, respectively.

Figure 7.7 shows that the simulations exhibit a good agreement. The only slight difference is that the `addbc=nwc,hgs` solutions exhibit a higher value for $\max \text{abs}\, \chi^{q=1}$, due to the contributions of the additional terms.

7.4.4 Edge toroidal field

Given the comparable convergence paths of the three simulations, it is interesting to focus then on the additional parameter C_3, that is, on how much of the additional solution is actually needed to satisfy both boundary conditions. For such purpose it is useful to consider, instead of C_3, a normalized parameter

$$C_3^* = \text{abs}\left(\frac{C_3}{1+C_3}\right), \tag{7.3}$$

which measures the relative weight of the additional term in the full solution. For the exact solution, on the other hand, the relative difference between the reconstructed toroidal value b_ϕ^q and the measured $b_\phi^{m,n}$ can be considered by introducing a 'mismatch factor'

$$\Delta_\phi = 1 - \text{abs}\left(\frac{b_\phi^q(r_{\text{sens}})}{b_\phi^{m,n}(r_{\text{sens}})}\right). \tag{7.4}$$

The normalized C_3^* coefficient for `addbc=nwc,hgs` and the mismatch factor Δ_ϕ for `addbc=no` are plotted as percentages in figure 7.8.

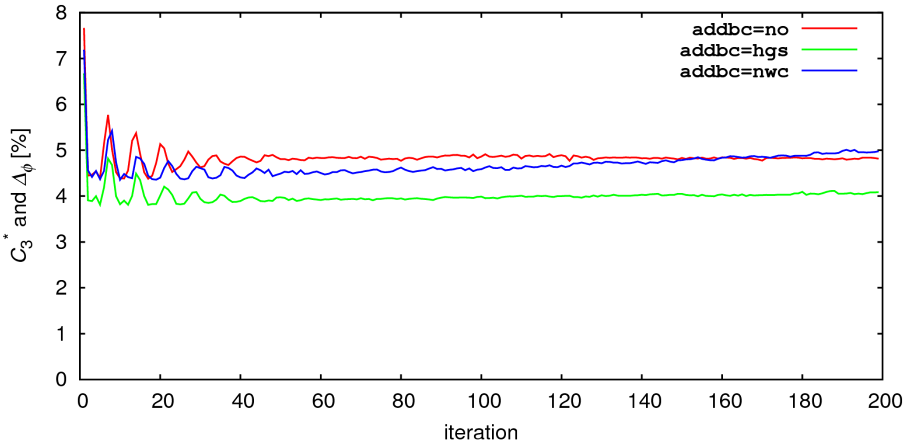

Figure 7.8: Converge paths of the additional normalized coefficient C_3^* for `addbc=nwc,hgs` and of the mismatch factor Δ_ϕ for `addbc=no`.

The `addbc=nwc` run exhibits a slow change in C_3^*, which could be an indication of a lower level of self-consistency than for the `addbc=hgs` run, where C_3^*

does not appear to be changing. The Newcomb and the HGS solutions are found to be approximately $C_3^* \approx 5\%$ and $C_3^* \approx 4\%$, respectively, while the mismatch factor for the exact solution is found to be $\Delta_\phi \approx 5\%$. Interestingly, the mismatch between the exact solution and the toroidal measurement is comparable to the weight of additional solution required to satisfy it.

7.4.5 Solutions

The reconstructed solutions, plotted in figure 7.9, result in good agreement. The only slight differences can be detected upon comparison of the second-order harmonics.

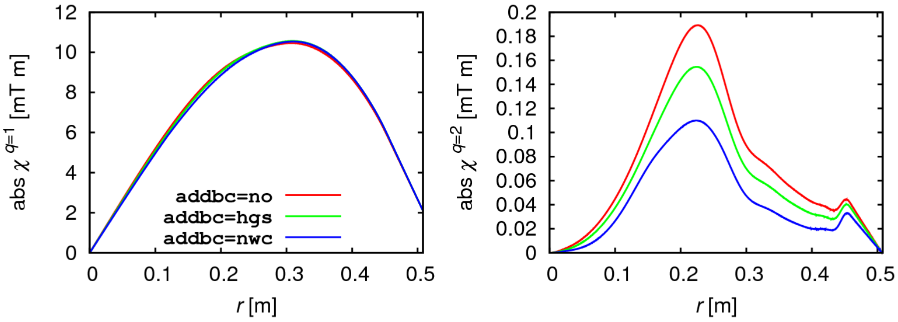

Figure 7.9: Profiles of the computed $q = 1 \div 2$ solutions for `addbc=no,nwc,hgs`.

7.4.6 Conclusions

In the examined case, the three different solutions exhibit noticeable differences only with respect to the reconstructed value for b_ϕ.

The result of figure 7.8 confirms that the C_3^* coefficient measures the mismatch between the reconstructed and the acquired b_ϕ values at the sensors' radius. The problem, therefore, can be tackled equivalently by requiring that the exact solution must satisfy the boundary conditions only within a certain threshold, or that the same threshold is exploited to partially relax the solution by addition of an auxiliary term.

In other cases the addition of the secondary boundary condition could help the overall convergence, rather than just the boundary reconstruction, by enforcing another relevant condition which stabilizes the solution. The benchmark carried out in this section shows that, even though the two additional techniques are not mathematically justified, they still provide valuable physical information.

(page intentionally left blank)

7.5 Back-averaging

The most delicate internal parameter is the constant that controls the back-averaging procedure implemented at the end of each iteration step, as discussed in subsection 6.4.8.

7.5.1 Parameters

In order to understand what happens to the convergence when the back-averaging parameter is changed, a few simulations with different `bacav` constant have been launched. The main parameters of the analysis are reported in table 7.6.

parameter	*value*	*description*	*section*
`maxq`	2	number of harmonics	7.1
`nlev`	300	number of contours	7.2
`bc`	0	main BC	7.3
`addbc`	`no`	additional BC	7.4
`bacav`	84÷90%	back-averaging constant	7.5

Table 7.6: Summary of the main parameters of the simulations.

7.5.2 Convergence

First, let us take a look at the convergence paths, plotted in figure 7.11.

The simulation with `bacav=84` fatally terminates without reaching convergence. The `bacav=86` simulation, on the other hand, completes the 200 steps but fails to converge and continues to oscillate, with both the zeroth- and the first-order convergence factors above 1%. The `bacav=88,90` simulations reach convergence and exhibit good convergence factors, around 0.1%.

7.5.3 Solutions

Then, consider the final solutions for the converged simulations, plotted in figure 7.10.

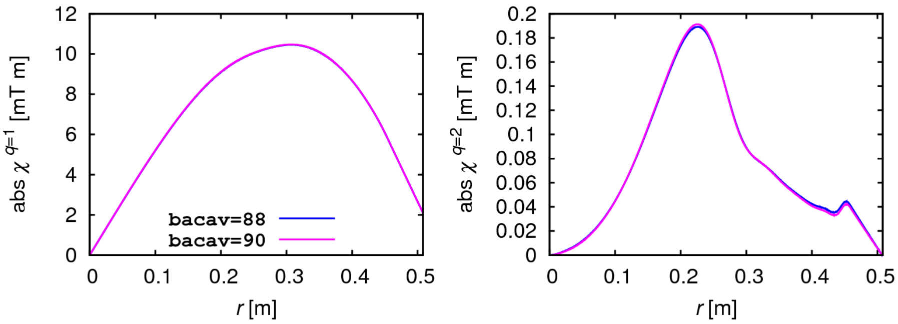

Figure 7.10: Profiles of the computed $q = 0 \div 3$ solutions for `bacav=84÷90`.

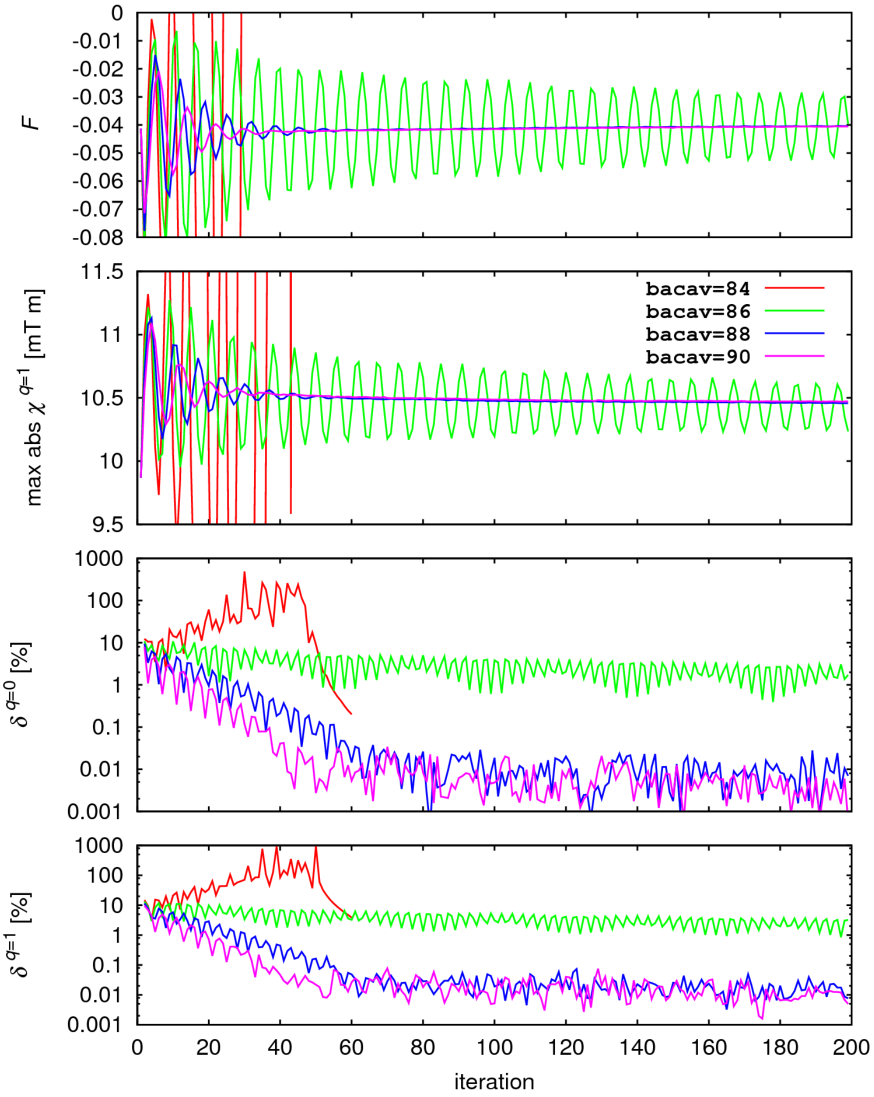

Figure 7.11: Converge paths of F, $\max\text{abs}\,\chi^{q=1}$ and $\delta^{q=0,1}$ for `bacav=84÷90`.

The two converged simulations, `bacav=88,90`, exhibit a nice agreement up to the second-order harmonic.

7.5.4 Conclusions

For the analysed simulation, the optimal convergence constant is found to be `bacav=88`, which represents the best ratio of new information input to convergence robustness among the cases considered.

7.5.5 Threshold analysis

It is interesting to investigate whether the observed back-averaging threshold – which for the previous analysis was around `bacav`$\approx$`88` – depends upon the amplitude of the analysed perturbation, rather than being constant or determined from unknown dynamics. This would eventually help `hegrasha` in automatically setting the best back-averaging parameter to use in a given configuration.

Parameters

A large database of simulations, based on the same shot as before, has therefore been populated and analysed through a two-dimensional parameter scan: the back-averaging constant, ranging from 90% to 99.5%, is varied together with the perturbation amplitude, ranging from 5% to 75%.

parameter	*value*	*description*	*section*
`maxq`	`2`	number of harmonics	7.1
`nlev`	`300`	number of contours	7.2
`bc`	`0`	main BC	7.3
`addbc`	`no`	additional BC	7.4
`bacav`	`90÷99.5%`	back-averaging constant	7.5
`scafa`	`5÷75%`	scaling factor	7.5

Table 7.7: Summary of the main parameters of the simulations.

We write 'amplitude' of the perturbation because the corresponding parameter is indeed directly linked with the physical magnitude of the perturbation through the imposition of the boundary conditions for the first-order solution during the zeroth-step Newcomb reconstruction. The parameter, in fact, is the scaling factor, `scafa`, that multiplies the toroidal component of the perturbed magnetic field measured at the sensors' radius and used as boundary condition: a factor of 50% means that the experimentally measured value has been divided by 2 before being used to impose the boundary conditions.

The radial component of the perturbed magnetic field is enforced to zero, following the ideal shell approximation (6.2), even for the first harmonic $q = 1$. Schematically, for the initial guess one has

$$b_r(r_{\text{sens}}) = 0, \tag{7.5a}$$

$$b_\phi(r_{\text{sens}}) = \texttt{scafa} \cdot b_\phi^{m,n}(r_{\text{sens}}), \tag{7.5b}$$

while for the iteration step one has

$$b_r(r_{\text{sens}}) = 0. \tag{7.6}$$

The final reconstructed solutions with respect to two different scaling factors have different shape as well as different amplitude, but the corresponding *initial* profiles must have the same shape, although different amplitude, since they are computed through a Newcomb approach, which is linear.

Convergence

The convergence summary is plotted in figure 7.12.

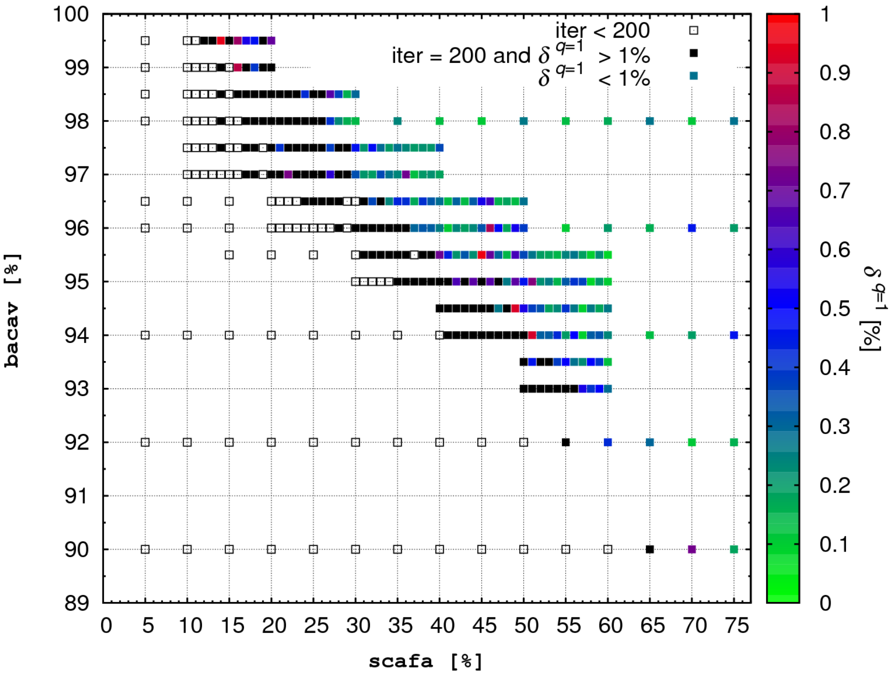

Figure 7.12: Convergence summary for `scafa=5÷75%` and `bacav=90÷99.5%`.

Three categories have been considered: the first one is the set of simulations that failed to complete, that is, the simulations that fatally terminated and did not run for 200 steps; the second one is the set of simulations that failed to converge, that is, the ones that completed the 200 steps but whose first-order convergence factor was above a specified threshold; the third one is the set of the converged simulations, that is, the ones with convergence factor below the same threshold. The threshold has been chosen at 1%, and below such value the color legend applies.

A definite dependence of the back-averaging threshold from the perturbation amplitude is evident from figure 7.12: the higher the perturbation amplitude, the lower the required `bacav` constant for convergence. In fact, the simulations with scale factor lower than 20% failed to converge for almost any back-averaging parameter up to 99.5%, whereas the ones with scale factor higher than 50% had the opposite behaviour, exhibiting no fatal terminations and converging with `bacav` as low as 94%.

Solutions

During the iteration procedure the only enforced boundary condition is the ideal shell condition on b_r (7.6), so that the final solutions do not necessarily satisfy the boundary condition on b_ϕ (7.5b). In order to verify that simulations which start from small scales, e.g. `scafa=50%`, converge towards comparable scales, e.g. `scafa`≈`50%`, a further analysis can be carried out.

Figure 7.13 shows the profiles of the final b_ϕ solutions for simulations with scale factor `scafa=30÷60%` and appropriate back-averaging parameter. As a comparison, the `scafa=75%` simulation has been also plotted twice, scaled back to `scafa=30%` and `scafa=60%`.

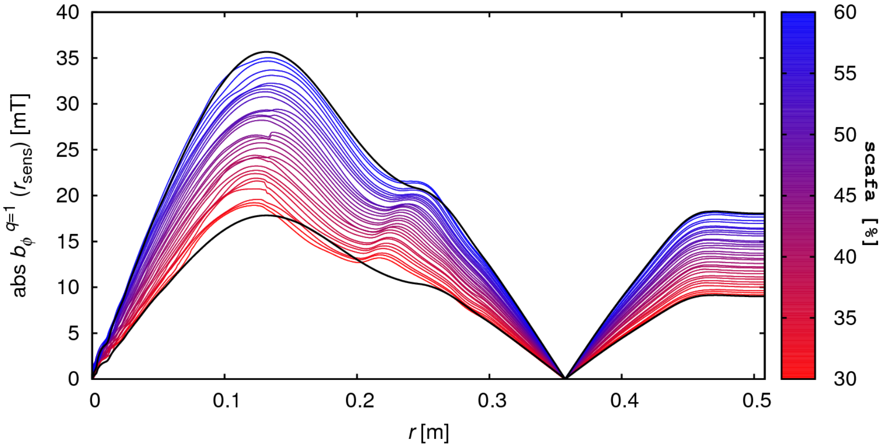

Figure 7.13: Converged profiles of $\mathrm{abs}\, b_\phi^{q=1}$ for `scafa=30÷60%`.

The analysis of figure 7.13 confirms the the converged simulations maintain a scale factor consistent with the initial one.

Conclusions

The threshold analysis clearly indicates that the back-averaging parameter necessary for convergence gets higher as the perturbation gets lower, and that a certain threshold of amplitude exists below which no convergence is possible.

CHAPTER 8

Results

This chapter will present and discuss in detail the results of the Fortran code.

As anticipated in section 5.1, the helical Grad-Shafranov code is applied in section 8.1 to a SHAx state based on the dominant $m = 1$, $n = 7$ tearing mode during a RFP shot in RFX-mod, and in section 8.2 to a MHAx state based on the $m = 2$, $n = 1$ tearing mode, which is typical of tokamak discharges, during a tokamak shot in RFX-mod.

8.1 SHAx state

This section will investigate the result obtained by applying `hegrasha` to the shot #23810 at 80 ms in RFX-mod, which is a SHAx state in a QSH RFP configuration, generated by the dominant $m = 1$, $n = 7$ tearing mode.

8.1.1 Parameters

Experimental

The most important external parameters are reported in table 8.1.

parameter	*value*	*description*
F	-0.036	acquired
Θ	1.420	"
I_P	1.437	"
α	4.798	fitted
Θ_0	1.490	"
F	-0.045	initial
Θ	1.403	"

Table 8.1: Experimental parameters for shot #23810 at 80 ms: I_P is expressed in MA.

Note that, for both the F and Θ parameters, the distinction between the *acquired* and *initial* labels is the one explained in subsection 6.2.3: the former are read directly from the pulse file, while the latter are the one resulting from an α-Θ_0 equilibrium computation with the *fitted* values for such constants.

Numerical

Then, let us summarize in table 8.2 the main internal parameters for `hegrasha`, adjusted and optimized following the analyses of chapter 7.

parameter	*value*	*description*
`maxq`	2	number of harmonics
`nlev`	300	number of contours
`bc`	0	main BC
`addbc`	no	additional BC
`bacav`	88	back-averaging constant

Table 8.2: Internal parameters for `hegrasha` for the analysed simulation.

8.1.2 Convergence

Then, let us consider the convergence path.

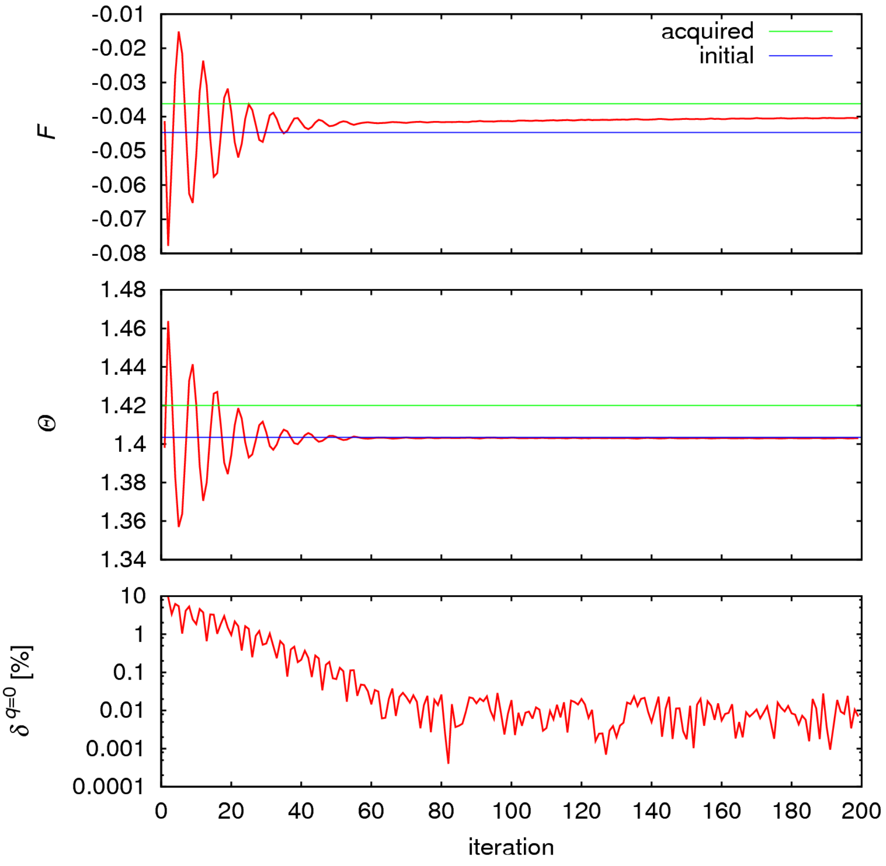

Figure 8.1: F, Θ and $\delta^{q=0}$ for the final simulation.

Zeroth order

The main zeroth-order quantities – F, Θ and $\delta^{q=0}$ – are plotted in figure 8.1. For F and Θ, the read and computed values from table 8.1 are plotted as well.

Each quantity converges towards a well definite value, and in particular the F and Θ parameters result in good agreement with the initial values. The zeroth-order convergence factor, indeed, confirms that the zeroth-order quantities are extremely self-consistent and are characterised by a $\delta^{q=0} \approx 0.01\%$.

First order

The main first-order quantities – $\max \operatorname{abs} \chi^{q=1}$, $b_\phi^{q=1}$ and $\delta^{q=1}$ – are plotted in figure 8.2. For $b_\phi^{q=1}$, the experimentally measured value is also plotted.

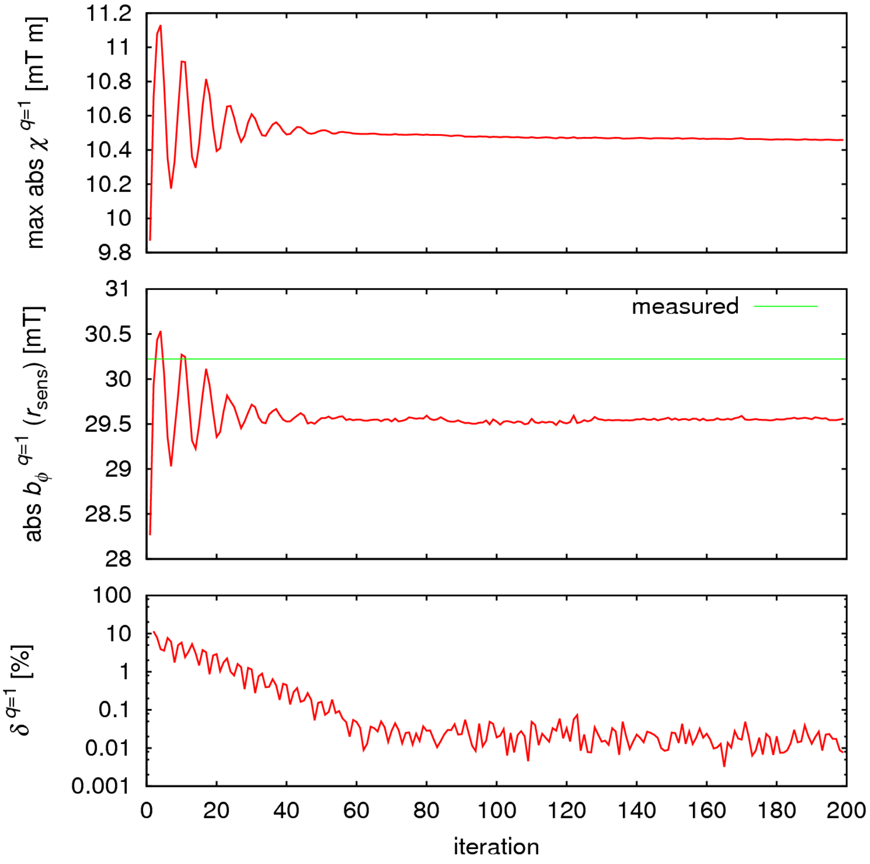

Figure 8.2: $\max \operatorname{abs} \chi^{q=1}$, $b_\phi^{q=1}$ and $\delta^{q=1}$ for the final simulation.

Both $\max \operatorname{abs} \chi^{q=1}$ and $b_\phi^{q=1}$ converge pretty fast towards the final value. The toroidal magnetic field converges towards a value which differs from the experimentally determined value of about 4.8%. The first-order convergence factor, moreover, is found to be less than 0.1%.

8.1.3 Solutions

The $q = 0 \div 2$ harmonics of the reconstructed solutions for χ, b_ϑ and b_ϕ are plotted in figure 8.3. For $q = 0 \div 1$ the initial guesses, deriving from the α-Θ_0 equilibrium and the Newcomb solution respectively, are plotted as well.

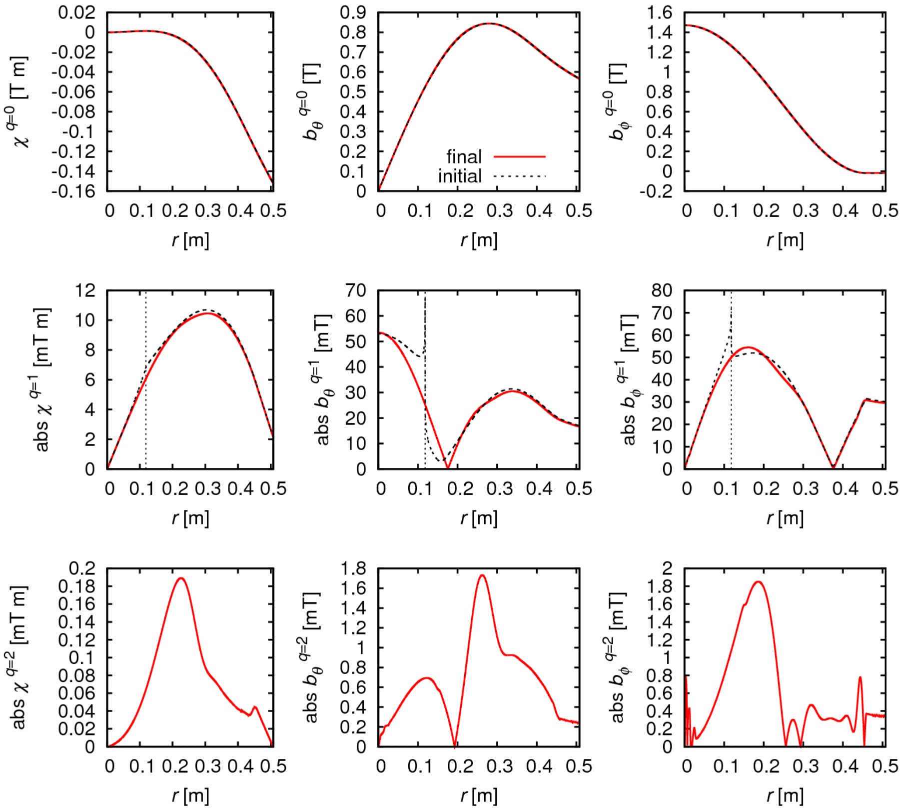

Figure 8.3: Final $q = 0 \div 2$ harmonics for χ, b_ϑ and b_ϕ.

The agreement between the initial guesses and the final solutions is evident. The main difference in the $q = 1$ harmonic is the behaviour near the resonant radius, highlighted by a vertical line in figure 8.3. The Newcomb $\chi^{q=1}$ solution, in fact, presents a discontinuity in its first derivative at r_s, while the $b_\vartheta^{q=1}$ and $b_\phi^{q=1}$ are actually discontinuous.

8.1.4 Topology

The comparison of the reconstructed solutions with the zeroth-step guess carries significant physical information, since it sheds light on the agreement between the two different models, that is, the linear Newcomb treatment and the non-linear helical Grad-Shafranov model. It is interesting, therefore, to compare not only the solutions, but also the topology of the flux surfaces between the zeroth- and the last iteration step.

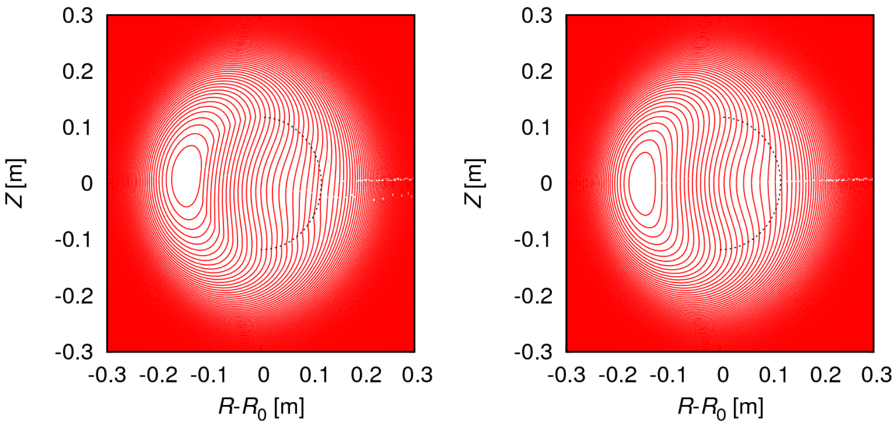

Figure 8.4: Comparison of the initial (left panel) and final (right panel) flux surfaces.

Figure 8.4 shows that the flux surfaces for the initial and the final step are in good agreement, the main difference being the behaviour on the resonant surface. Such surface, partially plotted in each panel as a dashed line, is where the Newcomb solution exhibits a discontinuity in the first derivative. Some of the contours in the left panel, therefore, are characterised by a 'broken' contour line, whereas in the right panel the contours are smooth.

Furthermore, a minor difference in the position of the helical axis can be detected due to a slight phase difference of the reconstructed solutions.

8.1.5 Conclusions

Summarizing, the analysed simulation converges extremely neatly around reasonable values for the main zeroth- and first-order quantities: the F and Θ parameters can be found in good agreement with the initial values, and the first-order solutions are in excellent agreement with the initial Newcomb guess. On one hand, it is not a surprising result since the initial guess heavily influences the whole convergence path but, on the other hand, it confirms that the linear Newcomb prediction agrees with a helical Grad-Shafranov model.

The only difference is that the helical Grad-Shafranov solution, exploiting a single boundary condition, cannot exactly match the toroidal component and differs from the experimental value of approximately 5%, as discussed in subsection 7.4.4.

8.2 MHAx state

The helical Grad-Shafranov code, as introduced in section 5.1, can be applied also to a MHAx state.

This section applies `hegrasha` to the tokamak shot #30417 at 500 ms on RFX-mod and focuses on the $m = 2$, $n = 1$ tearing mode, which produces a MHAx topology.

Since the $m = 2$ poloidal mode number is the Fourier harmonic connected with the ϑ poloidal angle, two helically twisted axes can be seen in the polar section, corresponding to a single $q = 1$ mode number in the u helical angle.

8.2.1 Parameters

Experimental

The most important parameters of the experimental configuration are reported in table 8.3.

parameter	*value*	*description*
I_P	1.101	acquired
α	1.65	fitted
Θ_0	0.24	"
$q(0)$	0.956	initial
$q(a)$	2.514	"

Table 8.3: Experimental parameters for shot #30417 at 500 ms: I_P is in MA.

The initial edge safety factor value, $q(a) = q_a$, is obtained from the measured plasma current and the edge toroidal field, while the initial axis safety factor value, $q(0) = q_0$, is known to be $q_0 \approx 1$ given the sawtoothing observed in SXR measurements.

Numerical

The internal parameters for the `hegrasha` simulation are summarized in table 8.4.

parameter	*value*	*description*
`maxq`	2	number of harmonics
`nlev`	300	number of contours
`bc`	0	main BC
`addbc`	hgs	additional BC
`bacav`	90	back-averaging constant

Table 8.4: Internal parameters for `hegrasha` for the analysed simulation.

Notice that, differently than the SHAx state, the analysed MHAx state needs the additional boundary condition characterised in section 7.4 in order to find convergence. The chosen additional solution is the helical Grad-Shafranov χ^q_{hgs}.

8.2.2 Convergence

Let us consider the convergence path.

Zeroth order

The main zeroth-order quantities – q_0, q_a and $\delta^{q=0}$ – are plotted in figure 8.1.

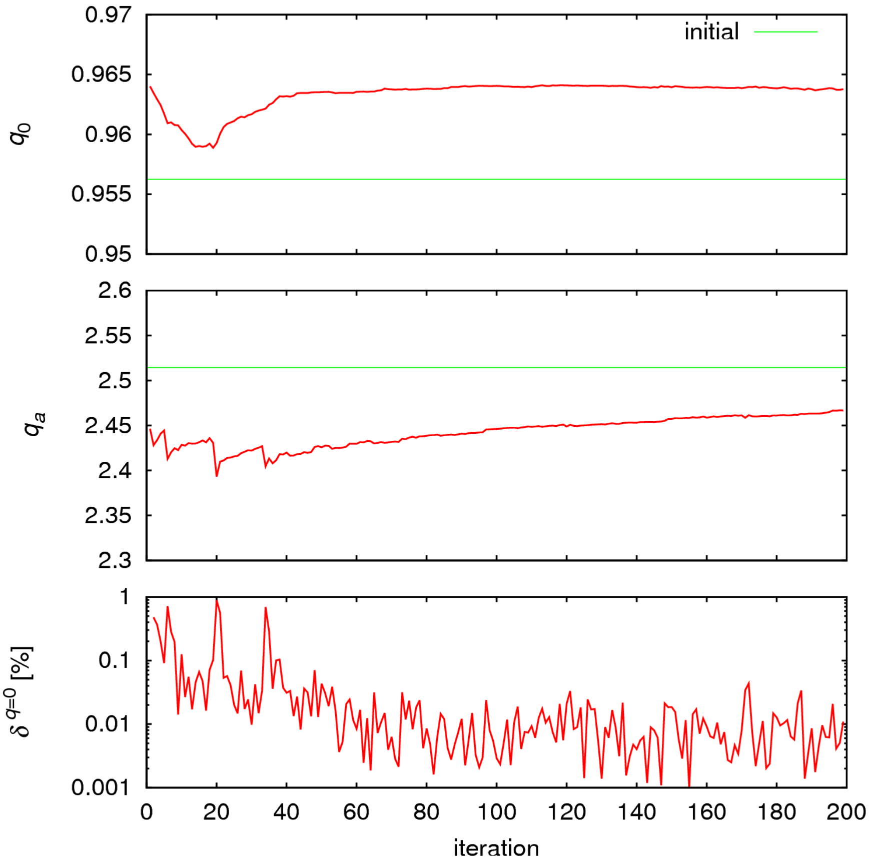

Figure 8.5: q_0, q_a and $\delta^{q=0}$ for the final simulation.

Even though the convergence path is less neat than that of the SHAx state, and in particular a slow change in q_a can be detected, the plotted quantities seem to converge nonetheless, with the zeroth-order convergence factor of about 0.01%.

First order

The main first-order quantities – $\max\text{abs}\,\chi^{q=1}$, C_3^* and $\delta^{q=1}$ – are plotted in figure 8.2.

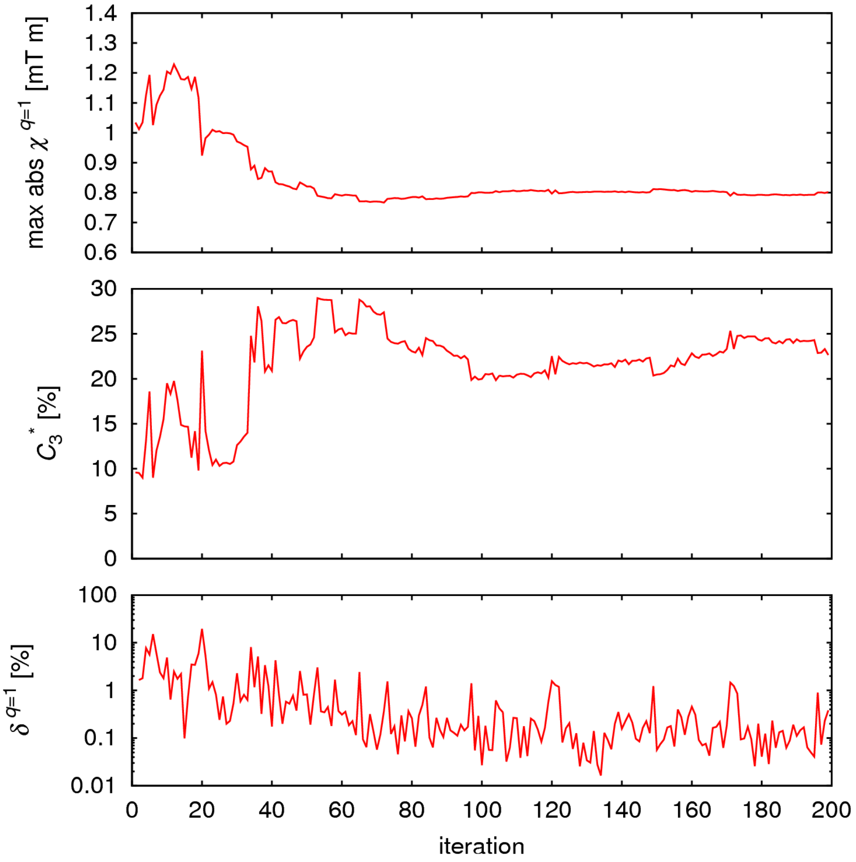

Figure 8.6: $\max\text{abs}\,\chi^{q=1}$, C_3^* and $\delta^{q=1}$ for the final simulation.

Similarly to the zeroth-order quantities, the first-order quantities converge towards definite final values. The additional boundary condition parameter is found to be $C_3^* \approx 23\%$, which is an indication of the amount of additional solution that has been added to the original solution. The first-order convergence factor, is found to be lower than 0.5%.

8.2.3 Solutions

The $q = 0 \div 2$ harmonics of the reconstructed solutions for χ, b_ϑ and b_ϕ are plotted in figure 8.7. For $q = 0 \div 1$ the initial guesses, deriving from the α-Θ_0 equilibrium and the Newcomb solution respectively, are plotted as well.

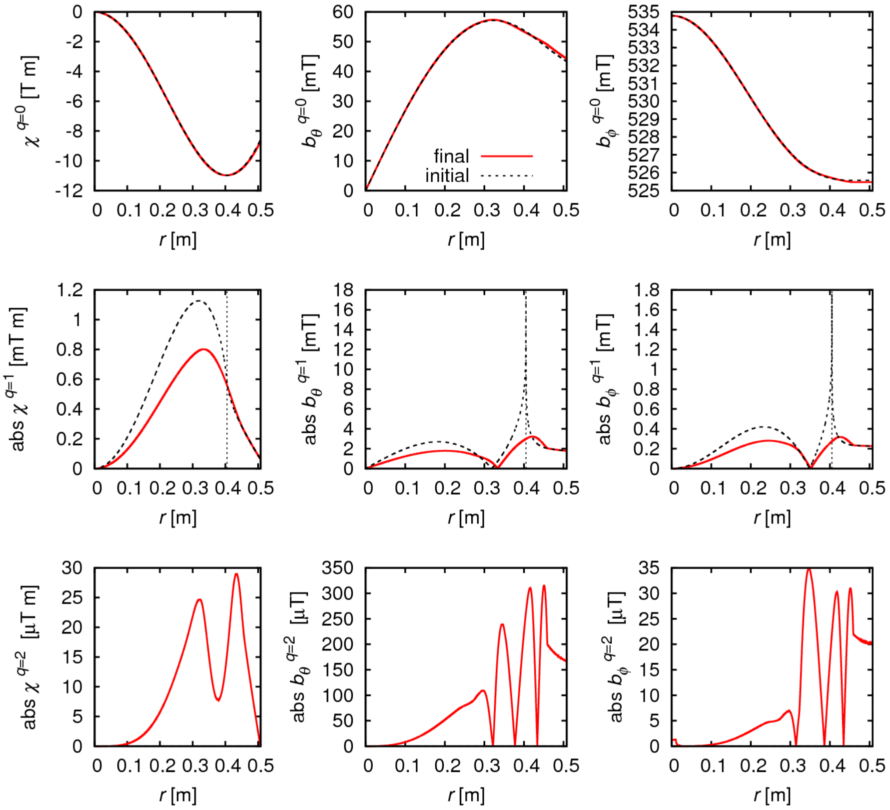

Figure 8.7: Final $q = 0 \div 2$ harmonics for χ, b_ϑ and b_ϕ.

The zeroth-order solutions are found to agree with the initial guesses, but a slight difference at the plasma edge can nonetheless be detected.

The first-order b_r profile is found to be quite different from the Newcomb prediction, expecially in the internal region, $r < r_s$. The first-order b_ϑ and b_ϕ profiles, on the other hand, exhibit only minor differences with respect to the Newcomb guesses, most evidently in the resonant region, $r \approx r_s$.

8.2.4 Topology

A comparison of the initial and final flux surfaces is plotted in figure 8.8.

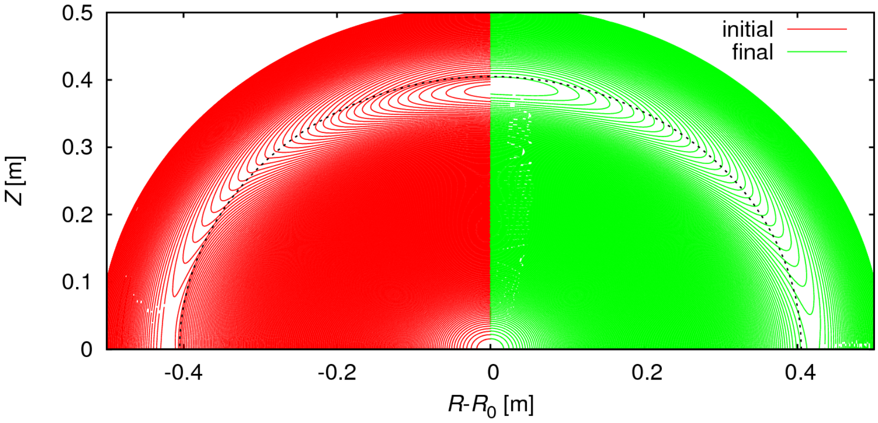

Figure 8.8: Comparison of the initial and final flux surfaces.

As was clear from the radial profiles of the solutions, the main differences are in the region near the resonance (plotted as a dashed line), towards the inner side. The helical axis appears in a slightly different position, and the flux surfaces nearest to the helical axis exhibit the biggest difference. The agreement is nonetheless still reasonable.

8.2.5 Conclusions

In summary, the helical Grad-Shafranov can be applied to a $m = 2$, $n = 1$ tearing mode in a tokamak shot as well, but the solution is much less straightforward than for the SHAx RFP configuration: in particular, a much lower degree of self-consistency can be obtained, highlighted by the need for a $C_3^* \approx 23\%$ additional solution.

Part III

VMEC and V3FIT

CHAPTER 9

Code suite

The purpose of this chapter is to introduce the VMEC equilibrium computation code and the V3FIT equilibrium reconstruction tool.

The VMEC/V3FIT code suite will be exploited, in Chapter 10, as a benchmarking algorithm for the `hegrasha` code developed in Chapter 6. A new diagnostic for V3FIT, furthermore, will be introduced and discussed in Chapter 11.

9.1 Introduction

Three-dimensional equilibrium solvers have been first envisaged in the stellarator community, given the natural and intrinsic three-dimensionality of such devices. The change in paradigm occurred in recent years among the fusion community has highlighted the need for robust three-dimensional reconstruction tools for axisymmetric devices as well. On one hand, RFPs have suggested the possibility of obtaining improved confinement regimes thanks to three-dimensional helical states and, on the other hand, tokamak experiments with external perturbations have requested a lot of asymmetric physics analysis. For such reasons, three-dimensional reconstructions are extremely important from both a predictive, modeling and operational standpoint.

Equilibrium reconstruction is a complex process that can be thought of as comprising two subproblems. On one hand the core equilibrium solver, VMEC, focuses on the direct problem of computing a plasma equilibrium given *a* set of input parameters. V3FIT, on the other hand, tackles the inverse problem of finding *the* set of input parameters that yields the best-fitting equilibrium for a given set of experimental measurements and within a given threshold.

9.2 VMEC

The Variational Moments Equilibrium Code (VMEC) is a numerical tool for the solution of the 'direct', or 'forward', problem of computing the three-dimensional plasma equilibrium deriving from a given set of parameters.

This section will introduce and discuss the main features of the code. For a complete reference, see the 1983 paper by Hirshman and Whitson [Hir83] and the following papers [Hir86, Hir91].

9.2.1 Assumptions and equations

The VMEC code computes the equilibrium of a static isotropic plasma, without fluid flow, by exploiting an energy minimization principle. VMEC, moreover, assumes the plasma is characterised by nested and conserved flux surfaces, so that it cannot be applied to configurations with magnetic islands or with chaotic structures.

The equations that have to be solved are the force-balance equation and Ampère's and Gauss' laws,

$$\mathbf{F} \equiv -\mathbf{J} \times \mathbf{B} + \nabla p = 0, \tag{9.1a}$$

$$\nabla \times \mathbf{B} = \mu_0 \mathbf{J}, \tag{9.1b}$$

$$\nabla \cdot \mathbf{B} = 0, \tag{9.1c}$$

where $\mathbf{F}$ is the 'residual MHD force', which has to vanish in equilibrium.

9.2.2 Flux coordinates

Flux coordinates (s, u, v) are exploited – labelled (ρ, θ, ζ) in the original paper by Hirshman and Whitson. The s coordinate is a normalized flux label,

$$s = \frac{\chi - \chi_{\text{min}}}{\chi_{\text{max}} - \chi_{\text{min}}}, \tag{9.2}$$

where χ corresponds to the *poloidal* flux Ψ for a RFP and to the *toroidal* flux Φ for a tokamak. The u coordinate is a poloidal angle chosen so as to minimize the harmonic content of the Fourier problem which is, in general, incompatible with the requirement that in (s, u, v) coordinates the magnetic field lines appear straight. The v coordinate is connected to the machine toroidal angle ϕ through the toroidal periodicity `NFP`, which will be introduced in subsection 9.2.4.

The magnetic field $\mathbf{B}$ can be expressed in contravariant form

$$\mathbf{B} = \nabla v \times \nabla \Psi + \nabla \Phi \times \nabla u \tag{9.3a}$$

$$= B^u \mathbf{e}_u + B^v \mathbf{e}_v. \tag{9.3b}$$

In such a way the $\mathbf{B} \cdot \nabla p = 0$ and $\nabla \cdot \mathbf{B} = 0$ conditions are automatically satisfied. The basis vectors for the co- and contra-variant coordinates [D'h91] are defined as

$$\mathbf{e}_i = \frac{\partial \mathbf{x}}{\partial \alpha_i}, \tag{9.4a}$$

$$\mathbf{e}^i = \nabla \alpha_i, \tag{9.4b}$$

where $\mathbf{x}$ are the cartesian coordinates and $\alpha_i = \{s, u, v\}$.

9.2.3 Energy minimization

A variational principle in terms of the plasma energy

$$W = \int \left(\frac{|\mathbf{B}|^2}{2\mu_0} + \frac{p}{\gamma - 1} \right) \mathrm{d}^3 x, \tag{9.5}$$

where $\gamma \geq 0$ is the adiabatic index, is applied to solve the equilibrium equations (9.1). Since W is scalar invariant an 'inverse representation' is used, where the flux coordinates (s, u, v) are considered the independent variables and the cartesian coordinates $\mathbf{x}$ are considered dependent variables,

$$(s, u, v) \longmapsto \mathbf{x} = \mathbf{x}(s, u, v). \tag{9.6}$$

VMEC follows a 'steepest-descent method', which is an iterative technique for following the path in the phase space of the moment amplitudes along which the steepest decrease towards the W minimum is found. The Fourier harmonics of the residual force $\mathbf{F}$ are minimized at each iteration.

In particular, each quantity Q is determined throughout the code as a Fourier series in terms of sine and cosine harmonics of the (s, u, v) flux coordinates,

$$Q = \sum_{m,n} Q_{\mathrm{c}}^{m,n} \cos(mu - nv) + Q_{\mathrm{s}}^{m,n} \sin(mu - nv). \tag{9.7}$$

9.2.4 Input parameters

Plasma parameters

The total enclosed toroidal flux Φ_{tot} and the plasma current I_P have to be provided to VMEC, together with the profile of the plasma pressure p and of the helical safety factor q_h, defined as

$$q_h(s) = \frac{\mathrm{d}\Phi}{\mathrm{d}\Psi}(s). \tag{9.8}$$

Each profile can be expressed through the many parameterizations currently supported by VMEC such as, but not limited to, a two-power model or a spline interpolation. An example of the two-power model for p is

$$p(s) = a_0 + a_1(1 - s^{a_2})^{a_3}, \tag{9.9}$$

whereas an example of a spline for q_h is plotted in figure 9.1.

Generally, the (s, q) points to be interpolated are chosen carefully. In figure 9.1, for example, there are five: the first controls the safety factor on axis, the second and the third control the maximum value and the possibility of a hollow profile, the fourth controls the position for the reversal surface and the fifth controls the value for the edge safety factor.

Boundary parameters

Since boundary conditions have to be enforced in the computation, the outermost flux surface has to be specified. Two approaches are supported with respect to the modelization of the magnetic boundary.

In the *fixed-boundary* approach, VMEC needs to know which is the *fixed* last closed flux surface, $s = 1$. Both R and Z have to be specified as a function of the flux coordinates (s, u, v), and in particular the $R_{\mathrm{c,s}}^{m,n}$ and $Z_{\mathrm{c,s}}^{m,n}$ harmonics of the decomposition (9.7) have to be provided.

In the *free-boundary* approach, VMEC does not need to know where the last closed flux surface is, but where the external coils are, instead. The information about the external coils, in fact, is exploited to self-consistently compute the magnetic boundary, provided the currents flowing in such coils are known. Passive structures are not considered in the model.

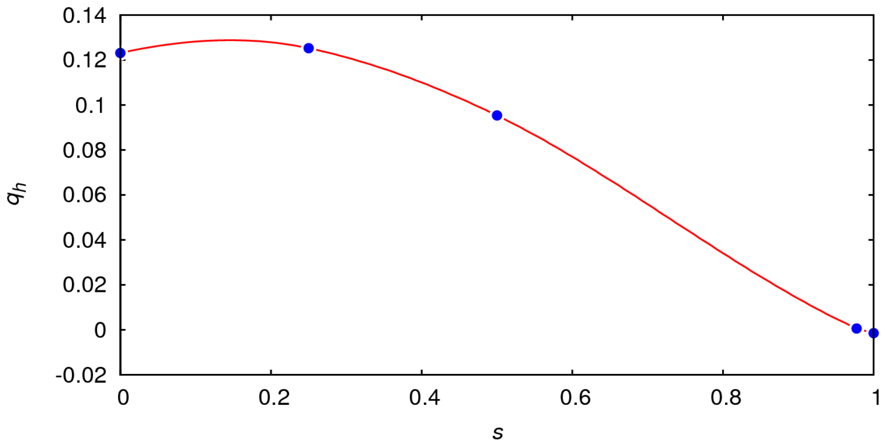

Figure 9.1: The helical safety factor q_h is plotted as a series of points (blue) to be interpolated with a spline function (red) by VMEC.

Computational parameters

The harmonic content of the computations has then to be specified. Such parameters include the toroidal periodicity of the configuration, `NFP`, which defines the symmetry of the toroidal angular dependence, and the poloidal and toroidal number of harmonics, `MPOL` and `NTOR`. The toroidal harmonics, in particular, are harmonics in terms of `NFP`, so that the first harmonic is indeed `NFP`. In typical RFX-mod computations, for example, `MPOL=9`, `NTOR=6` and `NFP=7`, following the toroidal mode number of the dominant tearing mode.

9.3 V3FIT

The V3FIT code, on the other hand, tackles the 'inverse' problem of computing the plasma equilibrium that best fits a given set of experimental measurements, currently relying on VMEC as core equilibrium solver.

V3FIT, in other terms, iteratively executes VMEC to determine the set of reconstruction parameters which leads to modelled signals that best interpret the provided experimental signals. Each of the following subsections will introduce and describe those features that will be used in the next chapters. For a complete reference, see the 2009 paper by Hanson *et al* [Han09].

9.3.1 Parameters

The parameters, $\mathbf{p}$, are the V3FIT-internal quantities necessary for the determination of the modelled signals. The *reconstruction* parameters, $\mathbf{p}^{\mathrm{r}}$, are a subset of those, and represent the ultimate goal of the fitting procedure. The convergence of V3FIT, in fact, corresponds to the determination of the optimal $\mathbf{p}^{\mathrm{r}}$ and to the computation of the final equilibrium.

Most of the VMEC input parameters, introduced in subsection 9.2.4, can be flagged as reconstruction parameters, but there are more V3FIT-specific quantities that can be specified using one of the many VMEC-supported parameterized profiles. Examples of V3FIT-specific quantities are the density and temperature profiles – and their interdependence – or the soft x-ray emissivity profile.

9.3.2 Model

The set of modelled signals, $\mathbf{d}^{\mathrm{m}}(\mathbf{p})$, is computed by V3FIT in order to quantify the mismatch against the observed signals, as will be explained in the subsection 9.3.4.

The V3FIT-specific requirements provide additional information on top of the VMEC computations. The extra physics is necessary to self-consistently compute certain modelled signals, e.g. Thomson scattering measurements, since they cannot be compared directly to the VMEC-computed quantities, but only indirectly through pressure and density.

Another important aspect of the modelling of *external* magnetic measurements in V3FIT is that in fixed-boundary reconstructions the vacuum contribution to such measurements has to be determined separately and independently from the plasma contribution, since it cannot be deduced from VMEC-internal data. For reference, see [Ter13].

9.3.3 Diagnostics

The last ingredient in the V3FIT minimization recipe is the set of experimentally observed signals, $\mathbf{d}^{\mathrm{o}}$, that provide the physical information to be interpreted. It is important to stress that V3FIT is linked to the VMEC toroidal periodicity and consequently is able to model magnetic measurements only in terms of `NFP` harmonics.

The diagnostic system for RFX-mod has been briefly discussed in subsection 2.3.1. Typical V3FIT reconstructions exploit both magnetic diagnostics – saddle coils, pick-up coils, flux loops and the new virtual diagnostic introduced in chapter 11 – and kinetic diagnostics – Thomson scattering, SXR and interferometer.

From the diagnostic point of view V3FIT is extremely robust, since its modular nature makes it possible to add and modify diagnostics at will. The implementation of the new `extcurz` diagnostic is discussed in chapter 11 as a tool for matching the edge safety factor value.

9.3.4 Minimization procedure

The core mechanism for V3FIT is the minimization of the mismatch between the observed data signals, $\mathbf{d}^{\mathrm{o}}$, and the modelled data signals, $\mathbf{d}^{\mathrm{m}}$, which are computed as a function of the model parameters, $\mathbf{p}$. The mismatch between the two sets of signals is computed through the χ^2,

$$\chi^2 = \sum_i w_i \cdot \left(\frac{d_i^{\mathrm{o}} - d_i^{\mathrm{m}}(\mathbf{p})}{\sigma_i} \right)^2 , \tag{9.10}$$

where each observed signal has weight w_i and experimental error σ_i, and is minimized through a quasi-Newton algorithm. The weight is just a way of 'switching off' diagnostics, that is, of neglecting the relative mismatch in the sum of the χ^2, and will prove extremely useful in the analyses of Chapter 11.

In V3FIT the signal errors are assumed as independent, but nonetheless a more refined equation for χ^2 – and for the quantities that will be defined next – can be introduced: for reference, see [Han10].

The data covariance matrix $\mathbf{C}^{\mathrm{o}}$ is defined as

$$(\mathbf{C}^{\mathrm{o}})_{ij} = \sigma_i \sigma_j \delta_{ij}, \tag{9.11}$$

and the posterior parameter covariance matrix $\mathbf{C}^{\mathrm{p}}$ as

$$(\mathbf{C}^{\mathrm{p}})^{-1} = \mathbf{J}^T \cdot (\mathbf{C}^{\mathrm{o}})^{-1} \cdot \mathbf{J}, \tag{9.12}$$

where $\mathbf{J}$ is the Jacobian of the modelled signals with respect to the model parameters,

$$\mathbf{J}_{ij} = \frac{\partial d_i^{\mathrm{m}}}{\partial p_j}(\mathbf{p}). \tag{9.13}$$

The Jacobian is exploited in V3FIT for a singular value decomposition (SVD) analysis, and represents another useful measurement of the relationship between each parameter and each modelled signal. Furthermore, the diagonal elements of the posterior parameter covariance matrix,

$$\sigma_i^{\mathrm{p}} = \sqrt{(\mathbf{C}^{\mathrm{p}})_{ii}}, \tag{9.14}$$

quantify the uncertainty in the reconstructed value of the i-th parameter. Finally, the signal effectiveness matrix can be introduced,

$$E_{ij} = \frac{\sigma_j}{\sigma_i^{\mathrm{p}}} \frac{\mathrm{d}\sigma_i^{\mathrm{p}}}{\mathrm{d}\sigma_j}, \tag{9.15}$$

that shows which signals are most important in determining which parameters. The higher the signal effectiveness E_{ij} for a signal s_j, the more it matters in determining the parameter p_i. The signal effectiveness is non-negative and normalized to unity,

$$\sum_j E_{ij} = 1. \tag{9.16}$$

9.3.5 Iterative procedure

Let us then briefly summarise the main operational steps in a V3FIT run.

First, VMEC is executed to compute the equilibrium with the original reconstruction parameters. The modelled signals are computed and the χ^2 is obtained from eq. (9.10).

After that VMEC is executed again, once for each reconstruction parameter p_i^{r}: in each new execution, all the parameters have their original value, except for the i-th parameter which is slightly varied. The χ^2 is computed after each execution, and the Jacobian is then obtained by composition of the i partial Jacobians.

The SVD analysis is finally performed: the algorithm then computes the steps to be applied to each reconstruction parameter, and the iteration starts again from the top with an updated parameter vector $\mathbf{p}$.

CHAPTER 10

Benchmark

This chapter will introduce and discuss the benchmark of the `hegrasha` helical Grad-Shafranov solver through comparison with the VMEC equilibrium solver and the V3FIT equilibrium reconstruction tool.

Under scrutiny is a `hegrasha` simulation based on shot #30843, which is extremely similar to the shot #23810 discussed in section 8.1, but which benefits from a much more complete diagnostic setup. All the discussions of section 8.1 with respect to the SHAx state, the dominant m, n mode or the shallow F still stand.

10.1 Simulations

As explained for `hegrasha` in subsection 6.2.2, and for VMEC/V3FIT in sections 9.2 and 9.3, the external input data and the internal working parameters are extremely different for each code.

On one hand, the two-dimensional `hegrasha` code assumes cylindrical coordinates and a helically symmetric MHD perturbation spectrum, starts from an initial Newcomb linear model for the $m = 1$, $n = 7$ dominant tearing mode on an underlying α-Θ_0 equilibrium, solves the helical Grad-Shafranov equation and enforces at each iteration $b_r = b_r^{m,n}$ for $q = 1$ and $b_r = 0$ for $q = 2$.

On the other hand, the three-dimensional VMEC code assumes generalized curvilinear coordinates, considers a rich spectrum in m modes, starts from a fixed boundary and a helical safety factor profile q_h, and minimizes the magnetic energy. On top of that, V3FIT exploits hundreds of both magnetic and thermal diagnostics to minimize the χ^2 mismatch.

For such reasons, two simulations have been launched: a hybrid VMEC computation and a full VMEC/V3FIT reconstruction.

10.1.1 Hybrid VMEC

The first comparison is represented by a ‘hybrid’ `hegrasha` and VMEC run, where the result from the helical Grad-Shafranov equation is exploited to build a VMEC input file, which is then used to compute the equilibrium. In such a way, V3FIT is not used.

The information listed in subsection 9.2.4 is provided to VMEC through the `hegrasha` computations only, without any additional information. In particular, no pressure is included.

10.1.2 Full V3FIT

The second comparison is represented by a full and independent V3FIT run, where an input file is prepared for V3FIT with all the available information from the experimental side, independently from the `hegrasha` predictions.

This means, as explained in sections 9.2 and 9.3, that a guess for the input parameters is provided to VMEC including a two-power model for pressure and a spline parameterization for the electron temperature – which is not self-consistently related to the density – and then all the diagnostics signals are provided to V3FIT together with the list of reconstruction parameters. After the initial VMEC run, as explained in subsection 9.3.5, each reconstruction parameter is individually changed and the optimal set is eventually found.

The diagnostic information available to V3FIT, described in subsection 2.3.1, is of course much more than what is provided to `hegrasha`, and in particular consists of the magnetic diagnostics (with exception of the 4x48 poloidal array), the Thomson scattering data and the newly developed `extcurz` diagnostic, which will be introduced in chapter 11.

10.2 Results

Let us then consider the comparison between each of the three predictions.

10.2.1 Topology

First, let us compare the flux surfaces, plotted in figure 10.1 for the VMEC $v = 0 = \phi$ polar section. The VMEC flux surfaces do not correspond to the `hegrasha` flux surfaces, since they derive from different computations on different helical fluxes, but they still provide valuable insight into the topological configuration of each simulation.

It is clear that the agreement between the three simulations is partial: each predicts a different position for the helical axis, and the internal flux surfaces exhibit different shapes, with `hegrasha`-predictions being more bean-shaped. A more quantitative comparison will be performed in subsection 10.2.3.

10.2.2 Safety factor

Before considering the Fourier harmonics, let us focus on the helical safety factor q_h defined in eq. (9.8) and plotted in figure 10.2, which gives us a valuable insight into the VMEC and V3FIT solutions.

The helical safety factor is, in fact, the most specific physical quantity provided to VMEC. In the hybrid simulation the VMEC profile (green) derives from the `hegrasha`-computed values (red), and the spline parameterization is exploited as a way of interpolating q_h to a full profile. For the full V3FIT simulation, however, the initial profile (orange) is only the initial guess. Note that, even though such initial guess starts extremely close to the `hegrasha`/VMEC

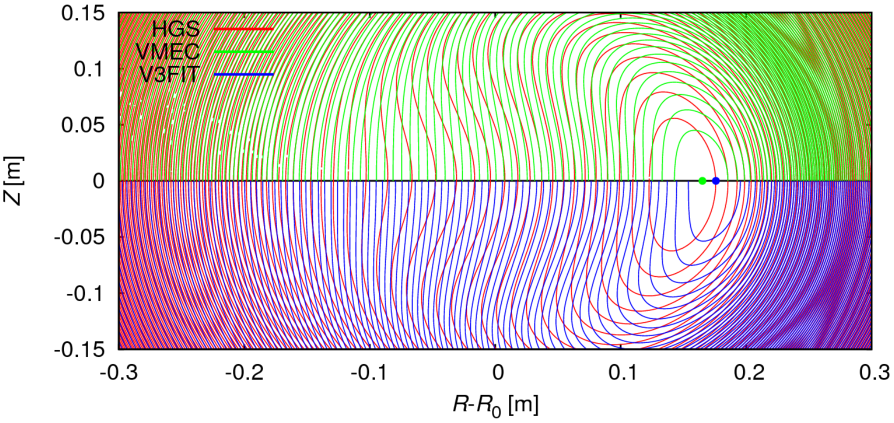

Figure 10.1: Magnified plot of the flux surfaces for the `hegrasha` prediction (red), the simple VMEC computation (green) and the full V3FIT reconstruction (blue). The dots represent the positions of the helical axes.

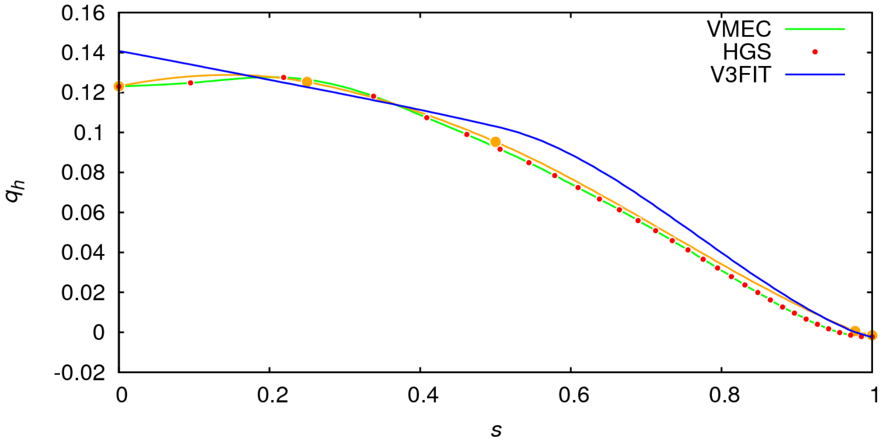

Figure 10.2: Helical safety factor q_h for `hegrasha` (red), VMEC (green), and V3FIT (blue). The initial guess for V3FIT (orange) is plotted as well.

profile, the final V3FIT profile (blue) is extremely different in the internal region.

Given the helical safety factor profiles, a certain difference between the VMEC and the final V3FIT solutions has to be expected.

10.2.3 Solutions

Then, let us focus on the radial profile of the helical flux harmonics, χ^q.

The `hegrasha` harmonics, on one hand, live in the (r, q) space, corresponding to the $(r, u) \equiv (r, m\vartheta - n\phi)$ space. The VMEC/V3FIT harmonics, on the other hand, live in the (s, m, n) space, corresponding to the (s, u, v) space. Therefore, some conversion mechanism has to be employed before the profiles can actually be compared.

For such purpose the VMEC quantities have been expressed back as functions of the cylindrical coordinates,

$$Q(s,u,v) \longmapsto Q(r,\vartheta,\phi), \tag{10.1}$$

and then a two-dimensional Fourier transform has been computed, yielding

$$Q(r,\vartheta,\phi) \longmapsto Q(r,m,n). \tag{10.2}$$

In such a way, the VMEC $m = 0$, $n = 0$ harmonic can be compared with the `hegrasha` $q = 0$, the VMEC $m = 1$, $n = 7$ harmonic with the `hegrasha` $q = 1$ and the VMEC $m = 2$, $n = 14$ harmonic with the `hegrasha` $q = 2$.

Many more VMEC harmonics evidently give contributions to the magnetic fields, e.g. the $m = 0$, $n = 1$ harmonic, but they are not considered in the comparison since they have no equivalent from the `hegrasha` point of view.

Zeroth harmonic

The underlying equilibria for each of the three simulations are plotted in figure 10.3,

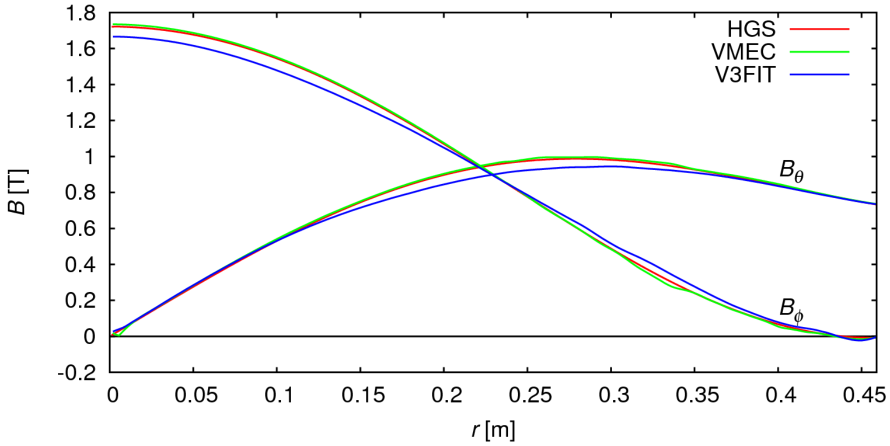

Figure 10.3: Zeroth-order equilibrium fields for the `hegrasha` run (red), the hybrid VMEC computation (green) and the full V3FIT reconstruction (blue).

The zeroth-order harmonics are found to be in reasonable agreement, but a few differences can be found in both the B_ϑ and B_ϕ profiles, mostly between the V3FIT simulation and the other two.

First harmonic

The solution for $\chi^{q=1}$, obtained from eq. (4.9a) for VMEC and V3FIT, are plotted in figure 10.4.

The first-order `hegrasha`, VMEC and V3FIT predictions appear to be in reasonable agreement. Both the scale and the local radial behaviours are consistent between the three simulations.

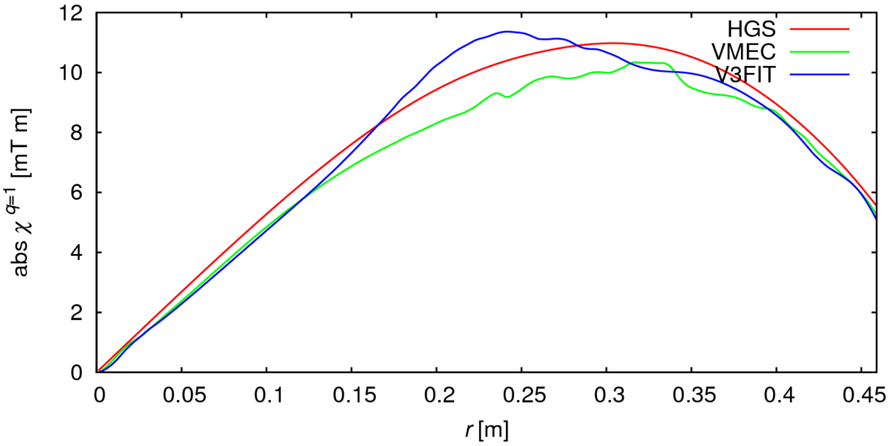

Figure 10.4: The $\chi^{q=1}$ harmonic for `hegrasha` (red), VMEC (green) and V3FIT (blue).

Second harmonic

For the second harmonic, the $\chi^{q=2}$ prediction is plotted in figure 10.5.

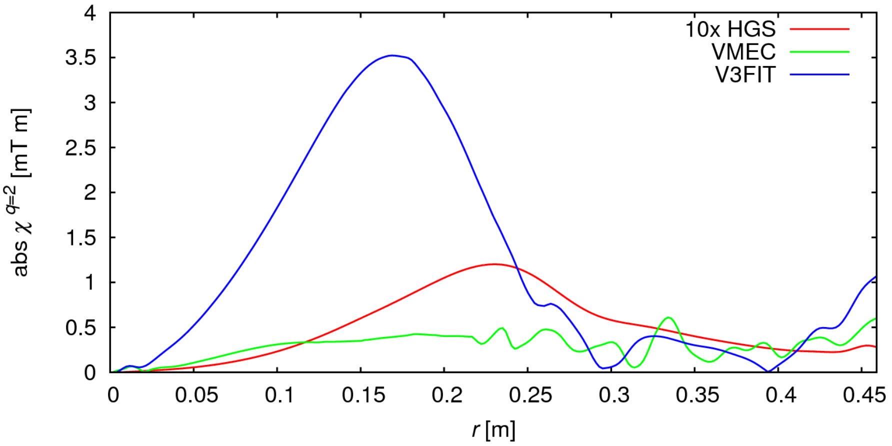

Figure 10.5: The $\chi^{q=2}$ harmonic for `hegrasha` (red), VMEC (green) and V3FIT (blue).

It is evident that the three simulations not only predict different profiles for the second-order harmonic, but predict different amplitudes, too. The V3FIT-predicted amplitude, in fact, is almost 30 times bigger than the `hegrasha` prediction – which is multiplied by 10 in figure 10.5 – and 6 times bigger than the VMEC prediction.

10.2.4 Conclusions

Summarizing, the benchmark of the `hegrasha` code with the VMEC equilibrium computation code on one hand, and with the V3FIT equilibrium reconstruction tool on the other, yields mixed results.

Given the extremely different conditions under which each of the three simulation has been derived, with particular reference to geometries, symmetry assumptions, harmonic content, coordinates, diagnostic information and minimization procedures, the good agreement of the zeroth-order profiles of figure 10.3 and the reasonable agreement of the first-order profiles of figure 10.4 can be interpreted as a satisfying result.

The models, however, exhibit significant differences in the second-order harmonics, between `hegrasha` and both VMEC and V3FIT. The inconsistencies could be linked to non-linear interplay of various MHD modes due to toroidal effects, which are included in the VMEC/V3FIT computations but not in the two-dimensional HGS model. As a consequence, secondary modes like the $m = 0$, $n = 7$ and $m = 2$, $n = 7$ modes – toroidally coupled to the dominant mode – could contribute to the global topology in the VMEC/V3FIT simulations, while the same is prevented in `hegrasha` by the helical symmetry assumption.

CHAPTER 11

A new diagnostic

This chapter is devoted to the introduction, the development and the discussion of the new `extcurz` diagnostic implemented in the V3FIT code.

11.1 Motivation

While running V3FIT fixed-boundary reconstructions, the information about the axisymmetric component of the toroidal field, linked to the currents flowing in the external coils, is completely unaccessible from the point of view of the model. Since such information does have an impact on the reconstruction and in particular on the helical safety factor profile q_h, reconstructions previously had to be manually changed in order to adjust its value at the plasma edge[1] $q_h(a)$ [Ter13].

For this reason a new virtual diagnostic, named `extcurz` for '`external current` along `z`', has been designed and implemented in V3FIT with the purpose of adding a knob that could be automatically tuned depending on external current readings. The new diagnostic is called *virtual* because it does not have a physical experimental setup, even though it does have an experimentally measured value.

Throughout this chapter, for simplicity, the h subscript in q_h will be dropped and its edge value will be consistently labelled q_a. The *helical* safety factor q, therefore, is the one defined in eq. (9.8), which is a function of the normalized flux label s, and not the *cylindrical* safety factor from eq. (2.2), which is a function of the radius r.

11.2 The `extcurz` diagnostic

Let γ be a closed path on the inboard side equator of the last closed flux surface that circles around the torus. By Ampère's Law the circulation of the magnetic field $\mathbf{B}$ on γ is linked to the current enclosed in the area bounded by γ, that is

---

[1] In the following, the plasma boundary is described through both the normalized flux label s and the radius r as the $s = 1$ and $r = a$ surface, respectively.

the current I_{ext} flowing in the external coils, so that

$$\int_\gamma \mathbf{B} \cdot \mathrm{d}\mathbf{l}_\gamma = \mu_0 I_{\text{ext}}. \tag{11.1}$$

The purpose of the new diagnostic `extcurz` is to match the circulation computed by the model and based on the internal magnetic fields with the value of the external currents known and imposed from the outside.

The flux coordinates (s, u, v) used by VMEC have been introduced in subsection 9.2.2. The magnetic field is expressed in the covariant representation through the $\mathbf{e}_i$ of eq. (9.4b), and its components are written as in eq. (9.7),

$$B_i = \sum_{m,n} B_{i,\text{c}}^{m,n} \cos(mu - nv) + B_{i,\text{s}}^{m,n} \sin(mu - nv). \tag{11.2}$$

The path γ is a loop with constant s and u coordinates and varying v coordinate, with path element $\mathrm{d}\mathbf{l}_\gamma = \mathrm{d}v\, \mathbf{e}_v$, so that the dot product from eq. (11.1) is straightforward[2]

$$\mathbf{B} \cdot \mathrm{d}\mathbf{l}_\gamma = \mathbf{B} \cdot \mathrm{d}v\, \mathbf{e}_v = B_v\, \mathrm{d}v. \tag{11.3}$$

Since the higher order harmonics get averaged to zero by the integral in the circulation[3], the integration yields the cosine zeroth order harmonic,

$$\int_\gamma \mathbf{B} \cdot \mathrm{d}\mathbf{l}_\gamma = \int_0^{2\pi} B_v\, \mathrm{d}v = 2\pi B_{v,\text{c}}^{0,0}. \tag{11.4}$$

The current flowing in the external coils is not the only current enclosed in the area bounded by γ: there are also the currents flowing in the passive structures of the machine, that could be either the vacuum vessel, or the shell, or even the support structures. Such currents have to be computed and accounted for in order to get a meaningful comparison between modelled and experimental signals. In RFX-mod the induced current on the vessel is modelled through a simple computation which links the induced current to the flux variation on the vessel and the poloidal and toroidal resistivities.

Once the circulation (and thus the modelled external current) is computed, `extcurz` can be added to the other diagnostics – magnetic sensors, Thomson scattering, interferometers, polarimeters, etc. – so that the difference between the modelled signal and the observed value can weigh in when it comes to the computation of the χ^2.

11.3 Experimental configuration

The configuration that will be considered throughout the article as a typical RFX-mod equilibrium corresponds to a helical state during shot #30227 at 115 ms: such a configuration is characterized by a quasi-helical symmetry and benefits from reduced magnetic chaos and improved confinement properties [Lor09].

---

[2] Eq. (11.3) has the expected dimension for a magnetic circulation: $B_v = \mathbf{B} \cdot \mathbf{e}_v \sim [\mathrm{T}] \cdot [\mathrm{m}]$, since $\mathbf{B} \sim [\mathrm{T}]$ and $|\mathbf{e}_v| = \sqrt{g_{vv}} \sim [\mathrm{m}]$.

[3] While $n \neq 0$ harmonics are averaged to zero, $m \neq 0$, $n = 0$ harmonics are not but their sum *has* to vanish because physically there can not be any u-dependence in the circulation.

The diagnostic setup for such shot involves all and only the magnetic signals introduced in subsection 2.3.1 but without the 4x48 poloidal magnetic probe array, totalling 434 signals. On one hand the absence of thermal signals from the diagnostic setup of the selected shot means that non-magnetic reconstructed profiles, e.g. pressure, are not computed self-consistently and should therefore be left out of the comparisons, while on the other hand it provides a benchmark related to homogeneous all-magnetic data.

The experimental measurement corresponding to the `extcurz` diagnostic, as explained in the previous subsection, is the sum of the poloidal current flowing in the external windings and the correction for the current flowing in the vessel. The toroidal winding system in RFX-mod consists of 12 sectors: each sector is made of 4 coils, and each coil has 8 turns. The error related to the current flowing in each turn, 30 A, has to be multiplied by the number of turns, 12x4x8, so the total uncertainty is found to be 11.52 kA. Since the current for the specified shot amounts to 141.89 kA, the error on `extcurz` turns out to be approximately 8% of the signal.

11.4 Reconstructions

Among the input parameters needed by VMEC in order to perform a fixed-boundary computation, as discussed in subsection 9.2.4, the safety factor profile has to be specified. In this shot, the safety factor is parameterized through a spline function with four (s, q) points from the magnetic axis to the plasma boundary: $(0, q_0)$, $(s_{\max}, q_{\max})$, $(s_{\text{rev}}, 0)$, $(1, q_a)$. Each of the five parameters – q_0, $s_{\max}$, $q_{\max}$, s_{rev}, q_a – can then be varied and adjusted by V3FIT during the reconstruction: `extcurz` is designed to address in particular the edge safety factor q_a.

As discussed by Terranova in [Ter13], the edge safety factor is expected to scale linearly with the external current. The effect of `extcurz`, therefore, can be investigated running three different kinds of reconstructions based on the same input files: 'control' runs, where the edge safety factor q_a is kept fixed and can not be adjusted by V3FIT; 'blind' runs, where q_a is adjusted by V3FIT but without knowledge of the `extcurz` value; 'full' runs, where V3FIT adjusts the q_a given the value provided by `extcurz`.

If the new diagnostic is indeed a valuable one, one should see that V3FIT is not able to adjust the q_a correctly and consistently without the corresponding `extcurz` value, and that the 'full' reconstructions interpret the experimental data better than the 'control' or the 'blind' runs, leading to smaller normalized χ^2 values.

The prediction of the 'control' reconstructions[4] depend, of course, upon the guess for the edge safety factor: the nearer q_a is to the 'true' value, the more agreement one will find between modelled and experimental signals, even without the insight provided by `extcurz`. In order to account for such a bias a full scan has been performed varying the initial q_a values: by choosing q_a further away from the expected value, the effect of `extcurz` is emphasized.

---

[4] The predictions of the 'blind' and 'full' reconstructions depend upon the guess for q_a as well, since there could be different minima accessible in parameter space. In other words, `extcurz` removes one degree of degeneracy, but there could be more.

11.5 Results

Before entering a quantitative analysis, let us first qualitatively discuss the results for the safety factor profiles for each set of reconstructions.

11.5.1 Edge safety factor

The reconstructed edge safety factor values are plotted in figure 11.1 for each set of runs.

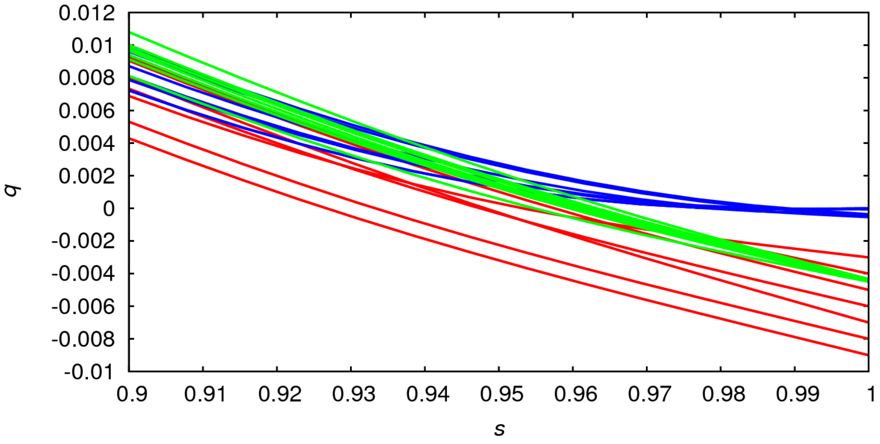

Figure 11.1: Edge safety factor for ‘control’ (red), ‘blind’ (blue) and ‘full’ (green) runs. Different lines correspond to different initial q_a values.

As can be clearly seen from figure 11.1, each ‘control’ reconstruction has the same q_a that was specified as input, since V3FIT is configured not to vary it, while ‘blind’ and ‘full’ runs exihibit different values depending on the minimization path followed by the V3FIT reconstruction. In such cases, however, one can distinguish two different accumulation points: ‘blind’ runs converge towards an extremely shallow edge safety factor, $q_a \approx -0.0005$, ‘full’ runs converge towards a deeper value, $q_a \approx -0.0045$.

11.5.2 Safety factor profile

Let us then consider the complete q profiles for each set of runs, plotted in figure 11.2.

The difference between each set of profiles becomes clearer as we go near the magnetic axis, due to the absence of an experimental condition to be imposed on q_0 but also due to the spline nature of the profile: the value on axis heavily influences the behaviour in the internal region. The ‘control’ runs are characterized by a thick variation over all the s-domain, as opposed to ‘blind’ and ‘full’ runs which exhibit a narrow variation from the edge region up until the $s \approx 0.4$ region. A different qualitative behaviour can however be detected for ‘blind’ and ‘full’ runs: the former tend to be much steeper near the magnetic axis and hollow in the internal region, while the latter show a much softer slope.

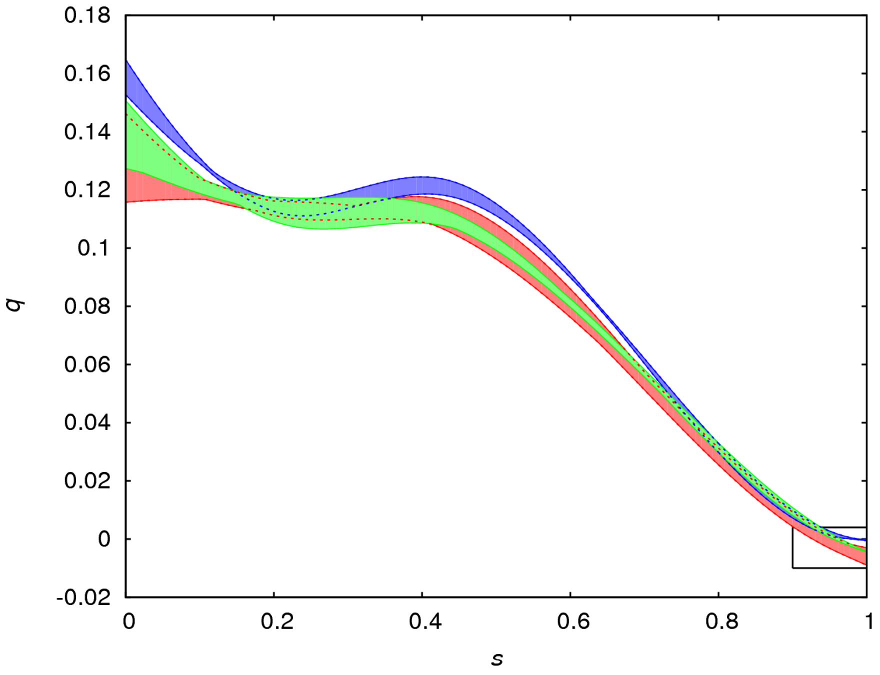

Figure 11.2: Summary of the reconstructed profiles for 'control' (red), 'blind' (blue) and 'full' (green) runs. For each set of runs, the area swept by a subset of the reconstructed profiles with different initial q_a is shown. The top and bottom boundary lines do not necessarily correspond to a single profile, as they are computed as the maximum and minimum q-points at every s-position. The black rectangle near the edge shows the area magnified in figure 11.1.

Such feature gives an indication of the difficulty of finding a well-behaved spline profile closely fitting the experimental data.

On the other hand, by specifying more points for the initial guess spline interpolation or by choosing a global parameterization instead, one would find much more stability and profile stiffness for the safety factor. At the same time, however, the effect of the `extcurz` diagnostic would be less clear.

11.5.3 Signal effectiveness

Let us now take a look at the effect of `extcurz` on q_a. The signal effectiveness matrix, computed through eq. (9.15), is a way to check *a posteriori* the link between each diagnostic signal and each reconstruction parameter [Han10]. The maximum values of the signal effectiveness matrix with respect to the q_a parameter are plotted in the top panel of figure 11.3, whereas in the bottom panel the maximum values for the total toroidal flux Φ_{tot} are shown. The effectiveness is written as a percentage since the sum over all the 'switched on' diagnostics yields 100%.

In 'full' runs `extcurz` is indeed the most effective diagnostic on the edge safety factor reconstruction, with an effectiveness in the first step of the reconstruction between 10% and 45%, to be compared to 'blind' runs, where the

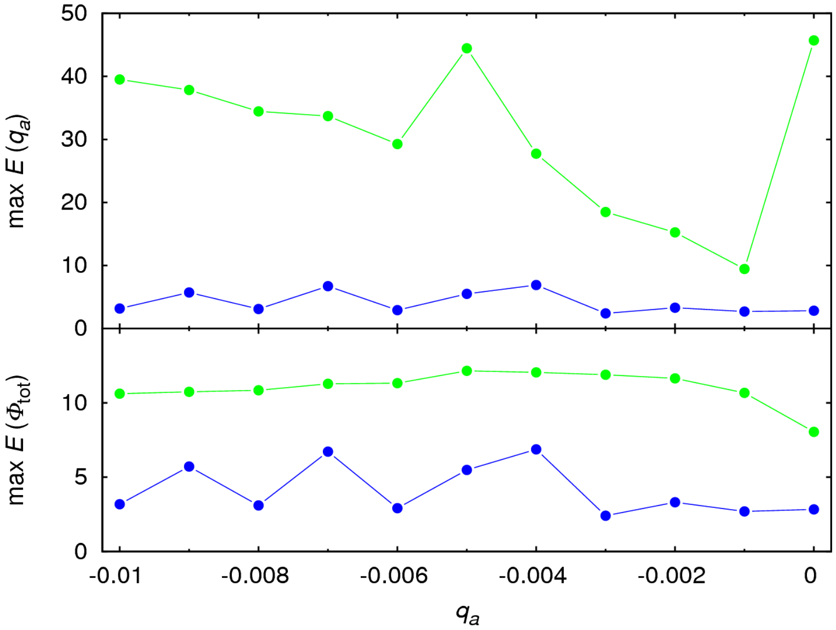

Figure 11.3: For 'blind' (blue) and 'full' (green) runs the maximum signal effectiveness (over all the diagnostics) for determining q_a (top panel) and $\Phi_{\rm tot}$ (bottom panel) is plotted against the initial q_a, which identifies each run. In each 'full' run `extcurz` has the largest signal effectiveness with respect to both q_a and $\Phi_{\rm tot}$, while in 'blind' runs the maxima correspond to several different diagnostics.

value oscillates around 5%. Moreover, the signal effectiveness matrix shows that in each 'full' run `extcurz` is the most influential diagnostic also on the total enclosed toroidal flux $\Phi_{\rm tot}$, with an effectiveness oscillating around 10%, again greater than the 5% obtained in 'blind' runs. This confirms that `extcurz` is indeed a valuable magnetic diagnostic, that is most effective on edge parameters.

11.5.4 Posterior error

The uncertainty on the q_a parameter provided *a posteriori* through eq. (9.14) turns out to be, for the last reconstruction step, approximately $4.22 \cdot 10^{-4}$ for 'blind' runs and $4.16 \cdot 10^{-4}$ for 'full' runs, with no apparent dependence upon the presence of `extcurz`.

For 'full' runs, this amounts to a percentage error of about 9%, therefore comparable with the 8% `extcurz` signal error initially provided to V3FIT.

For 'blind' runs, however, the error is much bigger than the signal itself. This could be explained by considering that without high-effectiveness signals like `extcurz`, the minimization procedure cannot distinguish a successful parameter reconstruction with a reasonable signal error from an unreliable reconstruction with a large signal error, since both yield low χ^2 values. The 'blind' runs, therefore, are probably biased by numerical issues.

11.5.5 Chi squared

Finally, let us focus on the χ^2 values computed from eq. (9.10) and shown in figure 11.4. On one hand, one can take a look at the total χ^2 used by V3FIT, labelled χ^2_{V3F}, which is sum of the χ^2 of the *switched on* diagnostics. But, on the other hand, one can consider an *effective* χ^2 that takes into account also the χ^2 relative to `extcurz`, χ^2_{ecz}, even if the diagnostic itself is switched off and which is consequently labelled $\chi^2_{\mathrm{V3F+ecz}}$. For 'control' and 'blind' runs, therefore, $\chi^2_{\mathrm{V3F+ecz}} = \chi^2_{\mathrm{V3F}} + \chi^2_{\mathrm{ecz}}$, while for 'full' runs $\chi^2_{\mathrm{V3F+ecz}} \equiv \chi^2_{\mathrm{V3F}}$ since χ^2_{ecz} is included in both terms. The purpose of such distinction is to stress which χ^2 is used by V3FIT for the reconstruction.

Both values are furthermore *normalized* to the number of diagnostics in order to get comparable quantities for 'control' and 'blind' runs (which have 434 signals) and 'full' runs (which have 435).

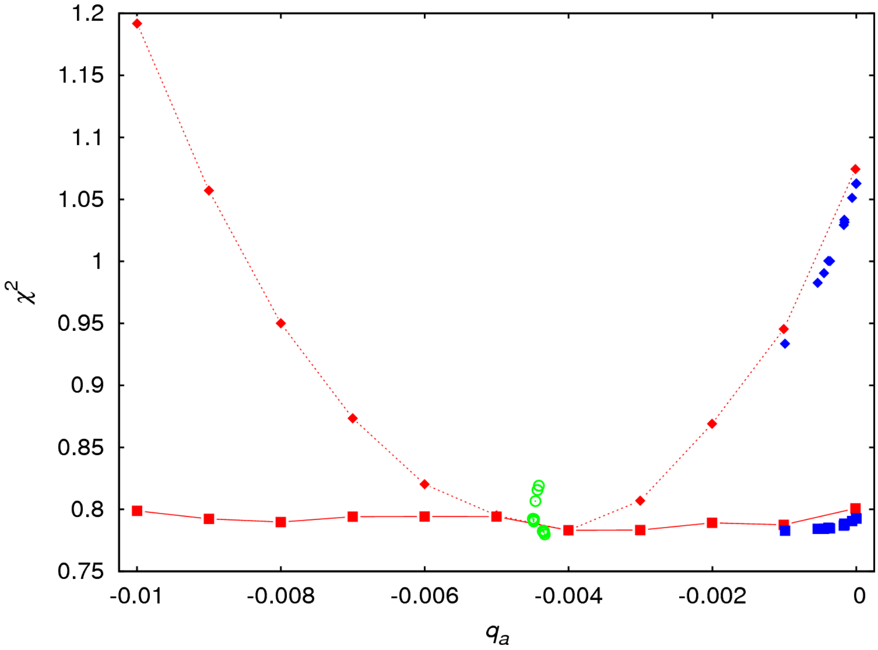

Figure 11.4: Summary of the normalized χ^2 values for each run: for 'control' (red) and 'blind' (blue) runs, the squares (■) correspond to the V3FIT-computed χ^2_{V3F} and the diamonds (⧫) correspond to the effective $\chi^2_{\mathrm{V3F+ecz}}$; for 'full' (green) runs, the circled dots ($\odot$) correspond to both, $\chi^2_{\mathrm{V3F}} \equiv \chi^2_{\mathrm{V3F+ecz}}$.

The 'control' curves in figure 11.4 provide us with valuable information about the degeneracy in the edge safety factor parameter space. As the squares show, from V3FIT's point of view there is no dependence of χ^2_{V3F} upon q_a. The degeneracy can be removed by taking into account `extcurz`, and indeed the effective $\chi^2_{\mathrm{V3F+ecz}}$ shows a much more definite behaviour with a minimum at $q_a \approx -0.0045$.

Figure 11.1 showed that 'blind' runs converge towards an extremely shallow reversal, accumulating around $q_a \approx -0.0005$. Figure 11.4 shows the same result, but also paints the complete picture: V3FIT is unaware that the reconstructed edge safety factors do not agree with the experimentally measured external current, since such information is provided by the χ^2_{ecz} term only. From this aspect, therefore, 'blind' runs are extremely unsuccessful in that even the ones starting with a q_a close to the experimental value (e.g. around $q_a \approx -0.0045$) converge towards an almost unreversed configuration.

In the case of 'full' runs, by construction, the χ^2 computed by V3FIT involves the `extcurz` term, so that the minimum in q_a space can be detected and acted upon. The reconstructed edge safety factor values appear to be independent from the initial q_a guesses, even though a certain spread in χ^2 can be found, due to the fact that the q_a scan forces extremely unreasonable initial guesses and therefore extremely different paths took by the minimization algorithm stop in different places, given the specified χ^2 threshold. The 'full' runs, with `extcurz` switched on, are the only runs that successfully and reliably reconstruct the edge safety factor without hindering significantly the agreement of the other diagnostic signals with the measured data.

11.6 Conclusions

In case of fixed-boundary V3FIT reconstructions, the link between the edge safety factor and the external currents carries important information for the consistency of the model. While previously such consistency had to be manually imposed by user trial and error [Ter13], the implementation of the new `extcurz` diagnostic makes it automatic and allows to align it with the χ^2 minimization procedure, core process of the reconstruction.

The results show that the q_a reconstruction is necessary to gain independence from initial guess mistakes, but that it cannot be 'blindly' varied and has to be coupled with the new diagnostic. The edge safety factor degeneracy is indeed removed with the insight provided by `extcurz`, which lets V3FIT precisely reconstruct q_a and further lower the effective χ^2, therefore leading to much better reconstructions.

Even though the proposed analysis involves the RFP configuration, `extcurz` could be applied to tokamak fixed-boundary reconstructions as well.

Part IV

Conclusions

Summary

In this thesis the two-dimensional helical Grad-Shafranov equation has been solved through a numerical code developed for this purpose, and the V3FIT three-dimensional equilibrium reconstruction suite has been exploited first to carry out a benchmark against the HGS solver and then to reconstruct RFX-mod equilibria more precisely, thanks to a new virtual magnetic diagnostic.

Helical Grad-Shafranov model

The helical Grad-Shafranov equation is obtained under the symmetry assumption that a single dominant mode, which produces the helical deformation of the plasma column, is present on the equilibrium with its higher order harmonics. The Fortran code developed as a numerical solver relies on an iterative procedure which separates the right-hand from the left-hand side of the HGS equation, therefore shifting the high non-linearity from the solution itself to the search of self-consistency between the RHS and LHS. Through a Fourier transform, in fact, the problem becomes linear and admits numerical solutions, satisfying a single boundary condition. Given the availability of two external measurements in the experimental setup of RFX-mod the boundary condition problem is overdetermined, and the solution cannot satisfy both. Indeed, the reconstructed HGS solution for a single-helical-axis problem during a RFP shot does not satisfy exactly the non-enforced boundary condition, and the mismatch is found to be less than 5%. A solution for this problem has been proposed, consisting in the addition of an auxiliary term to the exact HGS solution, which lets both boundary conditions be enforced simultaneously. The weight of the additionary condition has been found to be 5%, not unsurprisingly comparable to the mismatch between the enforced and measured boundary condition. The HGS model has been applied to a tokamak shot with a magnetic island as well, yielding less consistent results than the single-helical-axis case for the RFP shot.

The helical Grad-Shafranov solver provides interesting physics by relaxing the assumption of linearity in the problem as opposed, for example, to the perturbation analysis carried out through a Newcomb model, often exploited for MHD reconstruction of tearing modes. The proposed method, indeed, is fully non-linear and lets a three-dimensional configuration be reduced and analysed through a two-dimensional equation thanks to the helical symmetry assumption. The helical Grad-Shafranov represents therefore a valuable gateway between two- and three-dimensional physics.

Benchmark of the HGS model with VMEC and V3FIT

Three-dimensional equilibrium reconstruction codes like VMEC/V3FIT cannot rely on a Grad-Shafranov equation and instead exploit energy minimization principles for the solution of the equilibrium equations. The assumptions for the VMEC code, nonetheless, are strict in that the plasma has to be characterised by good and nested flux surfaces, so that VMEC cannot be exploited to model complex topologies where tearing mode islands are present. In the case of a single-helical-axis topology VMEC can be applied, and in the present work it has been exploited as a benchmark tool against the helical Grad-Shafranov model. The comparison of the two-dimensional, albeit helically symmetric, code to the fully three-dimensional algorithm has provided interesting results. In fact, even though each code has been derived under different assumptions, with particular reference to the spectral contents and the coordinates, a good agreement is found for the zeroth-order solutions and the first-order quantities appear in reasonable agreement. The second-order harmonics do not agree, however, confirming that the models have different inner physics, which has to be compared carefully.

Development of a new virtual diagnostic

As a further result, a new virtual diagnostic for V3FIT has been developed to provide a constraint on the edge safety factor in fixed-boundary reconstructions. The proposed benchmark of the new diagnostic has demonstrated that indeed the final reconstructions benefit from the additional information, which otherwise would not enter the fixed-boundary problem, and help to get a more self-consistent helical safety factor profile.

Bibliography

[Abr72] M. Abramowitz and I. A. Stegun, *Handbook of Mathematical Functions with Formulas, Graphs, and Mathematical Tables*, New York: Dover Publications, 1972, OCLC 18003605.

[Alf07] A. Alfier and R. Pasqualotto, «New Thomson scattering diagnostic on RFX-mod», *Review of Scientific Instruments*, **78** (1): 013505, 2007, DOI 10.1063/1.2431769.

[D'h91] W. D. D'haeseleer, W. N. G. Hitchon, J. D. Callen and J. L. Shohet, *Flux Coordinates and Magnetic Field Structure*, Springer-Verlag, 1991, OCLC 839704811.

[Fin92] J. M. Finn, R. Nebel and C. Bathke, «Single and multiple helicity Ohmic states in reversed-field pinches», *Physics of Fluids B: Plasma Physics (1989-1993)*, **4** (5): 1262–1279, 1992, DOI 10.1063/1.860082.

[Fit99] R. Fitzpatrick, «Formation and locking of the "slinky mode" in reversed-field pinches», *Physics of Plasmas (1994-present)*, **6** (4): 1168–1193, 1999, DOI 10.1063/1.873361.

[Fra01] P. Franz, L. Marrelli, A. Murari, G. Spizzo and P. Martin, «Soft X ray tomographic imaging in the RFX reversed field pinch», *Nuclear Fusion*, **41** (6): 695, 2001, DOI 10.1088/0029-5515/41/6/304.

[Han09] J. D. Hanson, S. P. Hirshman, S. F. Knowlton, L. L. Lao, E. A. Lazarus and J. M. Shields, «V3FIT: a code for three-dimensional equilibrium reconstruction», *Nuclear Fusion*, **49** (7): 075031, 2009, DOI 10.1088/0029-5515/49/7/075031.

[Han10] J. D. Hanson, S. F. Knowlton, B. A. Stevenson and G. J. Hartwell, «Equilibrium and Stability of Current-Carrying Discharges in the Non-Axisymmetric CTH Experiment», *Contributions to Plasma Physics*, **50** (8): 724–730, 2010, DOI 10.1002/ctpp.200900059.

[Hir83] S. P. Hirshman and J. C. Whitson, «Steepest-descent moment method for three-dimensional magnetohydrodynamic equilibria», *Physics of Fluids (1958-1988)*, **26** (12): 3553–3568, 1983, DOI 10.1063/1.864116.

[Hir86] S. P. Hirshman and D. K. Lee, «MOMCON: A spectral code for obtaining three-dimensional magnetohydrodynamic equilibria», *Computer Physics Communications*, **39** (2): 161 – 172, 1986, DOI 10.1016/0010-4655(86)90127-X.

[Hir91] S. P. Hirshman and O. Betancourt, «Preconditioned descent algorithm for rapid calculations of magnetohydrodynamic equilibria», *Journal of Computational Physics*, **96** (1): 99 – 109, 1991, DOI 10.1016/0021-9991(91)90267-O.

[Inn97] P. Innocente, S. Martini, A. Canton and L. Tasinato, «Upgrade of the RFX CO2 interferometer using in-vessel optics for extended edge resolution», *Review of Scientific Instruments*, **68** (1): 694–697, 1997, DOI 10.1063/1.1147677.

[Kre88] M. E. Kress, «Back-averaging: An accelerated iterative method for simulating plasma diffusion», *Journal of Computational Physics*, **76** (1): 201–230, 1988, DOI 10.1016/0021-9991(88)90138-6.

[Lor08] R. Lorenzini, D. Terranova, A. Alfier, P. Innocente, E. Martines, R. Pasqualotto and P. Zanca, «Single-Helical-Axis States in Reversed-Field-Pinch Plasmas», *Phys. Rev. Lett.*, **101**: 025005, 2008, DOI 10.1103/PhysRevLett.101.025005.

[Lor09] R. Lorenzini, E. Martines, P. Piovesan, D. Terranova, P. Zanca, M. Zuin, A. Alfier, D. Bonfiglio, F. Bonomo, A. Canton, S. Cappello, L. Carraro, R. Cavazzana, D. F. Escande, A. Fassina, P. Franz, M. Gobbin, P. Innocente, L. Marrelli, R. Pasqualotto, M. E. Puiatti, M. Spolaore, M. Valisa, N. Vianello, P. Martin and the RFX-mod team, «Self-organized helical equilibria as a new paradigm for ohmically heated fusion plasmas», *Nature Physics*, **5**: 570–574, 2009, DOI 10.1038/nphys1308.

[Ort93] S. Ortolani and D. D. Schnack, *Magnetohydrodynamics of Plasma Relaxation*, World Scientific Publishing, 1993, OCLC 28204196.

[Son03] P. Sonato, G. Chitarin, P. Zaccaria, F. Gnesotto, S. Ortolani, A. Buffa, M. Bagatin, W. R. Baker, S. D. Bello, P. Fiorentin, L. Grando, G. Marchiori, D. Marcuzzi, A. Masiello, S. Peruzzo, N. Pomaro and G. Serianni, «Machine modification for active MHD control in RFX», *Fusion Engineering and Design*, **66-68** (0): 161–168, 2003, DOI 10.1016/S0920-3796(03)00177-7.

[Ter13] D. Terranova, L. Marrelli, J. Hanson, S. Hirshman, M. Cianciosa and P. Franz, «Helical equilibrium reconstruction with V3FIT in the RFX-mod Reversed Field Pinch», *Nuclear Fusion*, **53** (11): 113014, 2013, DOI 10.1088/0029-5515/53/11/113014.

[Tre10] G. L. Trevisan, *Profilo radiale delle perturbazioni MHD in un plasma di tipo RFP: confronto tra le analisi in geometria cilindrica e toroidale*, Master's thesis, Università degli Studi di Padova, 2010.

[Wes04] J. Wesson, *Tokamaks*, Clarendon Press, 3rd edition, 2004, OCLC 13760665.

[Zan07] P. Zanca, L. Marrelli, G. Manduchi and G. Marchiori, «Beyond the intelligent shell concept: the clean-mode-control», *Nuclear Fusion*, **47** (11): 1425, 2007, DOI 10.1088/0029-5515/47/11/004.

Figure: “The Man Who Fell Sideways” from `xkcd.com/417`.